Second harmonic generation at crystalline semiconductor surfaces

by

Norberto Arzate Plata

A thesis submitted in conformity with the requirements
for the degree of Doctor in Sciences (Optics)

Centro de Investigaciones en Óptica, A.C.
Department of Optical Properties of Matter
Universidad de Guanajuato
México

November, 2000

What we observe is not nature itself,
but nature exposed to our mode of questioning.

Werner Heisenberg

To my mom,
sisters and brothers.

Contents

List of Figures

List of Tables

Acknowledgements

I acknowledge the invaluable supervision of this thesis by *Dr. Bernardo Mendoza Santoyo.* I thank him for his intelligently guidance and teaching which have made me improve my scientific experience.

I thank *Dr. Oracio Barbosa García (CIO), Dr. José Luis Maldonado Rivera (CIO), Dr. Alfonso Lastras Martínez (IICO), Dr. Rodolfo Del Sole (U. of Rome II)* and *Dr. Tony F. Heinz (Columbia U.)* for revising this thesis and their helpful suggestions to improve its understanding.

I thank *Lucymarie Mantese and Mike Downer* of U. of Texas at Austin, for allowing us to use their experimental data prior to publication.

I thank *Teresita Pérez* for your assistance in the management of the UNIX system.

I acknowledge the facilities and support of *Centro de Investigaciones en Óptica*.

I acknowledge the support of Consejo Nacional de Ciencia y Tecnología CONACyT, Mexico.

I appreciate the help and suggestions of Dr. Oracio Barbosa who always has shown interest in my professional success.

In a special way, I thank *my mom* and *all my sisters* and *brothers* for giving courage to get the doctorate to me.

Finally but not less important, I thank the friendship of *Jorge E. Mejía, Eric Rosas, Gilberto Gómez, Mario Pacheco* and *Elizabeth Falcón* who shared with me significant moments while my doctoral studies.

Resumen

Primeramente, se presentan espectros de reflectancia anisotrópica y generación de segundo armónico de superficies limpias y reconstruidas de Si(100). El cálculo se realiza en base al modelo de enlaces polarizables donde el cristal de Si se modela como un conjunto de dipolos puntuales los cuales responden a los campos electromagnéticos incidentes. Cada dipolo se considera que se encuentra localizado a la mitad de cada enlace Si-Si. El modelo incorpora la reconstrucción de la superficie a través del efecto del campo local. Se calcula el espectro óptico para una superficie con reconstrucción 2×1 como función del buckling del dímero y se muestra que la estructura atómica que reproduce los espectros de reflectancia anisotrópica y generación de segundo armónico es aquella con un buckling de 0.6 Å. Se presentan, además, los espectros para una superficie con reconstrucción c(4×2) y se comparan con los resultados experimentales.

Por otro lado, se aplica un modelo microscópico para calcular las diferentes contribuciones a la susceptibilidad no lineal de segundo orden que se requiere en el cálculo de la generación de segundo armónico. Estos términos se clasifican como transiciones 1ω y 2ω y, de acuerdo con el carácter de los estados de superficie o de bulto entre los cuales las transiciones se llevan a cabo. Como ejemplo, se analizan los efectos de estas susceptibilidades microscópicas en el espectro de generación de segundo armónico de una superficie de Si(100)c(4×2) limpia. Se analizan las siguientes resonancias que se han observado experimentalmente: la resonancia E_1 del Si de bulto a $2\omega \sim 3.3$ eV y las resonancias a $2\omega \sim 2.2$ y 3 eV. Nuestro formalismo nos permite comprender el origen de estas resonancias de superficie en la generación de segundo armónico.

Finalmente, mediante el modelo microscópico anterior se estudia el efecto de campos eléctricos dc superficiales en la generación de segundo armónico. Se obtienen espectros de generación de segundo armónico de superficies de Si(100) dopadas con Boro, limpias y con adsorsión de H . Se encuentra que el comportamiento teórico de la resonancia E_1 del

Si como función de la cobertura de H concuerda con el comportamiento experimental. Se concluye que la presencia de campos eléctricos dc superficiales, cuya magnitud depende de la cobertura de B y H, juega un papel importante en la generación de segundo armónico.

Abstract

First, we obtain linear and non-linear optical spectra of clean Si(100)2×1 reconstructed surfaces based on the model of polarizable bonds. The crystal is modeled as an array of point-like polarizable dipoles where each dipole is considered to be at the middle of every Si-Si bond. The model incorporates the reconstruction of the surface trough the local field effect. We calculate the optical spectra as a function of dimer buckling and it is shown that the structure which nicely reproduce the experimental reflectance anisotropy and second harmonic generation (SHG) spectra is that with a buckling of 0.6 Å. We also discussed the features in the spectra for the c(4×2) Si(100) surface.

On the other hand, we apply a microscopic formalism to calculate the different contributions to the nonlinear second-order susceptibility required in the calculation of SHG. These terms are classified according to 1ω and 2ω transitions and to the surface or bulk character of the states among which the transitions take place. As an example, we analyze the effects of these microscopic susceptibilities on the SHG spectrum of a clean Si(100)c(4×2) surface. Three resonances seen experimentally in SHG are analyzed through this approach. They are the E_1 resonance of bulk Si at $2\omega \sim 3.3$ eV and two other at $2\omega \sim 2.2$ and 3 eV. The physical nature of the microscopic susceptibilities calculated with our formalism allow us to understand the origin of these surface SHG resonances.

Finally, through the above microscopic formalism we calculate the second harmonic spectra of Si(100) in the presence of surface localized dc-electric field. It is found that the surface-allowed E_1 resonances for clean and H-covered surfaces shift as a function of the dc field in agreement with experiment. This suggests the presence of built-in electric fields strongly localized in the subsurface region and whose strength depends on the B and H coverage.

Chapter 1

Introduction

“We have called it the Transistor, because it is a resistor or semiconductor device which can amplify electrical signals as they are transferred through it.” These were the words of Ralph Bown announcing the new invention of the *transistor* on 1948 at a press conference held in the Bell Labs headquarters [1, 2]. Its inventors Shockley, Bardeen and Brattain marked the birth of a new era, i.e. the information age. Hardly an electronic equipment can be made today without such a device. At that time a supercomputer was as big as the size of a laboratory room and since then, the transistor has made possible to built compact electronic computers and other devices with size moving from microscopic circuits to impressive dimensions comparable to interatomic distances [3]. Nowadays, millions of transistors can be built on a square of silicon -the base material for building an integrated circuit- about the size of a fingernail.[*]

The good performance in making devices of such interatomic dimensions requires the preparation of clean[†] or adsorbed covered surfaces. The proper order or arrangement of atoms on the used surface is essential since the feasibility or quality of the surface for its well functioning depends on it. The most popular ways to obtain clean surfaces are [5]:

---

[*] Most electronic devices are built on microscopic circuits engraved on silicon chips. However many silicon-dominated circuits require considerable admixture of gallium arsenide components. The advantages of the gallium arsenide [4] lie in the speed with which electrons move through it, in weak signal generation operations and in the generation and detection of light. These advantages suit it for roles in computing, television reception and the optoelectronic transmission of data through optical-fiber networks.

[†] The word clean is connected with the limit of detection. For surface crystallographic studies 1% of a monolayer (ML) or less often can not be detected. On the other hand such level of impurities might be easily detectable if the surface electrical properties of semiconductors are studied [5].

a) cleaving, which is restricted to certain orientations of the selected group of crystals that cleave easily or b) noble gas ion sputtering and annealing after orienting, cutting and polishing the crystal outside the ultra-high vacuum (UHV) chamber. The latter method is the most viable. In this method, gas ions are produced by electron impact and accelerated towards the sample then, the surface impurities and first few layers of the underlying material can be removed. After the bombardment, careful annealing of the sample results in recrystallization of the surface.

In the process of manufacture of electronic devices the following question arises: How can we control the quality of surfaces that build up the device? Here is where Surface Science plays an important role since reliable characterization of surfaces and interfaces is needed for the development and manufacture of such devices.

Many tools for surface analysis have been developed, among others we have *synchrotron radiation* which is used for surface experiments where high intensity electromagnetic radiation to analyze surfaces is needed. This radiation is useful, for instance, for photoelectron spectroscopy and reflectivity measurements in the ultraviolet region. The *low energy electron diffraction* (LEED) method is used for determining surface structures. Low energy electrons have a wavelength comparable with the internuclear spacings of the atoms in a crystal, e.g $\approx$1 Å for an energy of $\approx$150 eV. Electrons with this energy penetrate only a few atomic layers due to the strong interaction with the solid so that only the outermost surface layers can be probed. *Photoelectron or photoemission spectroscopy* is a technique that is based on the photoelectric effect. The crystal is irradiated and photoelectrons are emitted from the filled valence bands just below the Fermi level with different kinetic energies. By means of a retarding potential the number of electrons with kinetics energies greater than a fixed energy can be determined. If the experiments are performed in the ultraviolet spectral region, then the technique is called *ultraviolet photoemission spectroscopy* (UPS) or if soft-x rays are used we then call it *x-ray photoemission spectroscopy* (XPS). *Auger electron spectroscopy* (AES) is used to probe for impurities. In this technique an electron (auger electron) is emitted after deexcitation of the atom once it has been bombarded with energetic electrons or photons. The emitted electron has a characteristic kinetic energy determined by the quantum states of the atom.

Besides the techniques mentioned above, we have the *optical techniques*, which unlike others, they do not require UHV environments and also they are non-invasive, nondestructive, and have wide spectral coverage as well. These techniques do not have enough surface sensitivity unless the signal contributed by the bulk media can be suppressed. In particular in this thesis, we will apply two optical techniques to study surfaces: *the reflectance anisotropy spectroscopy* (RAS) and mainly *second harmonic generation* (SHG).

RAS is a linear optical technique that is used to characterize structural and electronic properties of semiconductor surfaces [6–12]. The RAS measures changes in reflectance as a function of light polarization and is defined as the ratio

$$\frac{\Delta R}{R_0} = \frac{\Delta R_y - \Delta R_x}{R_0}. \tag{1.1}$$

where ΔR_y (ΔR_x) is the reflectance of light polarized in the y (x) direction and R_0 is the Fresnel reflection coefficient.

The RAS technique is based on measuring differential reflectivities and used as a surface probe when a medium is optically isotropic in the bulk (e.g. a cubic crystal) but the surface is anisotropic. The symmetry of the medium causes the signal from the bulk to cancel, which in turn makes the RAS a highly sensitive surface probe. Several phenomenological and microscopic theoretical methods have attempted to explain the observed RAS experimental spectra of surfaces and interfaces. The phenomenological models to describe differential reflectivities range from the three layer model of McIntyre and Aspnes [13], where the dielectric tensor of the crystal-vacuum interface was modeled by isotropic three-layer model, the discrete dipole models of Mochán and Barrera [6], Mendoza and Mochán [8], Hogan and Patterson [10], Wijers and Boeij [7] where local field effects are taken into account, to the more recent microscopic formulations of Mendoza *et al.* [9], Palummo *et al.* [11], and Rohlfing and Louie [12].

On the other hand, the optical technique of SHG has been used recently thanks to the invention of the laser. SHG is a second-order non-linear process first observed by Franken *et al.* [14]. They observed the second harmonic (SH) ultraviolet light at $\sim 3472\,\mathring{A}$ produced by propagating a ruby laser beam at 6944 $\mathring{A}$ through a quartz crystal. Later Terhune *et al.* observed the SH generation of light in a medium with inversion symmetry [15].

The SHG technique arises because a second-order process is forbidden, within the dipole approximation, in a medium with inversion symmetry, i.e. centrosymmetric medium [16]. Such a symmetry will necessarily be broken at an interface, for instance the discontinuity of the interface (i.e. the structural change in passing from the bulk to the surface layer) is sufficient to break such a symmetry, and thus the second-order non-linear process is therefore allowed at the surface.

Consider the following electromagnetic optical wave

$$\vec{E}(\vec{r},t) \sim \vec{E}(\vec{r})e^{-i\omega t}, \tag{1.2}$$

oscillating at frequency ω impinging on a medium. The total polarization induced by this wave is given by

$$\begin{aligned}\vec{P}(\vec{r},t) &= \overset{\leftrightarrow}{\alpha}\cdot\vec{E}(\vec{r},t) + \overset{\leftrightarrow}{\chi} : \vec{E}(\vec{r},t)\vec{E}(\vec{r},t) + \cdots \\ &= \overset{\leftrightarrow}{\alpha}\cdot\vec{E}(\vec{r})e^{-i\omega t} + \overset{\leftrightarrow}{\chi} : \vec{E}(\vec{r})\vec{E}(\vec{r})e^{-i2\omega t} + \cdots\,, \end{aligned} \tag{1.3}$$

where the first and second terms on the right hand side give the response at ω and 2ω, respectively. After a proper Fourier transformation, we obtain

$$\vec{P}(\omega) = \overset{\leftrightarrow}{\alpha}(\omega)\cdot\vec{E}(\omega) \tag{1.4}$$

the linear polarization proportional to the incoming field with $\overset{\leftrightarrow}{\alpha}(\omega)$ the linear polarizability tensor and

$$\vec{P}(\vec{r},2\omega) = \overset{\leftrightarrow}{\chi}(2\omega) : \vec{E}(\vec{r},\omega)\vec{E}(\vec{r},\omega) \tag{1.5}$$

is the second-order non-linear polarization proportional to the squared of the incoming field and is the source of the SH generation. The third rank tensor $\overset{\leftrightarrow}{\chi}(2\omega)$ is the second-order non-linear susceptibility, which characterizes the SH response of the medium. A typical sketch for SHG is shown in Fig. 1.1.

For a medium with inversion symmetry (e.g. a cubic crystal), the operation $(\vec{r}\rightarrow-\vec{r})$ must leave the system invariant. Using the fact that both $\vec{P}$ and $\vec{E}$ are polar vectors and that $\overset{\leftrightarrow}{\chi}$ is invariant, from Eq. (1.5) we have that,

$$\begin{aligned}\vec{P}(-\vec{r},2\omega) &= \overset{\leftrightarrow}{\chi}(2\omega)\vec{E}(-\vec{r},\omega)\vec{E}(-\vec{r},\omega) \\ -\vec{P}(\vec{r},2\omega) &= \overset{\leftrightarrow}{\chi}(2\omega)(-\vec{E}(\vec{r},\omega))(-\vec{E}(\vec{r},\omega)) \\ \vec{P}(\vec{r},2\omega) &= -\overset{\leftrightarrow}{\chi}(2\omega)\vec{E}(\vec{r},\omega)\vec{E}(\vec{r},\omega). \end{aligned} \tag{1.6}$$

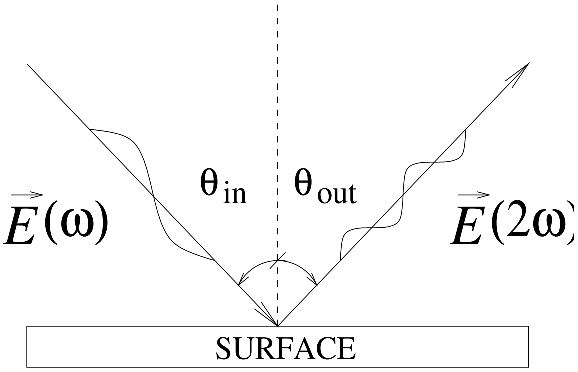

Figure 1.1: Sketch of the second harmonic generation technique. An incident electric field oscillating at the fundamental frequency ω induces a second-order non-linear optical response of the surface, thus observing in reflection a harmonic wave at 2ω.

Comparing Eq. (1.6) with Eq. (1.5) we obtain

$$\overset{\leftrightarrow}{\chi} = 0 \quad \Leftrightarrow \quad \text{inversion symmetry} \tag{1.7}$$

indicating that SHG is forbidden for centrosymmetric media. At an interface between two media where the inversion symmetry is necessarily broken, the SHG is allowed, making this technique a highly surface specific probe to analyze surfaces and interfaces.

We define the SHG efficiency as

$$\mathcal{R}(\omega) = \frac{I(2\omega)}{I^2(\omega)} \tag{1.8}$$

where the intensity $I(\omega) = (c/8\pi)|E(\omega)|^2$, then

$$\mathcal{R}(\omega) = \frac{8\pi}{c}\frac{|E(2\omega)|^2}{|E(\omega)|^4}, \tag{1.9}$$

with c the speed of light. To make a simple estimate of the order of magnitud of $\mathcal{R}$ we proceed as follows. The fact that $\overset{\leftrightarrow}{\chi}$ is different from zero only near the surface or interface of the system, allow us to make the simplifying approximation that the non-linear polarization given by Eq. (1.5) is localized within a sheet of infinitesimal width. This surface polarization P is of the order of the width of the sheet times $P(2\omega)$. We take this width to be of the order of an atomic distance, i.e. the Bohr radius a_B. On the other hand, the field radiated by such (non-linear) polarization sheet is of the order of P/λ with λ the wavelength of the radiated field, i.e. $E(2\omega) \sim P/\lambda \sim a_B P/\lambda$. From

Eq. (1.5), we notice that the units of $\overset{\leftrightarrow}{\chi}$ are those of inverse electric field (recall that $\vec{P}$ is polarization per unit volume), where the electric field is estimated to be of the order of e/a_B^2, with e the electron charge. Putting everything together into Eq. (1.9) we get

$$\begin{aligned}\mathcal{R}(\omega) &\sim \frac{1}{c}\left(\frac{a_B P}{\lambda}\right)^2 \frac{1}{E^4(\omega)} \sim \frac{1}{c}\left(\frac{a_B \chi E^2(\omega)}{\lambda}\right)^2 \frac{1}{E^4(\omega)} \sim \frac{1}{c}\left(\frac{a_B \chi}{\lambda}\right)^2 \\ &\sim \frac{1}{c}\left(\frac{a_B^3}{e\lambda}\right)^2 \sim 10^{-21} \quad \mathrm{cm}^2/\mathrm{W} \quad (\text{for } \lambda \sim \text{visible}). \end{aligned} \tag{1.10}$$

Due to the generality of this argument, this estimate can be used not only for semiconductors but also for metals, for which we expect a similar order of magnitud. However, the non-linear reflectance may still be increased in regions of resonance and suppressed in regions of transparency. The estimation of Eq. (1.10) also shows that very powerful lasers are needed to observe SHG.

Notice that, the non-linear susceptibility $\overset{\leftrightarrow}{\chi}(2\omega)$ directly reflects the structural symmetry of the surface or interface and gives us information from the surface electronic and vibrational transitions [17]. The origin of the surface SHG arises from two sources [16,18]: a) structural discontinuity as changes in the atomic positions, symmetry, electron density, as well as the presence of adsorbates at the surface and b) field discontinuity or variation of the field across the interface. The former dominates at a semiconductor surface with dangling bonds[‡] or where a monolayer (ML) [§] of molecules is adsorbed with a preferred orientation at an interface [19]. On the other hand, field discontinuity dominates on a liquid or glass surface, where the surface structure is not different from that in the bulk. Based on the origin of the SHG, we can define an interface layer as the region where both the structure and the field change significantly [18]. If the thickness of an interface layer is much smaller than the optical wavelength the long wavelength approximation can be assumed.

When higher-order effects are taken into account, the effective non-linear polarization $\vec{P}_{eff}(2\omega)$ generally should consists of a series of multipoles terms, which for a non-magnetic medium is written as

$$\vec{P}_{eff}(2\omega) = \vec{P}(2\omega) - \nabla \cdot \overset{\leftrightarrow}{\mathcal{Q}}(2\omega), \tag{1.11}$$

[‡] A dangling bond is an orbital of a surface atom of a crystal that is directed outward from the surface and is unbounded [5].

[§] One monolayer of coverage in a surface is approximately $\sim 10^{14}$ particles/cm^2 [5].

where $\vec{P}(2\omega)$ is the electric-dipole polarization and $\overset{\leftrightarrow}{\mathcal{Q}}$ is the electric-quadrupolar polarization. The terms in Eq. (1.11) are quadratic functions of the field and/or their derivatives. Up to the first derivatives of the field these terms are written as [20]

$$\vec{P}(2\omega) = \overset{\leftrightarrow}{\chi} : \vec{E}(\omega)\vec{E}(\omega) + \overset{\leftrightarrow}{\chi}{}_P^{(Q)} : \vec{E}(\omega)\nabla\vec{E}(\omega) \tag{1.12}$$

$$\overset{\leftrightarrow}{\mathcal{Q}}(2\omega) = \overset{\leftrightarrow}{\chi}{}_Q^{(Q)} : \vec{E}(\omega)\vec{E}(\omega), \tag{1.13}$$

where $\overset{\leftrightarrow}{\chi}{}^{(Q)}$ is a fourth rank tensor that describes the electric quadrupolar contributions. Defining a general susceptibility $\overset{\leftrightarrow}{\chi}{}^{(Q)}$ as

$$\overset{\leftrightarrow}{\chi}{}^{(Q)}(2\omega) = \overset{\leftrightarrow}{\chi}{}_P^{(Q)}(2\omega) - 2\overset{\leftrightarrow}{\chi}{}_Q^{(Q)}(2\omega), \tag{1.14}$$

then the effective surface polarization can be written as

$$\vec{P}_{eff}(2\omega) = \overset{\leftrightarrow}{\chi} : \vec{E}(\omega)\vec{E}(\omega) + \overset{\leftrightarrow}{\chi}{}^{(Q)} : \vec{E}(\omega)\nabla\vec{E}(\omega) - (\nabla\overset{\leftrightarrow}{\chi}{}^{(Q)}) : \vec{E}(\omega)\vec{E}(\omega). \tag{1.15}$$

The first term is the electric dipole contribution and the others are electric quadrupolar contributions. The second term is related to the field gradient across the interface; the third term is zero in the bulk of a homogeneous medium, but has a non-zero value at the surface due to structural discontinuity [21]. Note that the first two terms in Eq. (1.15) depend on the electric field or its variation in the surface region whereas the third term, although originating from the surface, only depends on bulk parameters [20].

On the other hand, the bulk contribution to surface SHG from a centrosymmetric medium should also be added [20], i.e. the non-vanishing electric quadrupolar bulk contribution to the non-linear polarization, which is related to the small but finite field gradient within a homogeneous system (second term of Eq. (1.15), since the others are identically zero in the bulk). Then the non-zero contribution from the bulk to the second-order polarization is

$$\vec{P}_b = \overset{\leftrightarrow}{\chi}{}^{(Q)} : \vec{E}(\omega)\nabla\vec{E}(\omega). \tag{1.16}$$

Measurements of SHG from the interface allows us to deduce the surface non-linear susceptibility. In such measurements the bulk may contribute to the signal at most to the same order of magnitud and may complicate the experiment since the detector collects the total SHG signal contributed by both the surface and the bulk [22]. However, in media with large dielectric constant such as metals and semiconductors, the contribution from the bulk is much weaker [18]. For some surfaces, the bulk contribution is at least an order of magnitud smaller than the surface term, and can be safely neglected [8, 18, 21, 23, 24].

The first experimental method used to detect SHG from semiconductors and metals was that of Bloembergen and coworkers [25]. They presented experimental results on the polarization and directional dependence of SHG of Si, Ge and Ag. Heinz *et al.* [19] made measurements of optical SHG spectra of adsorbates at submonolayers coverages. They obtained the position and the lineshape of the electronic transition for rhodamine-dye molecules adsorbed onto a fused silica. More recently, we can found in the literature experimental studies on SHG as a selective tool to probe excitons on NiO and CuCl surfaces [26] or for magnetized surfaces [27]. For semiconductors, the technique of SHG has been applied to the Si surface. For instance, we find experiments on the clean or oxide surface [21, 28–30], on the clean or H-adsorbed surface [31–33] and the B-doped surface [34].

On the theoretical side, different approaches for studying SHG at surfaces have been developed [8,24,35–47]. We find in the literature the early theoretical work of transmitted and reflected SHG of light waves at the boundary of non-linear media of Bloembergen and Pershan [35]. Rudnick and Stern [48] made a theoretical scheme for the calculation of the microscopic susceptibility components for a flat metallic surface with some limitations. Aksipetrov *et al.* [36] carried out an analysis of SHG in crystals showing the possibility of separating out the non-linear optical contribution from the layer near the surface. Later, Sipe *et al.* [37] developed a phenomenological analysis of the surface and bulk susceptibility tensors, identifying their independent components, and the possible functional dependence of the second-order reflectance on the incidence and azimuthal angles for different crystal surfaces. However, they did not attempt actual calculations of the susceptibility tensor. Mizrahi and Sipe [38] applied a Green method to calculate the essential measurable parameters of SHG at surfaces, in terms of the surface non-linear susceptibility. Models for the calculation of the non-linear susceptibility can be classified according to phenomenological and microscopic models. In the first class, one approximates the susceptibility with simple expressions, usually those of a harmonic oscillators and adjust, somehow, this expression to, usually, linear optical data. The second class uses a quantum mechanical expressions for the non-linear susceptibility and evaluates them according to semi-empirical tight-binding (SETB) and *ab initio* methods. Both approaches have been applied to semiconducting and metallic surfaces.

For metallic surfaces employing hydrodynamic phenomenological models see Refs.

49–56. For instance, Mochán and Mendoza use a phenomenological model which accounts for local-field effects to calculate SHG for Ag [40]. Maytorena *et al.* [53] uses the hydrodynamic model to study metallic surfaces [53–55]. They calculate SHG of semi-infinite metals taking into account the presence of a continuos electronic density profile at their surface [53]. They extend this model for the non-linear response of a conductor with a continuos electron density profile taking into account non-local effects [56]. Besides, within the hydrodynamic model, Maytorena *et al.* [56] developed a model to calculate the optical sum (SFG) and difference (DFG) frequency generation spectra at the surface of isotropic centrosymmetric conductors. They follow two approaches. One of them, consists of a semi-infinite free electron gas (jellium model) with a continuously varying electronic density profile. The other consists of a continuos distribution of polarizable entities (dipolium model) that respond non-linearly to the gradient of the field. Later Mendoza *et al.* [57] combine these approaches, the jellium model and the dipolium model, to calculate SFG/DFG at the interface of an isotropic centrosymmetric metal covered by a non-centrosymmetric adsorbate. Microscopic models to study the non-linear optical response, for simple metals, we find self consistent calculations employing the time dependent local density approximation (TDLDA) applied to the jellium model [52, 58–62].

For SHG at semiconductors surfaces employing phenomenological models we find, for example, the model of Schaich and Mendoza [39] where local field effects are taking into account. Here the system is considered to be composed of polarizable entities. With this approach, Mendoza and Mochán [24] gave simple analytical expressions modeling a centrosymmetric semi-infinite system by a homogeneous distribution of dipoles that respond harmonically to the perturbing field. Also, this approach was applied to Si surfaces by considering the crystal made up of a pointlike polarizable bonds [8, 24, 63]. On the other hand, within the microscopic models for SHG at semiconductors surfaces we can find for example the followings approaches: Levine [64] set down formulas for the second-order non-linear longitudinal response in semiconductors in a one electron, self consistent-field formalism. Sipe and Gharamani [65] presented a formalism for the calculation of the non-linear optical response of semiconductors within the independent-particle approximation. They presented the contribution to the non-linear susceptibility for CdTe from a full band structure. Gavrilenko and Rebentrost used the SETB method with a sp^3s^* basis to calculate the χ_{zzz} component [43, 44] of Si surfaces. Cini proposed a microscopic formalism for SHG [66]. He found closed expressions for the SH intensity. The theory allows to study SHG as a function of substrate band structure and plasma frequency, overlayer chemical properties and experimental geometry. Such a model has been successfully applied in the microscopic calculations for semiconductors of Refs. 42 and 45. More recently Gavrilenko *et al.* [46] and Mendoza *et al.* [47] reported results from *ab initio* theory and modified SETB method for SHG of the Si(100) surface. Gavrilenko *et al.* [46] quantitatively studied the non-linear response of Si(100) to H and Ge adatoms at Si(100)2×1 surfaces whereas Mendoza *et al.* studied Si(100)c(4×2) surfaces with H adsorption [47].

Because the technological importance of Si, the optical techniques described above, RAS [67, 68] and SHG [29, 31, 32, 34, 69], have been applied extensively to study different aspects of the Si(100) and Si(111) surfaces with different reconstructions[¶], ad-atom coverage, etc. [21, 23, 31, 32, 69–73]. Most of the studies have dealt with the (100) surface because most electronic devices are formed on this surface. The interest has been focused on understanding the basic physical properties of the clean surface, its growth, the process of adsorption of foreign atoms, etc. showing how this particular spectroscopy (SHG) is becoming a reliable surface tool.

1.1 Scope of this thesis

In this thesis, we theoretically study the optical properties of surfaces through the optical techniques of RAS and SHG. Being the silicon surface the most used in technology, we study, on one side, the clean Si(100) recontructed surface and on the other side, the clean and H-adsorbed and B-doped Si(100) reconstructed surface. The thesis is organized as follows: First, in Chap. 2, we give the basic background to calculate the optical spectra of RAS and SHG. Then in Chap. 3, we describe the method to calculate both RAS and SHG spectra based on the discrete dipole model. This model is applied to calculate the optical spectra of fully relaxed (i.e. reconstructed) Si(100) surfaces in which the polarizable entities replace each Si-Si bond. In order to understand the origin of the SHG structures seen in the spectrum, in Chap. 4, we develop a method to systematically investigate the different contributions to the observed peaks in SHG at surfaces. In particular, the clean Si(100)c(4×2) surface spectrum is analyzed through this method. We then use in Chap. 5 a microscopic formalism to calculate the SH spectra of adsorbed-covered and doped Si(100) surface. The charge transfer that arises as the surface reconstructs in the presence adsorbates generates a surface localized dc-electric field in the subsurface region.

[¶] The rearrangement of the atoms on a surface lowering the translational symmetry of the surface layers is called surface reconstruction.

We include such a dc-electric field in the calculations for SHG with adsorption of H and incorporation of B on the Si(100) surface. We finally summarize the main results of this thesis and give conclusions in Chap. 6.

Chapter 2

RAS and SHG at surfaces

2.1 Introduction

The interaction of an electromagnetic field of optical frequency ω, with a medium can be described by the induced polarization $\vec{P}(\omega)$ which contains harmonics (see Eq. (1.3)). This polarization is the source of the optical response of the medium, i.e. it generates new electromagnetic waves at the harmonic frequencies $\omega, 2\omega, 3\omega, \cdots$. The polarization can be written as an expansion of the electric field in the form[*]

$$\vec{P}(\omega) = \overset{\leftrightarrow}{\alpha}(\omega) \cdot \vec{E}(\omega) + \overset{\leftrightarrow}{\chi}(\omega) : \vec{E}\vec{E} + \cdots \tag{2.1}$$

where $\overset{\leftrightarrow}{\alpha}(\omega)$ is the linear polarizability which is related to the dielectric function $\epsilon(\omega)$ through the equation

$$\overset{\leftrightarrow}{\epsilon}(\omega) = 1 + 4\pi\overset{\leftrightarrow}{\alpha}(\omega). \tag{2.2}$$

The terms proportional to higher orders on the field, in Eq. (2.1), describe the non-linear response. The tensor $\overset{\leftrightarrow}{\chi}(\omega)$ is the second-order non-linear susceptibility responsible for the following processes: second harmonic generation (SHG), sum frequency generation (SFG), difference frequency generation (DFG), optical rectification and the Pockels effect

---

[*] The standard notation of the polarization written as an expansion of the electric field is

$$\vec{P}(\omega) = \overset{\leftrightarrow}{\chi}^{(1)}(\omega) \cdot \vec{E}(\omega) + \overset{\leftrightarrow}{\chi}^{(2)}(\omega) : \vec{E}\vec{E} + \cdots$$

Throughout this thesis, we use $\overset{\leftrightarrow}{\alpha}$ instead of $\overset{\leftrightarrow}{\chi}^{(1)}$ and $\overset{\leftrightarrow}{\chi}$ instead of $\overset{\leftrightarrow}{\chi}^{(2)}$.

[74].

The expansion of the polarization into powers of $\vec{E}$ is valid as long as the condition $E/E_{at} << 1$ holds, with E_{at} the atomic electric field. Typically $E_{at} \sim 3 \times 10^8\,\mathrm{V/cm}$. A laser beam of $1\,\mathrm{kW/cm^2}$ of power produces an electric field $\sim 10^6\,\mathrm{V/cm}$ then we have $E/E_{at} \approx 10^{-2}$. It means that the non-linear polarization is much weaker than the linear polarization [74]. This suggests that the observation of SHG requires high-intensity laser beams.

The linear and non-linear susceptibilities characterize the optical properties of media and are properly determined with a full quantum-mechanical calculation, however, simple phenomenological models help to get an insight of the origin of the optical response. Describing the physical properties of a crystalline medium one encounters with symmetry relations that the susceptibilities must satisfy. Since in this thesis, we study Si surfaces, in the next section, we go through the symmetry relations that the second-order non-linear susceptibility must hold for a centrosymmetric medium.

2.2 Symmetry of $\overset{\leftrightarrow}{\chi}$

The polarization of a crystal depends on the direction in which the external field $\vec{E}$ is applied. If $\vec{E}$ is applied in a certain direction in a crystal there will be a component of the polarization in that direction and also there may be components of the polarization in the direction perpendicular to $\vec{E}$. The existence of these perpendicular components depends on the symmetry of the crystal. Such a symmetry information is described by the susceptibilities tensors of the medium [5]. The Neumann's principle is then used to find the relationship of the different susceptibility components of the crystal.

The Neumann's principle states that any macroscopic physical property of a crystal has at least the symmetry of the point group of the space group. Restating this principle in the language of symmetry: any macroscopic physical property of a crystal, that is each component of the susceptibility tensor, transforms into +1 times itself under a symmetry operation of the point group of the crystal [5].

Consider the expression for the second-order sum frequency polarization

Face	χ_{ijk}
(100)	χ_{zzz}, $\chi_{zzx} = \chi_{zzy}$, $\chi_{zxx} = \chi_{zyy}$
(110)	χ_{zzz}, χ_{zzx}, χ_{zzy}, χ_{zxx}, χ_{zyy}
(111)	χ_{zzz}, $\chi_{zzx} = \chi_{zzy}$, $\chi_{zxx} = \chi_{zyy}$, $\chi_{xxx} = -\chi_{xyy} = -\chi_{yyx}$

Table 2.1: Independent components of the second-order susceptibility of the Si surface for its different faces.

$$P_i(\omega = \omega_1 + \omega_2) = \chi_{ijk} E_j(\omega_1) E_k(\omega_2), \tag{2.3}$$

each component of the susceptibility tensor $\overset{\leftrightarrow}{\chi}$ has to be invariant under any symmetry operation of the point group. This may reduce the number of independent and non-zero components. For instance, a general third rank tensor $\overset{\leftrightarrow}{\chi}$ in Eq. (2.3) has in principle 27 components. However for SHG ($\omega_1 = \omega_2$), the order of the last two indices, in Eq. (2.3), is arbitrary, i.e.

$$\chi_{ijk} = \chi_{ikj} \tag{2.4}$$

reducing the number of independent components to 18. This number might be reduced further by the point group symmetry. For instance, Table 2.1 shows the independent components of the Si surface for its different faces. For the diamond structure we may obtain other non-zero components of $\overset{\leftrightarrow}{\chi}$ since the microscopic symmetry of a face may be less than the macroscopic symmetry. For example, the (001) face has on the average the same symmetry as a square which yields the non-zero components shown in Table 2.1. However, if we look at a microscopic region, the displacement between the first and second crystalline planes might have a component along a square diagonal, say the [110] direction, which would therefore be inequivalent to the second diagonal in the $[1\bar{1}0]$ direction. This allows a non-zero value for χ_{zxy}. Nevertheless, any surface has steps so that on other microscopic regions the roles of the [110] and $[1\bar{1}0]$ directions are reversed and so is the sign of χ_{zxy}. Only after averaging over both kinds of regions, i.e. over the macroscopic region being illuminated by the beam, that the contribution to the surface polarization coming from χ_{zxy} cancels out, regaining the full symmetry of the square [8] as if $\chi_{zxy} = 0$.

2.3 Reflectance anisotropy spectroscopy (RAS)

The technique of of Differential reflectance spectroscopy (DRS) is very useful to investigate the optical properties of surfaces. The technique is based on measuring surface reflectivity changes. The first work in this direction is that of McIntyre and Aspnes [13]. They proposed a three layer model to find expressions for the reflection coefficient of a semi-infinite crystal taking into account the surface contribution. The relative deviation ($\Delta R_s/R_s$) from Fresnel formulas [75] of reflection according to McIntyre and Aspnes is given by

$$\frac{\Delta R_s}{R_s} = \frac{4\omega d}{c} cos\theta \, \Im m \left(\frac{\epsilon_s - \epsilon_b}{\epsilon_b - 1} \right) \tag{2.5}$$

for light polarized perpendicular to the plane of incidence (s-polarized light). Here $\Delta R_s = R_s - R_0$ is the difference between the reflection coefficient of the surface with the Fresnel reflection coefficient R_0, ω is the frequency, c the velocity of light, d is the layer thickness of the surface, θ is the angle of incidence and ϵ_s (ϵ_b) is the complex dielectric constant of the surface (bulk) which depends on frequency. For light polarized within the plane of incidence (p-polarized light) we have

$$\frac{\Delta R_p}{R_p} = \frac{4\omega d}{c} cos\theta \, \Im m \left\{ \frac{(\epsilon_b - sin^2\theta)(\epsilon_s - \epsilon_b) + \epsilon^2 sin^2\theta(\epsilon_s^{-1} - \epsilon_b^{-1})}{(\epsilon_b - 1)(\epsilon_b cos^2\theta - sin^2\theta)} \right\} \tag{2.6}$$

At normal incidence Eqs. (2.5) and (2.6) reduce to

$$\frac{\Delta R}{R} = \frac{4\omega d}{c} \Im m \left(\frac{\epsilon_s - \epsilon_b}{\epsilon_b - 1} \right) \tag{2.7}$$

The above equations for $\Delta R/R$ are valid as long as $\omega d/c << 1$, which holds for visible light.

An alternative approach to study surface optical properties of solids, is the reflectance anisotropy spectroscopy (RAS). This technique is based on DRS and is used to probe structural anisotropies on surfaces. Del Sole, based on a microscopic model, found expressions for the reflection coefficients where the anisotropy of the crystal was taken into account [76]. His result for the reflection coefficient of normally incident light in the α direction is

$$\frac{\Delta R_\alpha}{R_0} = \frac{4\omega d}{c} \Im m \left(\frac{\Delta \epsilon_{\alpha\alpha}}{\epsilon_b - 1} \right) \tag{2.8}$$

where $\Delta\epsilon_{\alpha\alpha}$ is a small perturbation to the microscopic dielectric function $\epsilon_{\alpha\beta}(z,z';\omega)$ of the vacuum-crystal surface which is given by

$$\begin{aligned}\Delta\epsilon_{\alpha\alpha}(\omega) &= \int\int \mathrm{d}z\mathrm{d}z'[\epsilon_{\alpha\alpha}(z,z';\omega)-\delta(z-z')] \\ &\quad - \int \mathrm{d}z \int \mathrm{d}z' \int \mathrm{d}z'' \int \mathrm{d}z''' \epsilon_{\alpha z}(z,z';\omega)\epsilon^{-1}_{zz}(z',z'';\omega)\epsilon_{z\alpha}(z'',z''';\omega).\end{aligned} \tag{2.9}$$

where $\delta(z-z')$ is the delta de Dirac and the integrals are evaluated from $-\infty$ to ∞. The reflection coefficient, Eq. (2.8), may take excitonic and local field effects into account, provided the macroscopic dielectric tensor defined in Ref. 77 for a semi-infinite crystal is used.

We define the RAS parameter as the difference between the ratios $\Delta R_y/R_0$ and $\Delta R_x/R_0$ of equation (2.8), i.e.

$$\begin{aligned}\mathrm{RAS} &= \frac{\Delta R_y - \Delta R_x}{R_0} \\ &= \frac{4\omega d}{c}\Im m\left(\frac{\Delta\epsilon_{yy}-\Delta\epsilon_{xx}}{\epsilon_b - 1}\right).\end{aligned} \tag{2.10}$$

Therefore, RAS measures changes in reflectance as a function of light polarized along two orthogonal directions in the surface plane.

On the other hand, Mochán and Barrera developed a simple model of polarizable entities for RAS [6], which is complementary to the microscopic model of Del Sole [77]. The model of plarizable entities, takes the local field effect into account, through the polarization near the surface and in the bulk. Mochán and Barrera found the following expression for RAS

$$\mathrm{RAS} = -4a\frac{\omega}{c}\,\Re e(i[\mathcal{P}_x - \mathcal{P}_y]), \tag{2.11}$$

with

$$\mathcal{P}_{x,y} = \sum_{n\geq 0}\left(\frac{\mathsf{P}^{(n)}_{x,y}(\omega)}{P_{x,y}(B,\omega)} - 1\right), \tag{2.12}$$

where $\mathsf{P}^{(n)}_i$ is the dipole moment per unit volume along the i-direction of any dipole in the nth plane, $P_i(B,\omega)$ is the bulk polarization along the i-direction and a is the distance between crystal planes. In this thesis we use Eq. (2.11) to calculate RAS.

2.4 Second harmonic generation (SHG)

The surface SHG is an electromagnetic phenomenon governed by Maxwell's equations. The source of the output radiation at frequency 2ω is the surface polarization, Eq. (1.5), induced by the incoming field $\vec{E}$ at the surface. Solution of the Maxwell's equations with the second-order non-linear polarization as the source term yields a second harmonic (SH) intensity $I(2\omega)$ in the reflected direction through which we define the SH generation efficiency as the ratio of the reflected intensity at the harmonic frequency to the square intensity at the fundamental frequency

$$\mathcal{R}(\omega) = \frac{I(2\omega)}{I^2(\omega)}. \tag{2.13}$$

This expression for $\mathcal{R}$ can be given in terms of the non-linear susceptibilities as [45]

$$\mathcal{R}(\omega) = \frac{32\pi^3}{(n_0 e)^2 c^3}\omega^2 \tan^2\theta |T_P(2\omega)T_i^2(\omega) r_{Pi}|^2, \tag{2.14}$$

where $i = s, p$ indicates the polarization of the input field at frequency ω. For the combinations of input polarization, r_{Pi} is given by

$$\begin{aligned} r_{Pp} = \quad & \sin^2\theta \chi_{\perp\perp\perp} + (c/\omega)^2 k_\perp^2(\omega)\chi_{\perp\parallel\parallel} \\ & -(c/\omega)^2 k_\perp(\omega)k_\perp(2\omega)\chi_{\parallel\parallel\perp}, \end{aligned} \tag{2.15a}$$

$$r_{Ps} = \chi_{\perp\parallel\parallel}, \tag{2.15b}$$

Here, θ is the angle of incidence, c the speed of light, n_0 is the electron density of the system, T_i is the transmission Fresnel factor for the i polarization and, $k_\perp = (\omega/c)[\epsilon_b(\omega) - \sin^2\theta]^{1/2}$ with $\epsilon_b(\omega)$ being the bulk dielectric function. The s-polarized SHG efficiency is identically zero due to symmetry considerations. Equation (2.14) is strictly valid within the dipole approximation. Nevertheless, even if quadrupolar corrections are considered, the isotropic and anisotropic bulk quadrupole terms in $\mathcal{R}(\omega)$ have shown to yield negligible contributions as compared to the dipole terms [8, 24, 33].

Chapter 3

Polarizable bond model

3.1 Introduction

A complete description of second-order non-linear effects at surfaces and interfaces must certainly explain the origin of the non-linear response in terms of microscopic quantities. A simple model that gives an explicit account of the microscopic crystalline effects is that which is based on treating the material as an ordered array of point-like, polarizable entities, which is referred to discrete dipole model [6, 8, 24, 39, 78]. In an external field each entity develops various multipoles moments which, in turn, produce fields that influence its neighbors. The self-consistent solution for the net polarization of the system allows one to calculate the various parameters introduced by the phenomenological theory. Within the discrete dipole model the geometrical arrangement of the atoms at the surface is incorporated through the surface local field effect (i.e. the change in the local field near the surface).

The polarization induced in a semiconductor originates from the displacement of its charge distribution. This charge distribution typically has a strong maxima at the middle of each bond for mono-atomic semiconductors with the exception of diamond, which has a bimodal distribution [74]. Thus, the *polarizable bond model* is based on treating the semiconductor as that of a lattice of point-like polarizable bonds. The model was used previously by Mochán and Barrera [6, 78] for the linear response of clean and Br-adsorbed Ge surface where they show that the local field effect induces a change in the macroscopic dielectric response of cubic crystals near their surface. This change depends on the orientation of the surface and of the plane of incidence, so that the optical properties such as reflectance, ellipsometric coefficients and surface-plasmon-polariton propagation also depend on orientation of the surface. On the other hand, Schaich and Mendoza [39] developed a model for surface second harmonic generation (SHG) consisting of a semi-infinite system made up of a continuos distribution of polarizable entities. The model was developed for the unreconstructed silicon surface by Mendoza and Mochán [8,24] and in the following that theory is applied to analyze 2×1 and c(4×2) reconstructed Si(100) surfaces. Part of this work is reported in Ref. 79.

We expect the local field to have large consequences in SHG through the following mechanism: Consider a localized polarizable entity and a semi-infinite crystal made up of its replicas. If each entity is centrosymmetric it would have no electric-dipole-allowed second harmonic (SH) transition, though it may have electric-quadrupolar and magnetic-dipolar contributions proportional to $\vec{\mathcal{E}}\nabla\vec{\mathcal{E}}$ where $\mathcal{E}_i$ is the local field acting at site i. The external field has a very slow spatial variation whose scale is of the order of the wavelength λ, although the field induced by a nearby entity j may have a very large variation, with a scale determined by the distance from j to i, r_{ij}, which is of atomic dimensions a. Different neighbors contribute to the gradient $\nabla\vec{\mathcal{E}}$ along different directions, so that, if the site i is itself centrosymmetric, these large gradients will cancel out among themselves, leaving only a small residual gradient of the order $\mathcal{E}/\lambda$. This cancellation is no longer possible at the surface, where $|\nabla\mathcal{E}| \approx \mathcal{E}/a$, yielding a large SH surface polarization. When written in terms of the microscopic field $\vec{E}$ this surface polarization is then proportional to $\vec{E}\vec{E}/a$, which corresponds to a large surface allowed dipolar SH process.

The chapter is organized as follows: in Secs. 3.2-3.7 we give expressions for the non-linear susceptibilities of each bond in terms of its linear polarizabilities. Then, in Secs. 3.4 and 3.5, we set up the linear and non-linear equations used to calculate the polarization of the crystal and finally in Sec. 3.6 we present reflectance anisotropy (RAS) and SHG spectra calculations for the Si(100) reconstructed surface and compare with available experimental spectra.

3.2 Microscopic linear polarizability

The polarizable bond model treats the crystal as an array of point-like dipoles. Then, we first treat an individual dipole (a single bond). We consider every dipole to be an anisotropic point-like harmonic oscillator of cylindrical symmetry, with charge e and mass m. The x coordinate axis is chosen to be along the symmetry axis and the y, z axes perpendicular to it. We denote the resonant frequencies of the dipole by $\omega_x = \omega_\|$ corresponding to the response parallel and by $\omega_y = \omega_z = \omega_\perp$ corresponding to the response perpendicular to the bond.

The first order induced dipole moment is written as [39]

$$\vec{p}(\omega) = \overset{\leftrightarrow}{\alpha}(\omega) \cdot \vec{\mathcal{E}}, \tag{3.1}$$

where $\vec{\mathcal{E}}$ is the local field and the linear microscopic polarizability $\overset{\leftrightarrow}{\alpha}(\omega)$ tensor is given by

$$\alpha_{ij}(\omega) = \begin{pmatrix} \alpha_\|(\omega) & 0 & 0 \\ 0 & \alpha_\perp(\omega) & 0 \\ 0 & 0 & \alpha_\perp(\omega) \end{pmatrix}. \tag{3.2}$$

To emphasize the dependence on each bond's orientation the following notation has been used: $\alpha_{xx} \rightarrow \alpha_\|$ and $\alpha_{yy} = \alpha_{zz} \rightarrow \alpha_\perp$ for its response parallel and perpendicular to the bond respectively and

$$\alpha_i(\omega) = \frac{e^2/m}{\omega_i^2 - \omega^2}, \tag{3.3}$$

with $i =\|$ or $\perp$. The cylindrical symmetry allows the polarizability to be written in the crystal coordinate system as

$$\overset{\leftrightarrow}{\alpha} = \alpha_\| \hat{e}^\lambda \hat{e}^\lambda + \alpha_\perp (\overset{\leftrightarrow}{\mathbf{1}} - e^\lambda e^\lambda), \tag{3.4}$$

where $\overset{\leftrightarrow}{\mathbf{1}}$ is the unitary tensor and $\hat{e}^\lambda$ is the unitary vector along the direction of the λ bond. The microscopic polarizability of each dipole, indeed, depends on its position through its particular bond orientation and its surface or bulk location.

3.3 Microscopic non-linear susceptibilities

Once we have defined in Sec. 3.2, the linear polarizability that describe the linear response of a polarizable entity, we go on describing the non-linear susceptibilities that describe the second order response. The second-order induced dipole moment is given by [8,39]

$$(\vec{p}_{n\lambda}(2\omega))_i = [\chi^{(d)}_{ijkl}(\omega) + \chi^{(m)}_{ijkl}(\omega)]\mathcal{E}_j(\nabla_k \mathcal{E}_l), \tag{3.5}$$

with*

$$\chi^{(d)}_{ijkl}(\omega) = \frac{1}{2e}[\alpha_{il}(2\omega)\alpha_{jk}(\omega) + \alpha_{ik}(2\omega)\alpha_{jl}(\omega)], \tag{3.6}$$

$$\chi^{(m)}_{ijkl}(\omega) = \frac{3}{2e}[\alpha_{il}(2\omega)\alpha_{jk}(\omega) - \alpha_{ik}(2\omega)\alpha_{jl}(\omega)]. \tag{3.7}$$

Here $\overset{\leftrightarrow}{\chi}^{(d)}$ and $\overset{\leftrightarrow}{\chi}^{(m)}$ are the dipolar and magnetic originated contributions to the microscopic second-order susceptibility of the dipole oscillator. Then, Eqs. (3.6) and (3.7) are simple relations between the non-linear susceptibilities (dipolar and quadrupolar) with the linear polarizability for harmonic oscillators [8,39]. Finally, the second-order induced electric quadrupolar moment is

$$Q_{ij}(2\omega) = \chi^{(Q)}_{ijkl}(\omega)\mathcal{E}_k\mathcal{E}_l, \tag{3.8}$$

where $\chi^{(Q)}_{ijkl}(\omega)$ is the quadrupolar susceptibility given by [8,39]

$$\chi^{(Q)}_{ijkl}(\omega) = \frac{1}{2e}[\alpha_{il}(\omega)\alpha_{jk}(\omega) + \alpha_{ik}(\omega)\alpha_{jl}(\omega)]. \tag{3.9}$$

---

*Eqs. (3.6)-(3.9) arise by obtaining the second-order change in the expectation value of the multipole moments [39] for a harmonic oscillator with charge $e < 0$, mass m and frequency ω. The calculation is based on a quantum mechanical scheme based on raising and lowering operators for the position operator. Within the time dependent perturbation theory, the second-order response of an operator $\hat{O}$ due to a perturbation $\hat{\mathcal{H}}'$ is given by

$$< \delta\hat{O}^{(2)}(2\omega) >= \left(\frac{1}{i\hbar}\right)^2 \int_0^\infty \mathrm{d}\tau_1 e^{i\omega\tau_1} \int_{\tau_1}^\infty \mathrm{d}\tau_2 e^{i\omega\tau_2} < [[\hat{O}, \hat{\mathcal{H}}'(-\tau_1)], \hat{\mathcal{H}}'(-\tau_2)] > .$$

Calculating the change in the electric-dipole moment $\hat{p}_i$ (magnetic-dipole moment $\hat{m}_i$) with the perturbations $\hat{\mathcal{H}}' \sim -ex_jE_j(L)$ and $\hat{\mathcal{H}}' \sim -1/2ex_jx_k(\partial_jE_k)_L$ ($\hat{\mathcal{H}}' \sim -m_jB_j(L)$), Eqs. (3.6) and (3.7) arise. Whereas obtaining the change in the quadrupole moment $\hat{Q}_{ij}$ with the perturbation $\hat{\mathcal{H}}' \sim -ex_j\vec{E}_j(L)$, Eq. (3.9) arises. Here, x is the position operator, $E(L)$ ($B_j(L)$) is the local electric (magnetic) field at the site of the entity.

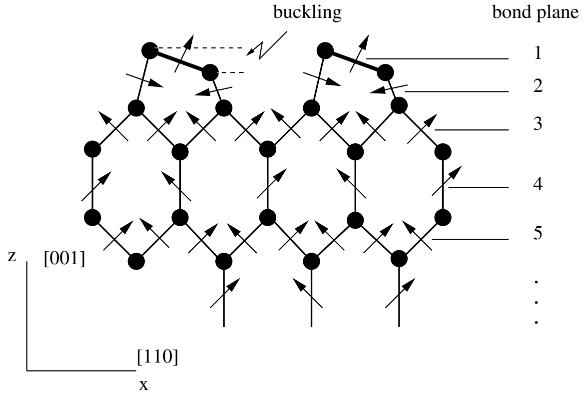

Figure 3.1: We show the 2×1 reconstructed surface of clean Si(100). The arrows represent the point-like dipoles that replace each Si-Si bond, where the dimer has a thicker line. The bond-plane enumeration is also shown.

The microscopic susceptibilities $\overset{\leftrightarrow}{\alpha}$ and $\chi^{(d),(m),(Q)}$ of a single oscillator given by expressions (3.2), (3.6), (3.7) and (3.9) respectively determine all the relevant response functions within the long wavelength limit.

It can be seen also from these equations, that from the knowledge of the linear polarizabilities $\alpha_i(\omega)$ the non-linear susceptibilities, for a single dipole, can be obtained (by substitution of Eq. (3.4) into Eqs. (3.6), (3.7) and (3.9)) and therefore, the total microscopic non-linear behavior as well.

3.4 Linear local field equations

The total polarization of a medium to an external field would be the sum of the dipole moments of each dipole that forms the system. Then we will set up the equations that give the linear dipole moment of every polarizable entity of the medium, which in turn give us the total linear response of the system. Then, the total induced linear dipole moment of every dipole that is in a plane ℓ and that has an orientation λ (see. Fig. 3.1) is given by Eq. (3.1) which is written in the form

$$\vec{p}_{\ell\nu\lambda}(\omega) = \overset{\leftrightarrow}{\alpha}^{\ell\nu\lambda}(\omega) \cdot \left(\vec{E}^{(ext)}(\vec{r}_{\ell\nu\lambda}, \omega) + \sum_{\ell'\nu'\lambda'} \overset{\leftrightarrow}{M}_{\ell\nu\lambda\ell'\nu'\lambda'} \cdot \vec{p}_{\ell'\nu'\lambda'}(\omega) \right) \tag{3.10}$$

where ν numbers the individuals dipoles that make up the plane ℓ with the same orientation λ. The term in parentheses in Eq. (3.10) is the local field $\vec{\mathcal{E}}$ which is the sum of the external field $\vec{E}^{(ext)}$ plus the fields generated by the surroundings dipoles, $\overset{\leftrightarrow}{M}$ is the dipolar interaction tensor between dipoles $\ell\nu\lambda$ and $\ell'\nu'\lambda'$ given by

$$\overset{\leftrightarrow}{M}_{\ell\nu\lambda\ell'\nu'\lambda'} = \nabla\nabla \frac{1}{|\vec{r} - \vec{r}_{\ell'\nu'\lambda'}|}\bigg|_{\vec{r}=\vec{r}_{\ell\nu\lambda}}, \tag{3.11}$$

where the gradient operator acts over $\vec{r}$. The sum in Eq. (3.10) is over all dipoles $\ell'\nu'\lambda' \neq \ell\nu\lambda$ and can be carried out by using a planewise summation [80].

In the long wavelength approximation the slow spatial variation of the external field is neglected which allows to write $\vec{E}^{(ext)}(\vec{r}_{\ell\nu\lambda}, \omega) \to \vec{E}(A, \omega)$ with $\vec{E}(A, \omega)$ the external field independent of position. In such a case, all dipoles with the same orientation λ in a particular plane would have the same dipole moment; this permit the ν index to be dropped in the dipole moment expression, i.e. $\vec{p}_{\ell\nu\lambda} \to \vec{p}_{\ell\lambda}$ and the sum over ν' in Eq. (3.10) is carried out as

$$\overset{\leftrightarrow}{\mathcal{M}}_{\ell\lambda\ell'\lambda'} = \sum_{\nu'}{}' \overset{\leftrightarrow}{M}_{\ell\nu\lambda\ell'\nu'\lambda'}, \tag{3.12}$$

where the prime on the sum indicates that the self interaction of a dipole should be excluded, i.e. the term with $\nu = \nu'$. Equation (3.12) represents the interaction between a particular dipole $\ell\lambda$ with all the dipoles with orientation λ' that make up the plane ℓ'. Notice that the tensor $\overset{\leftrightarrow}{M}$ depends on the difference $(\vec{r}_{\ell\nu\lambda} - \vec{r}_{\ell'\nu'\lambda'})$, which means that after summing over ν' the tensor $\overset{\leftrightarrow}{\mathcal{M}}$ does not depend on ν [80].

The above considerations allow Eq. (3.10) to be rewritten in the form

$$\sum_{\ell'\lambda'} [\vec{1}\delta_{\ell\ell'}\delta_{\lambda\lambda'} - \overset{\leftrightarrow}{\alpha}^{\ell\lambda} \cdot \overset{\leftrightarrow}{\mathcal{M}}_{\ell\lambda\ell'\lambda'}] \cdot \vec{p}_{\ell'\lambda'}(\omega) = \overset{\leftrightarrow}{\alpha}^{\ell\lambda}(\omega) \cdot \vec{E}(A, \omega). \tag{3.13}$$

Expression (3.13) is a set of $3 \times \lambda \times \ell$ equations to be solved for the linear dipole moments of each dipole λ in the plane ℓ. Then the total polarization is obtained by summing the contributions of all dipoles as,

$$\vec{p}(\omega) = \sum_{\ell\lambda} \vec{p}_{\ell\lambda}(\omega), \tag{3.14}$$

The dipole moment of each dipole in the bulk is independent of the plane ℓ; in such a case $\vec{p}_{\ell\lambda} \rightarrow \vec{p}_{\lambda}(B,\omega)$ and Eq. (3.13) is rewritten as

$$\sum_{\lambda'}[\vec{1}\delta_{\lambda\lambda'} - \overleftrightarrow{\alpha}^{\lambda}\cdot\overleftrightarrow{\mathcal{U}}_{\lambda\lambda'}]\cdot\vec{p}_{\lambda'}(B,\omega) = \overleftrightarrow{\alpha}^{\lambda}(\omega)\cdot\vec{E}(A,\omega). \tag{3.15}$$

where the tensor $\overleftrightarrow{\mathcal{U}}_{\lambda\lambda'}$ that describe the interaction between dipoles is given by

$$\overleftrightarrow{\mathcal{U}}_{\lambda\lambda'} = \sum_{\ell'=-\infty}^{\infty}\overleftrightarrow{\mathcal{M}}_{\ell\lambda\ell'\lambda'}\;. \tag{3.16}$$

Again, we notice that the tensor $\overleftrightarrow{\mathcal{U}}$ does not depend on ℓ since the tensor $\overleftrightarrow{\mathcal{M}}$ depends on the difference of position between bonds $\ell\lambda$ and $\ell'\lambda'$.

Therefore the total bulk polarization is given by

$$\vec{P}(B,\omega) = \sum_{\lambda}\vec{p}_{\lambda}(B,\omega). \tag{3.17}$$

3.5 Nonlinear local field equations

We continue with the description of the non-linear response of a medium as in Sec. 3.4. The total second-order dipole moment of every dipole $\ell\nu\lambda$ is the sum of the second-order non-linear response $\vec{p}_{\ell\nu\lambda}(2\omega)$ to the spatially varying local field plus the linear response to the field at the harmonic frequency 2ω due to the oscillating quadrupoles

$$\begin{aligned}\vec{p}^{(tot)}_{\ell\nu\lambda}(2\omega) &= \vec{p}_{\ell\nu\lambda}(2\omega)\\ &\quad+\overleftrightarrow{\alpha}^{\ell\nu\lambda}(2\omega)\cdot\left(\vec{\mathcal{E}}^{(Q)}_{\ell\nu\lambda}(2\omega)+\sum_{\ell'\nu'\lambda'}\overleftrightarrow{M}_{\ell\nu\lambda\ell'\nu'\lambda'}\cdot\vec{p}^{(tot)}_{\ell'\nu'\lambda'}(2\omega)\right),\end{aligned} \tag{3.18}$$

where

$$(\vec{p}_{\ell\nu\lambda}(2\omega))_i = \chi^{(d)\ell\nu\lambda}_{ijkl}(\vec{\mathcal{E}}_{\ell\nu\lambda}(\omega))_j\nabla_l(\vec{\mathcal{E}}_{\ell\nu\lambda}(\omega))_k. \tag{3.19}$$

Expression (3.19) is obtained from Eq. (3.5) where we have neglected the magnetic contribution of the magnetic susceptibility of each bond. The second-order dipole moment is also driven by the linear response to the field at 2ω due to the oscillating quadrupoles,

$$(\vec{\mathcal{E}}^{(Q)}_{\ell\nu\lambda}(2\omega))_i = \frac{1}{2}\sum_{\ell'\nu'\lambda'}(\overset{\leftrightarrow}{N}_{\ell\nu\lambda\ell'\nu'\lambda})_{ijk}(\overset{\leftrightarrow}{Q}_{\ell'\nu'\lambda'}(2\omega))_{jk}, \tag{3.20}$$

which, with the help of Eq. (1.12), can be written as

$$(\vec{\mathcal{E}}^{(Q)}_{\ell\nu\lambda}(2\omega))_i = \frac{1}{2}\sum_{\ell'\nu'\lambda'}(\overset{\leftrightarrow}{N}_{\ell\nu\lambda\ell'\nu'\lambda})_{ijk}\chi^{(Q)\ell'\nu'\lambda'}_{jklm}(\vec{\mathcal{E}}_{\ell\nu\lambda}(\omega))_l(\vec{\mathcal{E}}_{\ell\nu\lambda}(\omega))_m. \tag{3.21}$$

Finally, the last term on the left-hand side of Eq. (3.18) represents the linear response to the field at 2ω due to the other dipoles oscillating at 2ω and should be included to achieve self consistency.

The gradient of the local field in Eq. (3.19) should be evaluated at the position of the dipoles and is proportional to the linear dipole moment as

$$\nabla_i(\vec{\mathcal{E}}_{\ell\nu\lambda}(\omega))_j = -\sum_{n'\lambda'}(\overset{\leftrightarrow}{N}_{\ell\nu\lambda\ell'\nu'\lambda'})_{ijk}(\vec{p}_{\ell'\nu'\lambda'}(\omega))_k, \tag{3.22}$$

with the interaction tensor

$$\overset{\leftrightarrow}{N}_{\ell\nu\lambda\ell'\nu'\lambda'} = -\nabla\nabla\nabla\frac{1}{|\vec{r}-\vec{r}_{\ell'\nu'\lambda'}|}\bigg|_{\vec{r}=\vec{r}_{\ell\nu\lambda}}, \tag{3.23}$$

that decays quickly as the separation between planes increases. Similarly to Eq. (3.13), Eq. (3.18) can be written as

$$\sum_{\ell'\lambda'}[\vec{1}\delta_{\ell\ell'}\delta_{\lambda\lambda'} - \overset{\leftrightarrow}{\alpha}^{\ell\lambda}(2\omega)\cdot\overset{\leftrightarrow}{\mathcal{M}}_{\ell\lambda\ell'\lambda'}]\cdot\vec{p}^{tot}_{\ell'\lambda'}(2\omega) = \vec{\mathcal{S}}_{\ell\lambda}(2\omega), \tag{3.24}$$

where $\vec{\mathcal{S}}$ is the non-linear source given by

$$\begin{aligned}(\vec{S}_{\ell\lambda}(2w))_i = & - \chi^{(d),\ell\lambda}_{ijkl}(\vec{\mathcal{E}}_{\ell\lambda}(\omega))_j\sum_{\ell'\lambda'}(\mathcal{N}_{\ell\lambda\ell'\lambda'})_{klm}(\vec{p}_{\ell'\lambda'}(\omega))_m \\ & + \frac{1}{2}\alpha^{\ell\lambda}_{ij}(2\omega)\sum_{\ell'\lambda'}(\overset{\leftrightarrow}{\mathcal{N}}_{\ell\lambda\ell'\lambda'})_{jkl}\chi^{(Q),\ell'\lambda'}_{klmn}(\vec{\mathcal{E}}_{\ell'\lambda'}(\omega))_m(\vec{\mathcal{E}}_{\ell'\lambda'}(\omega))_n,\end{aligned} \tag{3.25}$$

which is expressed in terms of the linear dipole moment $\vec{p}_{\ell\lambda}(\omega)$ (see Eq. (3.13)). The linear local field $\vec{\mathcal{E}}_{\ell\lambda}(\omega)$ is obtained through the linear dipole moment as

$$\vec{\mathcal{E}}_{\ell\lambda}(\omega) = (\overset{\leftrightarrow}{\alpha}^{\lambda}(\omega))^{-1} \cdot \vec{p}_{\ell\lambda}(\omega). \tag{3.26}$$

Equation (3.24) gives the non-linear dipole moment of each dipole that is in the plane ℓ with orientation λ. Therefore, the total surface second-order dipole moment would be the sum of the contributions of all dipoles, i.e.

$$\vec{P}^{tot}(2\omega) = \sum_{\ell\lambda} \vec{p}^{\,(tot)}_{\ell\lambda}(2\omega) \tag{3.27}$$

Notice that, in principle, the sum in Eq. (3.27) is carried out over all dipoles in the system i.e, ℓ runs from $\ell = 0$ (from the surface) to $\ell \to \infty$ (to the bulk), however since the interaction tensor between surface dipoles with bulk dipoles decays quickly with plane separation, the source $\vec{S}$ in Eq. (3.24) converges to a fixed value and thus, the total surface non-linear dipole moment $\vec{p}^{\,(tot)}_{\ell\lambda}(2\omega)$ as well. This means that we should only sum over a finite number of planes to get the total surface non-linear dipole moment.

On the other hand, we have to add the finite bulk contribution to the signal whose origin comes from the quadrupole moment [20], i.e.

$$P^{tot}_i(2\omega) \to P^{tot}_i(2\omega) - \frac{1}{2}\sum_{\lambda}(\overset{\leftrightarrow}{Q}_{\lambda}(B,2\omega))_{iz}, \tag{3.28}$$

with

$$(\overset{\leftrightarrow}{Q}_{\lambda}(B,2\omega))_{ij} = \chi^{(Q),\lambda}_{ijkl}(\vec{\mathcal{E}}(B,\omega))_k(\vec{\mathcal{E}}(B,\omega))_l \tag{3.29}$$

where $\vec{\mathcal{E}}(B,\omega)$ is the local field at the bulk.

Once the total polarization is obtained we could obtain the different susceptibility components by making use of the definition of the second order polarization Eq. (1.5). First, we fixed the external electric field $\vec{E}(A,\omega)$ in different directions; if $\vec{E}(A,\omega) = E_j(A,\omega)\hat{e}_j$, it would be possible to obtain χ_{ixx}, χ_{iyy} and χ_{izz}, with $i = x, y$ or z, through

$$P^{tot}_i = \chi_{ijj}(\omega)E_j(B,\omega)E_j(B,\omega) \tag{3.30}$$

where $\vec{E}(B,\omega)$ is the macroscopic electric field inside the medium which differs from the external electric field $\vec{E}(A,\omega)$ through the equation

$$\vec{E}(B,\omega) = (E_x(A,\omega), E_y(A,\omega), E_z(A,\omega)/\epsilon(\omega)) \tag{3.31}$$

with $\epsilon(\omega)$ the dielectric function. If now $\vec{E}(A,\omega)$ is let to have two no null components, namely, $E_j(A,\omega)$ and $E_k(A,\omega)$ with $j \neq k$, thus we have

$$P_i^{tot} = \chi_{ijj} E_j^2(B,\omega) + \chi_{ikk} E_k^2(B,\omega) + 2\chi_{ijk} E_j(B,\omega) E_k(B,\omega). \tag{3.32}$$

Knowing χ_{ijj} and χ_{ikk}, Eq. (3.32) can be solved for χ_{ijk}, generating the 27 components of $\overset{\leftrightarrow}{\chi}$. Indeed, some of these components would be identically zero due to the symmetry of the system. Then, the SHG efficiency $\mathcal{R}(\omega)$ can be calculated in terms of the non-linear susceptibilities through Eq. (2.14).

Once we have calculated the surface SHG, we have to add the bulk contribution to the surface SHG from a centrosymmetric medium. This contribution has its origin in the non-vanishing electric quadrupolar bulk contribution to the non-linear polarization which is related to the small but finite field gradient within a homogeneous system (see Chap. 1). However, as we mentioned above, such a contribution is negligible (at least an order of magnitude smaller than the surface contribution) in media with large dielectric constant such as metals and semiconductors. This is actually our case and thus, we refer the reader to see Ref. [8] for details of the bulk contribution to the SHG. Nevertheless in the following results the negligible bulk contribution has been included.

3.6 The reconstructed silicon surface

The structural reconstruction of the silicon surface has been widely studied due to its technological importance. The interest has been focused on understanding the basic physical properties of the clean surface: its growth, the process of adsorption of foreign atoms, etc. In this respect, the knowledge of the atomic structure of the clean surface is needed. It is now accepted, that the dimers (pairs of atoms) are the main structural units of the reconstructed silicon surface. Surface atoms, having two dangling bonds (per atom), are assumed to form a dimer to lower their energy, then the formation of surface dimers would remove one of the two dangling bonds per surface atom without necessarily changing any bond lengths by more than a few percent [81]. Furthermore, surface dimer-

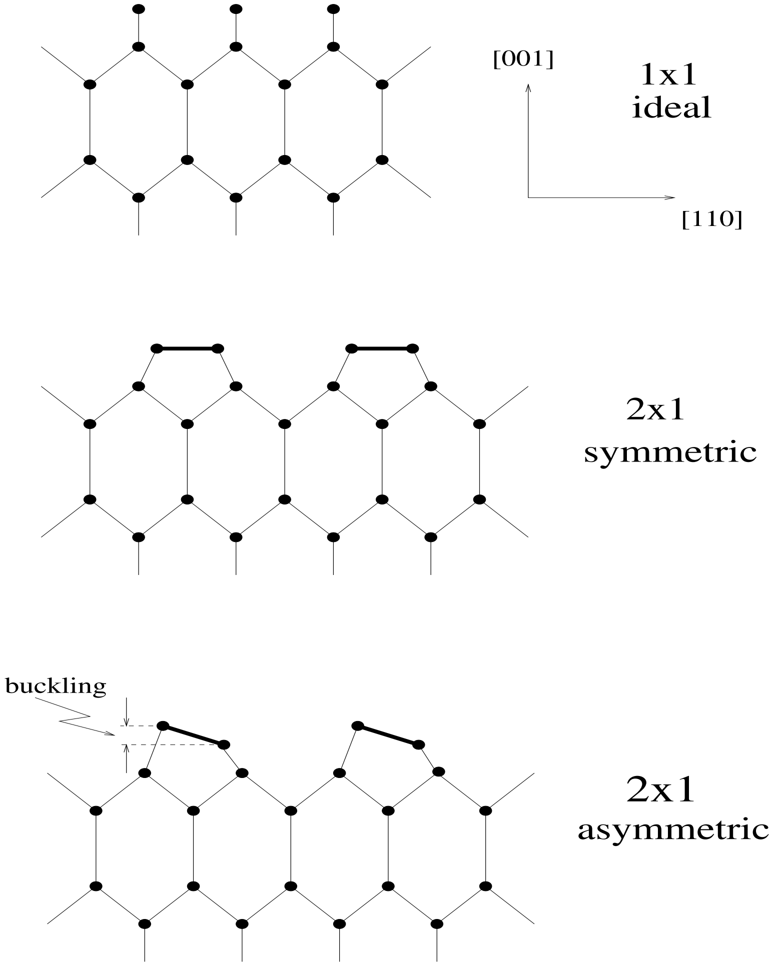

Figure 3.2: Reconstructions of the Si(100) surface: the ideal surface(top panel), 2×1 reconstructed surface with symmetric dimers (middle panel) and 2×1 reconstructed surface with asymmetric dimers (bottom panel). The dimers are shown with a thicker line.

ization introduces sizable subsurface angular strains which drive a substantial and deep reconstruction of the subsurface region that extends five atomic layers into the bulk [82]. Two different dimers models have been proposed: that of a structure with symmetric dimers and that of a structure with asymmetric dimers, where the dimers buckle out of the plane of the surface (see. Fig. 3.2). Chadi found that the energetically favorable reconstructions 2×1 and c(4×2) correspond to asymmetric dimers [83].

The optical techniques can predict the proper atomic structure due to the dependence of the selection rules on symmetry. For instance, Shkrebtii and Del Sole presented strong evidence in favor of the presence of asymmetric dimers at the Si(100)2×1 surface by a microscopic calculation of the differential reflectance, i.e. the difference between the reflectivities of the clean and oxidized surface [84], Palummo *et al.* carried out *ab initio* calculations of the optical properties of the Si(100) surface within density functional theory within the local density approximation (DFT-LDA) [11] meanwhile, Mendoza *et al.* applied a microscopic formalism to calculate the SH spectra of clean and hydrogenated Si(100) surfaces [9, 45].

3.7 Principal polarizabilities

In Secs. 3.4 and 3.5, we have set up Eqs. (3.13) and (3.24), that allow us to obtained the linear and non-linear dipole moments within the model of polarizable entities. These equations depend on the linear polarizability and the non-linear susceptibilities which also are given in terms of the linear polarizability through Eqs. 3.6 and 3.9. Thus, from the knowledge of the linear polarizability it is possible to obtain the linear and non-linear response of a medium to an external field.

We will study the Si surface and thus we describe, in this section, the procedure to follow to obtain the linear polarizability. Close to the visible spectral region, we expect that the main contributions to $\alpha_\parallel$ originate in bonding-antibonding transitions, while $\alpha_\perp$ is due mainly to transitions involving atomic states with different symmetry. We assume that $\alpha_\perp$ has larger resonant frequencies than the $\alpha_\parallel$, and we approximate $\alpha_\perp$ by a Lorentzian function, centered at some relatively high frequency $\omega_\perp$ with weight related to ω_p and damping parameter ω_c. Then,

$$\alpha_\perp(\omega) = \frac{(f\omega_p)^2}{\omega_\perp^2 - (\omega + i\omega_c)^2}, \tag{3.33}$$

where the factor f is allowed to be proportional to the amount of charge transfer to the upper Si of the dimers; ω_p has a fixed value, and the factor $f = 1$ is taken for all dipoles except that of the dimer for which $f \geq 1$.

In order to obtain $\alpha_\parallel(\omega)$, we start by using [75]

$$\vec{D} = \vec{E} + 4\pi\vec{P} \tag{3.34}$$

which relates the displacement vector field $\vec{D}$ to the electric field $\vec{E}$ through the polarization $\vec{P}$. With the help of the constitutive relation $\vec{D} = \epsilon\vec{E}$, we obtain the relation [8],

$$\vec{P}(\alpha_\parallel, \alpha_\perp) = \frac{\epsilon(\omega) - 1}{4\pi}\vec{E} \tag{3.35}$$

where the polarization should be calculated at the bulk and we have emphasized the dependence of $\vec{P}(\alpha_\parallel, \alpha_\perp)$ on the principal polarizabilities (see. Eqs. (3.13) and (3.14)). $\vec{E}(B, \omega)$ is the macroscopic electric field in the bulk and $\epsilon(\omega)$ is the bulk dielectric function of the crystal that is determined experimentally. Therefore, from Eq. (3.35) and with the help of Eq. (3.17) we can obtain $\alpha_\parallel$ from the knowledge of $\alpha_\perp$ and the experimental measurements of the dielectric function [85]. Therefore, once $\omega_\perp$, ω_p and ω_c are chosen in Eq. (3.33), equation (3.35) can be solved for $\alpha_\parallel$ for any given $\epsilon(\omega)$.

For instance, in Fig. 3.3, we show $\alpha_\parallel$ of Si as a function of frequency with the parameters $\hbar\omega_\perp = 7.17$, $\hbar\omega_p = 1.68$, $\hbar\omega_c = 0.2$ and $f = 1$. The value of $\hbar\omega_\perp$ is of the order of the transition energy between the atomic states of Si $3p^{23}P$ with $J = 0$ and $3d^3D^0$ with $J = 1$ [86], in qualitative agreement with the discussion preceding Eq. (3.33). We observe in Fig. 3.3 the usual peaks due to the singularities or the bulk density of states, although they are substantially shifted due to short range Coulomb and exchange interactions. We recall that the bulk local field effect induces an almost equal but opposite shift [87, 88].

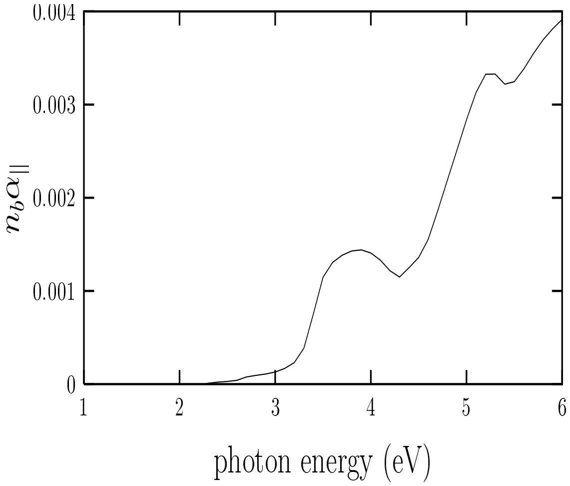

Figure 3.3: Imaginary part of the axial bond polarizability of Si as a function of frequency. The structure is shifted from the singularities of the joint density of states, due to short range Coulomb and exchange interactions, which are compensated within the bulk by the long range local field effect.

3.8 Polarizable bond model for the Si surface

In this section, we proceed to study the structure of the reconstructed Si(100) surface by using the polarizable bond model. This model has the advantage of having a simple interpretation, and has been successfully applied to Si surfaces [6,8,10,24]. For instance, the model of Mendoza and Mochán [8] supports the conclusion of Daum *et al.* [29] that the bulk E_1 transition of Si yields a SHG resonance of the clean or oxide-covered Si(100) surface due to the vertical strain induced by surface reconstruction. In Ref. 8, optical spectra SHG were calculated for the unreconstructed surface where the effect of reconstruction was incorporated by a strain induced through a vertical displacement of the first atomic plane. However, the model was not compared with RAS since no experimental data were available.

In this section, we relax the simple approximation of vertical displacement for inducing the strain, and we apply the polarizable bond model to calculate RAS and SHG spectra of fully relaxed (i.e. reconstructed) Si(100) surfaces. Within this model, the semiconductor Si crystal is treated as an array of point-like polarizable dipoles with a dipole located at the center of each Si-Si [74] bond since the maximum distribution of charge is located there (see Fig. 3.1). However, for the bond corresponding to the dimer, the actual position of the dipole may be off-centered due to the charge transfer (of $e/3$ with e the electron charge) to the upper atom that takes place as the surface reconstructs [83].

We use three atomic reconstructions characterized by their dimer buckling: 0 Å (symmetric dimers), 0.7 Å and 0.6 Å whose atomic coordinates were calculated by minimizing the total energy of the surface, Ref. 81 and Ref. 89, respectively. We take the following values for the frequency parameters of Eq. (3.33): $\hbar\omega_\perp = 7.05\,\mathrm{eV}$ for both surface (including the dimer) and bulk dipoles, and $\hbar\omega_p = 1.68\,\mathrm{eV}$. These values were obtained by finding simultaneously the best agreement with the experimental results of RAS and SHG. The value of $\hbar\omega_\perp$ is of the order of the transition energy between the atomic states of Si $3p^{2\,3}P$ with $J = 0$ and $3d^3D^0$ with $J = 1$, [86] in qualitative agreement with the discussion before Eq. (3.33). These parameters are also consistent with those used in Ref. 8. Finally we mention that the results do not depend strongly on ω_c as long as $\omega_c \ll \omega_\perp$ (we take $\hbar\omega_c = 0.2$ eV) and that a good numerical convergence occurs with ~ 80 crystalline planes. The results are compared to experimental data measured from single domain surfaces for RAS [68, 90] and double domain surfaces[†] for SHG [31, 32]. The components of $\overset{\leftrightarrow}{\chi}$ for the double domain (100) surface are obtained through

$$\chi_{\perp\perp\perp} = \chi_{zzz} \tag{3.36a}$$

$$\chi_{\perp\|\|} = (\chi_{zxx} + \chi_{zyy})/2 \tag{3.36b}$$

$$\chi_{\|\|\perp} = (\chi_{xxz} + \chi_{yyz})/2 \tag{3.36c}$$

Besides we have the relations $\chi^{I}_{zxx} = \chi^{II}_{zyy}$, and $\chi^{I}_{xxz} = \chi^{II}_{yyz}$ between susceptibility components of domains I and II.

Figure 3.4 shows RAS and the SHG spectra for the Si(100) surface. The spectra shown are for the ideal 1×1 surface, strain-relaxed surface where the last layer of atoms is relaxed inward by 5% of the interplane distance [24] and for the reconstructed 2×1 surface. It is mentioned that in these cases the same values for the frequency parameters of equation (3.33) are used, with $f = 1$, for all dipoles (including the dimers). In the RAS spectrum, we see that the ideal surface (1×1) has no structure. On the other hand,

---

[†] We refer to single domain surfaces when all the dimers of the reconstructed Si(100) surface are oriented only in one direction (domain I) whereas double domain surfaces are those where the dimers have two different orthogonal orientations (domain I and II). The RAS measurement of Si(100) requires a single domain sample since it requires the measurement of reflectance of light polarized along the directions parallel and perpendicular to the dimers. Whereas the SHG measurement may be made in a double domain sample. This fact is taken in the SHG calculations into account by considering Eqs. (3.36) for $\overset{\leftrightarrow}{\chi}$.

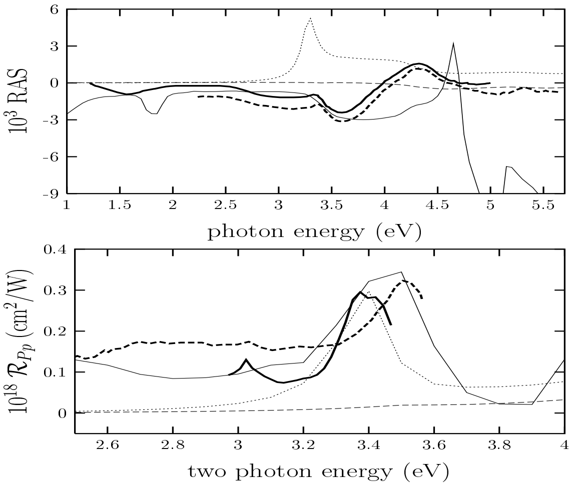

Figure 3.4: Top(bottom) panel shows the RAS (SHG) optical spectrum of Si(100) surface. The dashed line is for the ideal(1×1) surface (in SHG, ×5), the dotted line is for the strain-relaxed surface (in SHG, ×5), the thin solid line is for to the 2×1 reconstructed surface (in SHG, ×.5). Experimental spectra are also shown: for RAS, the thick solid line is that of R. Shioda and J. van der Weide [68] and the thick dashed line is that of Jaloviar *et al.* [90]; for SHG, the thick solid line is that of Dadap *et al.* [31] and the thick dashed line is that of Höfer [32].

the strain relaxed surface shows a positive anisotropy around 3.4 eV which is not seen in the experimental spectrum. The RAS spectrum for the 2×1 surface shows the low frequency experimental peak found at 1.6 eV but displaced in energy by 0.2 eV upward. This peak is usually assigned to a surface state [11], which in our theory results from the local field. The positive experimental structure at 4.3 eV is also qualitatively reproduced but displaced in energy by 0.4 eV.

On the other hand, it is seen in the SHG spectrum of Fig. 3.4 that both the strain-relaxed and the reconstructed 2×1 surfaces reproduces the experimental peak at 3.36 eV thus confirming the conclusion made by Daum *et al.* [29] that the bulk E_1 transition of Si yields a SHG resonance at the Si(100) clean or oxide covered surface due to the vertical strain induced by surface reconstruction. Notice that the SHG spectrum for the ideal 1×1 surface has no structure. For better correspondence with the experiment the SHG spectrum has been moved by 0.1 eV and 0.2 eV for the strain-relaxed and 2×1 reconstructed surface respectively.

Figure 3.5 shows the RAS and SHG spectra of the Si(100)2×1 surface for three surface reconstructions with different bucklings [81, 89], along with the experimental results of Refs. 68 and 90 performed on highly oriented single-domain surfaces for RAS and Refs.

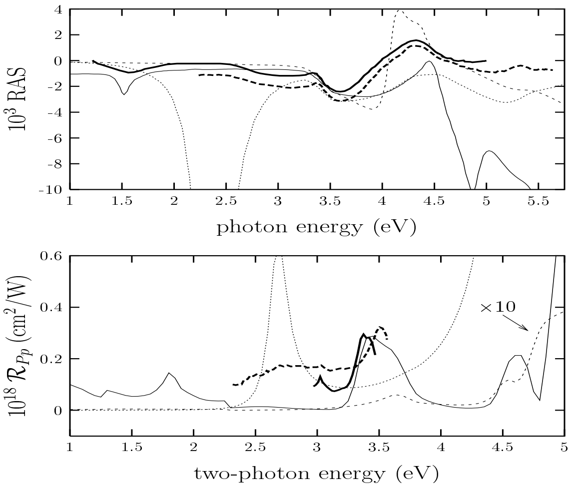

Figure 3.5: In the top and bottom panel the RAS and SHG spectra for p-in P-out polarizations of clean Si(100)2×1 are shown, for different dimer bucklings: 0 Å (symmetric dimers) (long dashed line), 0.6 Å (thin solid line) and 0.7 Å (dashed line). The thick solid and dashed lines correspond to the experimental spectra as in Fig. 3.4. It is mentioned that the vertical scale for SHG is within the same order of magnitude as the microscopic calculation of Ref. 45, and that the energy has been shifted upwards by 0.3 eV.

31 and 32 performed on double domain surfaces for SHG. All dipoles (including the dimers) are taken to have identical $\overset{\leftrightarrow}{\alpha}(\omega)$, with $f = 1$. For RAS we observe the following features. All theoretical spectra show three features above 3.5 eV, that are near the experimentally determined values of 3.6 eV, 4.3 eV and 5.3 eV. However, only the surface with a buckling of 0.7 Å gives the RAS features having correct signs at 3.9 eV and 4.2 eV, in qualitative agreement with the experimental results. The RAS spectrum for the surface with symmetric dimers shows a feature at 3.3 eV in correspondence with the experimental one at the same energy. However, this case also shows a broad and large negative structure at 2.4 eV not seen in the experimental curves. In addition, only the RAS spectrum of the geometry with buckling of 0.6 Å has a feature at 1.5 eV, which qualitatively reproduces the experimental one at 1.6 eV. Similar results are reported by Palummo *et al.* [11] at 1.5 eV and 4.3 eV, where the RAS spectra are obtained for the (2×1) surface through *ab initio* calculations within DFT-LDA using reconstructions with symmetric dimers, with bucklings of 0.56 Å and 0.71 Å. Fig. 3.6 shows their spectra, the low-energy peak, essentially due to dimer surface states, shifts from 1 to 1.4 eV due to an opening of the gaps and changes its sign, in going from the symmetric to the asymmetric case. The same peak increases in strength and shifts slightly to 1.6 eV with increase of the buckling. On the other hand, the positive structure at 4.3 eV reduces as the buckling increases. We mention that the RAS spectra calculated there and shown in

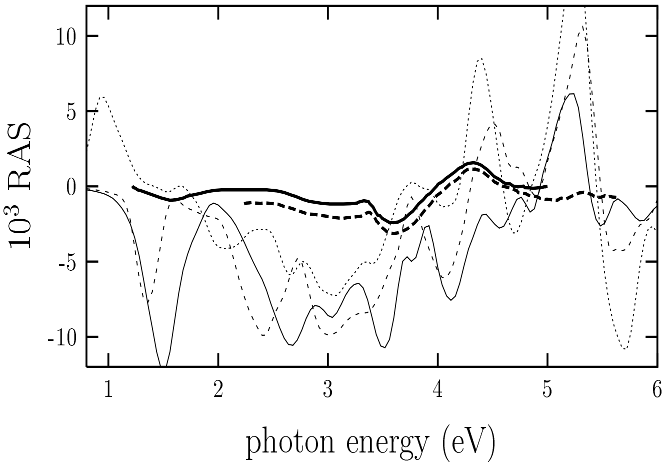

Figure 3.6: RAS spectra for the Si(100)2×1 surface as a function of dimer buckling of Ref. 11 calculated within the DFT-LDA. The dotted line is for the structure with symmetric dimers (buckling of 0 Å), the dashed line is for the structure with buckling of 0.56Å, and the thin solid line is for the structure with buckling of 0.71Å. The experimental spectra is shown for comparison as in Fig 3.4.

Fig. 3.6 have several features between 1.5 eV and 4.0 eV that are not present neither in the experimental data nor in our spectra. Even though the qualitative experimental behavior is reproduced with the *ab initio* calculations shown in 3.6, it is remarkable that the calculated spectra for RAS, within the polarizable bond model show a much better lineshape. In principle both calculations, within the polarizable bond model and within *ab initio* calculations of Ref. [11] reproduce qualitatively the features around 1.6 eV and 4.3 eV seen in the experiment. The best agreement of RAS with the experiment in both models is found to be for a surface with buckling of $\sim 0.6\,\AA$.

Moving to SHG we obtain the results of Figs. 3.5 and 3.7 where we have shifted the theoretical curves upward by 0.3 eV to provide better correspondence between calculated and measured structures. We see from Fig. 3.5 that for the surface with a buckling of 0.6 Å, the E_1 resonance seen experimentally at 3.4 eV (in the two-photon energy) is reproduced. At 4.6 eV there is another peak which corresponds to the bulk E_2 Si transition. Also, for this surface there is a peak at 1.8 eV. For the surface with a buckling of 0.7 Å the E_1 peak appears, but now it is now blueshifted in comparison with that of the previous surface, and the E_2 peak is seen as a small shoulder slightly redshifted with respect to the same previous surface. Furthermore, the intensity of its spectrum is an order of magnitude smaller than that of the surface with buckling of 0.6 Å. For the surface with zero buckling, we find that the E_1 peak is strongly redshifted to 2.7 eV, and

E_2 is also strongly blueshifted to 5 eV, which is not shown in the plot since it has a large intensity. The qualitative dependence of the SHG E_1 resonance on the buckling of the dimer is also seen in the microscopic model of Ref. 91 but the shifting of the E_1 peak is now downward in energy as the buckling increases.

Thus, our results may imply that if the local field is incorporated into a microscopic calculation, one should expect the SHG resonant peaks to shift. Finally we mention that neither case reproduces the surface peak at 3 eV seen in the experimental curve. This peak is obtained in the microscopic theory of Ref. 45 and is due to electronic surface states related to the dimer (see Chap. 4). Since we have treated the dipole corresponding to the dimer's bond in the same manner as (except for its orientation) a bulk bond, we should not expect to have a surface related transition.

In principle one should be able to chose an appropriate $\overset{\leftrightarrow}{\alpha}(\omega)$ for the dimer and surface bonds in order to reproduce the surface SHG peak at 3 eV. However, we would like to keep the number of adjustable parameters to a minimum, and instead try to look into the phenomenology that the present model allows in simple physical terms, and see its consequences in the RAS and SHG spectra. Therefore, in what follows we explore an interesting point related to the prediction of Chadi by which, in a tilted dimer, there is a charge transfer of $\sim e/3$ into the upper Si atom of each buckled dimer [83]. In order to include such a charge transfer in our model, we can adjust the following two variables: a) f for the dimer alone (see Eq. 3.33), since it is proportional to the dimer electronic charge density through the plasma frequency

$$\omega_p^2 = \frac{4\pi n_0 e^2}{m} \tag{3.37}$$

where n_0 is the electronic charge density, e is the electron charge and m is the electron mass; and b) the position of the point dipole that replaces the dimer's bond, from its nominal centered position $\Delta = 0$, to an off-centered position $\Delta \neq 0$, since the charge is redistributed in the same manner as its centroid.

We have done such an exploration for the surface with a buckling of 0.6 Å, and have found that the RAS and SHG spectra that better reproduce the experimental data are those with $f = 1.9$ and $\Delta = 0.25a$ towards the upper Si atom of the dimer, where a the dimer's bond length. Both values are consistent with the Chadi's prediction of charge transfer. A roughly estimate of the possible value of f is as follows: from Eq. (3.37) we see that the plasma frequency is proportional to the electronic charge as $\omega_p \approx n_0^{1/2}$, according

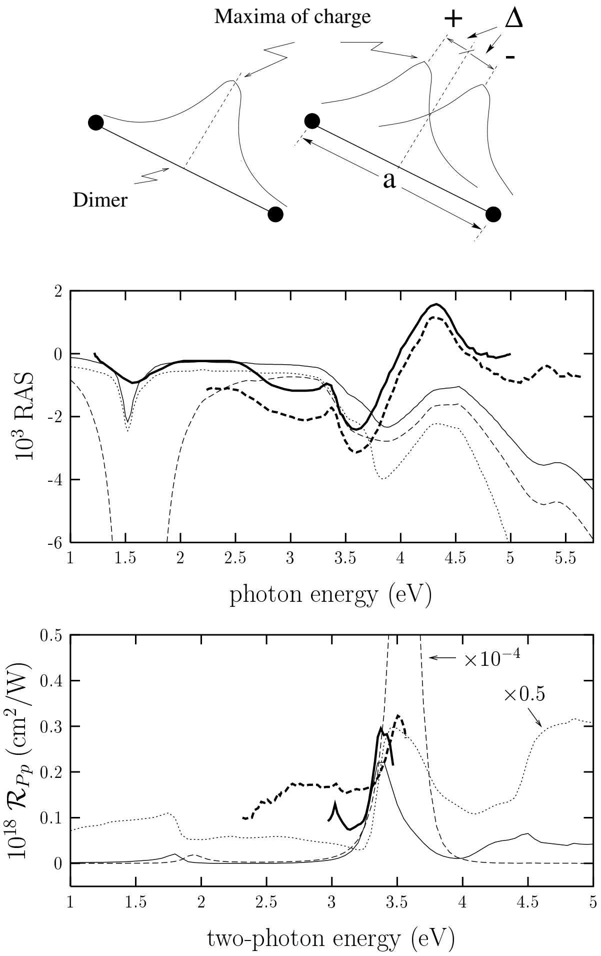

Figure 3.7: The top figure shows the dimer with a curve showing the distribution of charge. The plots are the same as Fig. 3.5, for a dimer buckling of 0.6 Å. The dashed line is for $\Delta = 0$, whereas the dotted line is for $\Delta = -0.25a$ and the solid line is for $\Delta = 0.25a$, which gives the dimer's dipole displaced towards the lower or upper Si by 0.25 of its length respectively. Both spectra have the same $f = 1.9$. The thick solid and dashed lines are the experimental spectra of Refs. 68 and 90 for RAS and Refs. 32 and 31 for SHG.

to Chadi prediction of charge transfer to the dimer, there should be a displacement of charge of 1/3 to the upper atom that forms the dimer, changing the effective charge at the dimer to 4/3 of its value of the bulk Si-Si bond. Besides, taking into account the union of two atoms, what in fact forms a dimer, we multiply by 2 the charge density. Thus, we have $n_0 \rightarrow [(2 \times 4/3)n_0]^{1/2} \approx 1.6 n_0^{1/2}$. On the other hand, the displacement of charge to the upper atom of the dimer makes the center of mass of the charge to be displaced upward by $1/6a$ towards the upper Si atom.

We show in Fig. 3.7 the RAS and SHG spectra for such values of f and Δ. Comparing the spectra, we see that $\Delta = .25a$ gives a much better lineshape than $\Delta = 0$ (whose spectrum is larger by a factor of 2), since the RAS feature at 1.5 eV and the SHG peak E_2 at 4.5 eV are very well defined. Also, the RAS spectrum qualitatively reproduces the small feature[‡] seen in the experiment of Ref. 90 above 5 eV. On the other hand, if we use a negative Δ which would imply an off-centered dipole towards the lower Si atom in the dimer (see top of Fig. 3.7), we obtain in the RAS spectrum a similar lineshape above 3 eV as the case for positive Δ, however the spectrum has a huge feature at 1.5 eV. Similarly, the SHG spectrum shows an enhanced E_1 peak. These features for negative Δ do not agree with the experimental results, thus confirming the prediction of Chadi through this optical model. [83].

To understand the origin of the structure shown in the above spectra, we proceed as follows. The solution of the total dipole moment that represents the polarization of the system has the following structure [92, 93]

$$p(n\omega) \sim \frac{S(n\omega)}{1 - \alpha(n\omega)M} \sim \mathcal{T}(n\omega)S(n\omega), \tag{3.38}$$

where $n = 1, 2$ refers to the linear or non-linear solution, respectively. We identify the local field $\mathcal{E}$ as $\mathcal{T}(n\omega) \sim (1-\alpha(n\omega)M)^{-1}$ and $S(\omega)$ as the linear source proportional to the external perturbing field. On the other hand, $S(2\omega)$ is the non-linear source proportional to $\mathcal{T}^2(\omega)$, with M representing the dipolar interaction tensor, and $\alpha(\omega)$ representing $\overset{\leftrightarrow}{\alpha}(\omega)$ (see. Eq. (3.2)). From Eq. (3.38), $p(\omega)$ could have structure only from the local field $\mathcal{T}$ at ω, since $S(\omega)$ has no structure. In contrast, $p(2\omega)$ could have structure at 2ω directly from $\mathcal{T}(2\omega)$, and also through $S(2\omega)$ which is driven by the local field $\mathcal{T}$ at ω. For instance, we have checked that in Fig. 3.7 the SHG peak at $2\hbar\omega = 1.8$ eV comes from the local field $\mathcal{T}$ at 2ω, and that the SHG E_1 peak comes from the local field $\mathcal{T}$ at

---

[‡] We do not add further comments in the qualitatively agreement on this feature since the errors bars of the experimental spectrum of Ref. [90] are roughly of the same magnitude.

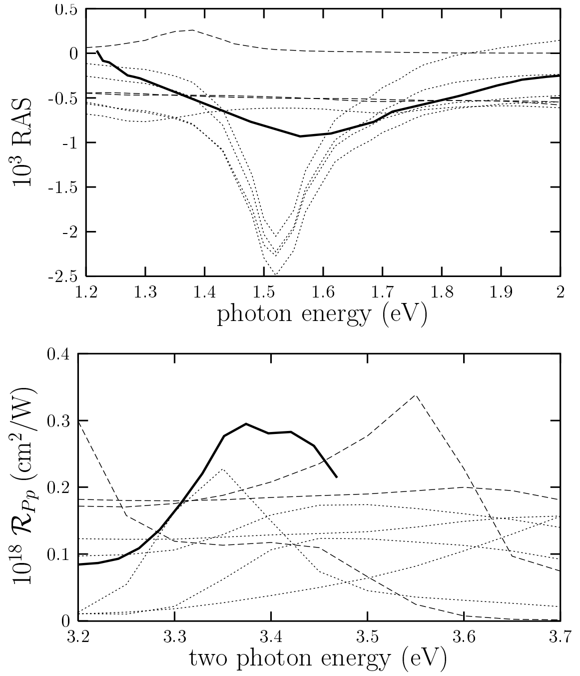

Figure 3.8: RAS and SHG spectra for the 2×1 reconstructed surface. The dotted(dashed) line is for the case when the interaction of the 1st, 2nd, 6th-8th (3rd through 5th) subsurface plane of bonds with the dimers is artificially set to zero. The thick solid lines are for the experimental data as in Fig. 3.5.

ω (through the non-linear source), just as the RAS feature at 1.5 eV also comes from the local field $\mathcal{T}$ at ω[§]

Within this model, we also can explore the localization of the dominant interaction of the dimer with the sub-surface bonds. In principle this exploration will give information on the origin of the features seen in the RAS and SHG spectra. This can be done by taking off (setting to zero) the interaction of the dimers with the sub-surface bonds. The results, for the RAS and SHG spectra, are shown in Fig. 3.8 where it is seen that 1.5 eV peak disappears in the RAS spectrum when the interaction of the 3rd through the 5th bond layers with the dimers is taken off. Similarly the E_1 peak in the SHG spectrum is not well defined. This behavior suggests that it is the interaction of these planes with the dimers which gives the anisotropy found at 1.6 eV and the E_1 resonance for SHG. These results show clearly how RAS and SHG are sensitive to the surface and sub-surface region reconstruction. Similar qualitative results will be found in the microscopic treatment of Chap. 4, in which the electronic transitions are between dimer and sub-surface electronic

---

[§] We mention that double resonances where $S(2\omega)$ and $\mathcal{E}(2\omega)$ resonate at the same frequency producing a huge enhancement of the SHG yield, could be found in other type of structures by adjusting the geometry of the system as shown in Ref. 92.

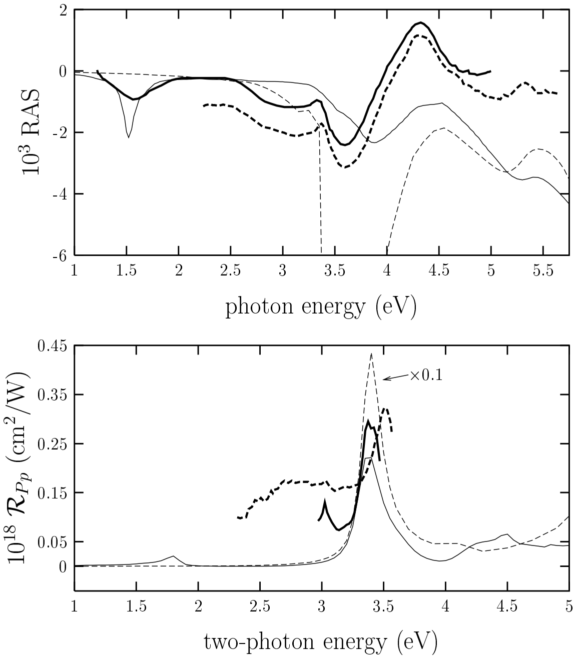

Figure 3.9: RAS and SHG spectra for the Si(100) surface with reconstruction 2×1(thin solid line) and c(4×2)(dotted line). The thick solid and dashed lines are for the experimental data as in Fig. 3.5.

states.

In order to compare with other reconstructions, we have calculated RAS and SHG for the most favorable reconstructed c(4×2) surface [83] at low temperatures using the same parameters as that of the 2×1 case (see Fig. 3.9). The RAS spectrum shows an enhanced anisotropy feature (negative) at 3.5 eV and a broad feature (also negative) at 4.4 eV, which do not reproduce the experimental spectra as good as the 2 × 1 structure shown also in Fig. 3.5. Although the RAS spectrum shows a qualitatively good agreement with experiment for energies above 5 eV, we do not add further comments, as before, in the qualitatively agreement on this feature since the errors bars of the experimental spectrum of Ref. [90] are roughly of the same magnitude. For SHG the E_1 is well reproduced, but it has a larger intensity than the 2×1 case. It also shows a very weak E_2 resonance. Neither the RAS nor the SHG give a peak at 1.5 eV, in contrast with the 2 × 1 for a buckling of 0.6 Å, and the surface peak at 3 eV for SHG is also not present. The SHG spectrum for the c(4×2) gives a good SHG E_1 resonance, however the RAS spectrum does not give good agreement with experiment. This might suggests that 2 × 1 reconstruction or a combination of both reconstructions of the experimental sample i.e the main features in the spectra might have its origin on the presence 2×1 and c(4×2) reconstructions of the sample.

We finally mention that for the ideally terminated (100) surface we find a finite RAS spectrum (see Fig. 3.4). On the other hand, the SHG spectrum has no E_1 peak, thus confirming the statement that the surface reconstruction gives rise to the observed nonlinear spectra.

3.9 Conclusions

In this chapter, we have described the model of polarizable bonds and then we have calculated, within this model, the surface RAS and SHG optical spectra of clean Si(100)2×1. We find that both RAS and SHG are sensitive to the buckling of the dimer and that, for a surface with dimer buckling of 0.6 Å, it qualitatively reproduces most of the experimental features reported in the literature. By changing parameters of the model, we conclude that the structures found in RAS and SHG are produced by the atomic reconstruction of the surface through the local field induced in the surface and sub-surface region. We calculated also RAS and SHG spectra for a c(4×2) surface reconstruction. The RAS spectrum does not show the the surface-related peak at 1.5 eV however, it shows a good qualitative agreement with experiment for energies above 5 eV. Whereas in the SHG spectrum, we found that the E_1 resonance is in well agreement with experiment. The surface sensitivity shown by this model is such that, as a further extension of this work, one can refine the dimer geometry by varying structural parameters and by choosing a few frequencies, like E_1 and E_2, at which to fit the spectral features of RAS and SHG. However, this is beyond the scope of the present thesis. Finally within the polarizable bond model, we see that the 2×1 reconstruction of Si(100) yields a better agreement with experiment than the c(4×2) structure in contrast with the conclusion of the microscopic calculations of Ref. [45]. To make a direct comparison with the above theoretical results, we suggest that the same sample should be studied in RAS and SHG spectroscopic experiments.

Chapter 4

Microscopic study of SHG from semiconductor surfaces

4.1 Introduction

We have studied in Chap. 3 the linear and non-linear optical response of the Si(100) surface through the polarizable bond model. Such a phenomenological model has allowed us to get a physical understanding of the origin of the optical response of this surface in a very simple way. We concluded that the reconstruction of the surface through the local field induced in the surface and sub-surface region was responsible for the structures seen in reflectance anisotropy spectroscopy (RAS) and second harmonic generation (SHG) spectra. Furthermore, we have explored, within this model, the prediction of Chadi [83] of charge transfer to the upper atom of the dimer at the surface. The overall good agreement with the experimental results that the polarizable bond model yields has been a step forward into the understanding of the physical properties of the Si(100) surface, but there are still too much to be done, since this classical and phenomenological model lacks of a complete description of the electronic transitions involved in the band structure.

The proper calculation of the second-order non-linear response must be on the basis of a quantum-mechanical microscopic theory from which the information of the origin of the SHG optical response of media could be obtained. The semi empirical tight-binding (SETB) theory allows to calculate the SHG including a realistic calculation of the band structure. Microscopic models to study the non-linear optical response, for simple metals, we find self consistent calculations employing the time dependent local density approximation (TDLDA) applied to the jellium model [52, 58–61]. Whereas, for semiconductor surfaces, we have the microscopic formalism [66] of Cini where he found closed expressions to calculate the SHG. Based on this formalism Reining et al. [42] calculated the SHG of the As-covered Si(111) surface. Later, Gravrilenko and Rebentrost showed that the SETB theory could give qualitatively correct predictions of the non-linear optical response of both reconstructed and unreconstructed clean semiconductor surfaces [43, 44]. Also, Mendoza *et al.* [45] have calculated the surface SHG from clean and H-covered Si(100). Their microscopic calculation showed that the bulk E_1 resonance occurs in surface SHG spectra through electronic transitions across surface-perturbed bulk states, that H adsorption modifies the SHG lineshape by reducing the E_1 resonance and suppressing the spectral structures due to transitions across surface states and that, contrary to what may be argued, the $\chi_{\perp\perp\perp}$ component of the second-order surface susceptibility does not dominate the SHG signal. Instead, they found that the $\chi_{\|\|\perp}$ component of the second-order surface susceptibility is mostly responsible for the observed features. Therefore, it is the inter-play of both in-plane and perpendicular components of $\overset{\leftrightarrow}{\chi}$ that gives rise to the SH response. In the following we use the same model and propose a method to systematically investigate the different contributions of the non-linear susceptibility to the observed peaks in SHG. Part of this work is reported in Ref. [94].

The approach consists in the separation and analysis of the different microscopic contributions to the non-linear susceptibility by which the radiated SHG is calculated. Similar analysis have been presented in Ref. 95 for bulk SHG from cubic semiconductors, and in Ref. 42 for surface SHG from H and As-terminated Si(111). However, both studies only analyzed the 1ω and 2ω transitions and did not attempt to go any deeper into the nature of their predicted resonances. With our approach we are able to determine the bulk or surface nature of the transitions, their 1ω or 2ω character, and their localization within the surface or bulk atoms, thus giving a complete description of the SHG spectrum.

We take as an example clean Si(100) with a c(4 × 2) reconstruction, which is the energetically most favorable structure at low temperatures [96], and use the same microscopic model as that of Ref. 45 to continue its study of SHG. This model uses the SETB approach with a sp^3s^* basis set.[*] The SETB method has also been fre-

---

[*] In the tight-binding (TB) method [97, 98] each atom is associated with a finite set of orbitals, or atomic basis states, each of which can be occupied by two electrons. To describe the bonding in silicon requires a minimal sp^3 basis consisting of one s orbital and three p orbitals for each atom [99]. Attempts to fit the conduction bands of semiconductors with a nearest-neighbor sp^3 basis have been failed. To overcome this deficiency Vogl *et al.* [100] included an excited s state, s^*, on each atom, giving an sp^3s^*

quently and successfully employed to study the linear optical properties of semiconductor surfaces [84, 102, 103]. In particular we mention that the linear optical results for the Si(100)2×1 surface reconstruction have been compared with *ab initio* methods by Palummo *et al.* [11]. They analyzed two optical probes, RAS and surface differential reflectivity (SDR). The conclusion of this work was that due to the omission of second-neighbor interactions in the SETB scheme, the RAS signal has the wrong sing for the low energy structures, but for the rest of the spectra there is a one to one correspondence between SETB and *ab initio* structures. On the other hand, the SDR spectrum being an average over two perpendicular polarizations depends less critically on the theoretical scheme used, and thus SETB and *ab initio* SDR agree rather well. Palumno *al.* [11] calculated RAS and SDR spectra for Si(100)c(4×2) surface confirming the aforementioned behavior. However, the *ab initio* spectra have some surface features at low energy not shown by the SETB calculation. A similar comparison between SETB and *ab initio* SHG calculations shows that for Si(100)c(4×2) the spectra basically agrees [47] above 2 eV in the two-photon energy (see inset of Fig. 4.3). These two methods will be used to study B and H-covered Si(100) surfaces in Chap. 5. The SETB approach has the advantage of being computationally less intensive. Within this approach we find that the clean Si(100) with a c(4×2) reconstruction has besides the 3 eV and E_1 SHG resonances already measured in Ref. 31 and theoretically reproduced in Ref. 45, a low energy surface resonant peak at $2\omega \sim 2.2$ eV which the recent spectrum obtained by Mantese *et al.* [104] in the infrared region, seems to corroborate. Thus, the analysis of the non-linear process that converts the incoming radiation into SH radiation through the non-linear susceptibility, will shed new information on the microscopic behavior of this surface.

The chapter is organized as follows: we describe, in Sec. 4.2, the procedure to calculate the SHG efficiency through the non-linear susceptibility tensor $\overset{\leftrightarrow}{\chi}$, and the decomposition of $\overset{\leftrightarrow}{\chi}$ into its different contributions. In Sec. 4.3, we show the spectra of the different $\overset{\leftrightarrow}{\chi}$ terms that contribute to SHG of a Si(100)c(4×2) surface, and analyze the resonances found at $2\omega \sim 2.2$, 3 eV and the bulk E_1. Finally in Sec. 4.4, we give conclusions.

---

basis. The inclusion of various excited states (including the *d* states [101]) would obtain the correct band structure.

4.2 Nature of the transitions through the non-linear susceptibility

A microscopic approach to the calculation of $\overleftrightarrow{\chi}$ was proposed by Cini [66] and adapted for a semiconductor surface by Reining *et al.* [42]. This method has the characteristic that within the same formalism one calculates the microscopic susceptibility and the radiated SH efficiency. We use a slab approach to mimic the semi-infinite system. The main steps taken to this end will be described. The key point is the calculation of the vector potential from which the non-linear radiated fields are calculated, and thus, the SHG yield is obtained through

$$R(\omega) = \frac{I(2\omega)}{I^2(\omega)}, \tag{4.1}$$

where the $I(\omega)$ is the intensity of the external field and $I(2\omega)$ is the intensity of the generated harmonic field given by

$$I(2\omega) = c|E(2\omega)|^2/8\pi. \tag{4.2}$$

The vector potential $\vec{A}(\vec{r},t)$ is given by [105]

$$A_i(\vec{r},t) = -\frac{1}{\hbar c}\int \mathrm{d}\vec{r}\,' \int_{-\infty}^{t} \mathrm{d}t' D^R_{ij}(\vec{r},t;\vec{r}\,',t')J_j(\vec{r}\,',t'), \tag{4.3}$$

where $\overleftrightarrow{D}^R$ is the retarded Green function appropriate for an interface [106], and $\vec{J}$ is the induced current. The interaction of the electron with the electromagnetic field is described through the perturbing potential given within the Coulomb gauge by

$$V = -\frac{e}{mc}\vec{A}\cdot\vec{p} + \frac{e^2}{2mc^2}\vec{A}^2 \tag{4.4}$$

where $\vec{A}$ is the external perturbing field at ω and $\vec{p}$ is the momentum operator of the electron. In the long wavelength approximation the term proportional to $\vec{A}^2$ does not give rise to electronic transitions, thus it can be eliminated [107]. Applying perturbation theory, the wave function to n-th order in V is given by

$$|\psi^{(n)}>= \frac{1}{(i\hbar)^n}\int_{-\infty}^{t} \mathrm{d}t' \int_{-\infty}^{t'} \mathrm{d}t'' \cdots V_I(t')V_I(t'') \cdots |\psi^{(0)}>, \tag{4.5}$$

where the subscript I means that V is in the interaction representation[†] and $\psi^{(0)}$ is the ground state wave function. To second-order, the induced current is given by

$$J_i =< \psi^{(0)}|\hat{J}_i|\psi^{(2)} > + < \psi^{(2)}|\hat{J}_i|\psi^{(0)} > + < \psi^{(1)}|\hat{J}_i|\psi^{(1)} >, \tag{4.6}$$

where $\hat{\vec{J}}$ is the quantum mechanical current operator [105]

$$\hat{\vec{J}} = \frac{e}{m}\hat{\vec{p}} - \frac{e^2}{mc}\vec{A}. \tag{4.7}$$

Substituting Eq. (4.6) and Eq. (4.5) into Eq. (4.3) and using $\vec{J} = \partial\vec{P}/\partial t$, where $P_i = \chi_{ijk}E_jE_k$ is the non-linear polarization, it is possible to obtain, within the long wavelength approximation, the imaginary part of the non-linear susceptibility as [45]

$$\begin{aligned}
\Im m(X_{ijk}(\omega)) \quad = \quad & \frac{\pi n_0 e^4}{2Am^3\omega^3}\sum_{\vec{k}}\sum_{r\in C}\sum_{s\in V} \\
& \left\{\sum_{n\in C}\left[\left(\frac{\mathcal{P}^i_{sn}P^j_{nr}P^k_{rs}}{E_{ns}-2E_{rs}} + \frac{P^j_{sn}\mathcal{P}^i_{nr}P^k_{rs}}{E_{ns}+E_{rs}}\right)\delta(E_{rs}-\hbar\omega)\right.\right. \\
& \left. -2\frac{\mathcal{P}^i_{sn}P^j_{nr}P^k_{rs}}{E_{ns}-2E_{rs}}\delta(E_{ns}-2\hbar\omega)\right] \\
& -\sum_{m\in V}\left[\left(\frac{\mathcal{P}^i_{mr}P^j_{sm}P^k_{rs}}{E_{rm}-2E_{rs}} + \frac{P^j_{mr}\mathcal{P}^i_{sm}P^k_{rs}}{E_{rm}+E_{rs}}\right)\delta(E_{rs}-\hbar\omega)\right. \\
& \left.\left. -2\frac{\mathcal{P}^i_{mr}P^j_{sm}P^k_{rs}}{E_{rm}-2E_{rs}}\delta(E_{rm}-2\hbar\omega)\right]\right\}
\end{aligned} \tag{4.8}$$

where we have used for the second-order susceptibility, X_{ijk} for a single domain surface and left the used of χ_{ijk} for a double domain surface (see below). $P^i_{sn}(\vec{k})$ is the matrix element of the i-Cartesian component of the momentum operator ($\hat{\vec{p}}$) between states

---

[†] In the *interaction representation* the time dependence of the system is partly transferred to the operators while the wavefunctions varies slowly. Let the hamiltonian be of the form $\hat{\mathcal{H}} = \hat{\mathcal{H}}_0 + \hat{V}(t)$, where $\hat{\mathcal{H}}_0$ is the hamiltonian of the time independent non-pertubed system and $\hat{V}(t)$ is the perturbation. If $\hat{L}$ is the operator of an arbitrary physical quantity and $\psi(t)$ the time dependent wave function, then in the interaction picture we have

$$\begin{aligned}
L_I &= \exp(\frac{i}{\hbar}\hat{\mathcal{H}}_0 t)\hat{L}\exp(-\frac{i}{\hbar}\hat{\mathcal{H}}_0 t), \\
\psi_I &= \exp(-\frac{i}{\hbar}\hat{\mathcal{H}}_0 t)\psi(t).
\end{aligned}$$

s and n, which may be valence (V), or conduction (C) states at point $\vec{k}$ in the two dimensional-Brillouin zone (2DBZ), A is the sample area,

$$E_{nr} = E_n(\vec{k}) - E_r(\vec{k}), \tag{4.9}$$

with $E_n(\vec{k})$ the one-electron energy. The emission of SH light is described by the modified momentum operator

$$\vec{\mathcal{P}} = \frac{S(z)\vec{P} + \vec{P}S(z)}{2}, \tag{4.10}$$

where $S(z)$ is a function of z, being 1 at the front surface and 0 at the back surface, which avoids the spurious destructive interference of SH light generated at the two surfaces of the slab. For $S(z)$ we have used a step function centered at the middle of the slab. Using smoother functions yields the same SHG lineshape with only small changes in the absolute magnitude of $\mathcal{R}(\omega)$. We remark that Eq. 4.8 must be symmetrized in the last two indices (jk) in order to comply with the intrinsic permutation symmetry of $\overset{\leftrightarrow}{\chi}$.

The fundamental electric field $\vec{E}(\omega)$ oscillating at ω, given by $\vec{E}(\omega) = i\omega/c\vec{A}(\omega)$, which induces the non-linear response, is taken inside the surface. In particular, this field is simply given by the external field properly multiplied by the corresponding Fresnel factors [42]. A more detailed description of the fields, which incorporates the spatial variation of the dielectric function near the surface within the three-layer model [42], shows no change in the SHG peaks positions, and only slight difference in their intensity. However the full treatment of the surface screening is still lacking, and further improvement of the present formulation can be made along this point. This screening will presumably affect more the zzz component of $\overset{\leftrightarrow}{\chi}$ than any other component, however is not at all trivial to anticipate what the actual effect will be, and thus we explain the results within the framework of our formalism. Also, at the present stage of the available calculations for non-linear optical properties of semiconductor surfaces, like the one presented here, local-field and excitonic effects are still beyond current capabilities and are thus neglected throughout. Again, these effects along with the surface screening will prove to be crucial for a quantitative comparison between theory and experiment.

The four different terms of Eq. (4.8) are written down according to 1ω and 2ω transitions corresponding to the $\delta(E - \hbar\omega)$ or $\delta(E - 2\hbar\omega)$ terms, respectively. The summations over states are written in such a way that the two external sums fix the transitions that conserve energy (i.e. sum over r and s states), leaving as the most internal summation the one over virtual states (i.e. sum over m states). Then,

$$
\begin{aligned}
\Im m(X^{1\omega,C}_{ijk}) &= \frac{\pi n_0 e^4}{2Am^3\omega^3}\times \qquad (4.11a)\\
&\sum_{\vec{k}}\sum_{r\in C}\sum_{s\in V}\sum_{m\in C}\left(\frac{\mathcal{P}^i_{sm}P^j_{mr}P^k_{rs}}{E_{ms}-2E_{rs}}+\frac{P^j_{sm}\mathcal{P}^i_{mr}P^k_{rs}}{E_{ms}+E_{rs}}\right)\delta(E_{rs}-\hbar\omega),
\end{aligned}
$$

$$
\Im m(X^{2\omega,C}_{ijk}) = \frac{\pi n_0 e^4}{2Am^3\omega^3}\sum_{\vec{k}}\sum_{r\in C}\sum_{s\in V}\sum_{m\in C}\frac{\mathcal{P}^i_{sr}P^j_{rm}P^k_{ms}}{2E_{ms}-E_{rs}}2\delta(E_{rs}-2\hbar\omega), \qquad (4.11b)
$$

$$
\begin{aligned}
\Im m(X^{1\omega,V}_{ijk}) &= -\frac{\pi n_0 e^4}{2Am^3\omega^3}\times \qquad (4.11c)\\
&\sum_{\vec{k}}\sum_{r\in C}\sum_{s\in V}\sum_{m\in V}\left(\frac{\mathcal{P}^i_{mr}P^j_{sm}P^k_{rs}}{E_{rm}-2E_{rs}}+\frac{P^j_{mr}\mathcal{P}^i_{sm}P^k_{rs}}{E_{rm}+E_{rs}}\right)\delta(E_{rs}-\hbar\omega),
\end{aligned}
$$

$$
\Im m(X^{2\omega,V}_{ijk}) = -\frac{\pi n_0 e^4}{2Am^3\omega^3}\sum_{\vec{k}}\sum_{r\in C}\sum_{s\in V}\sum_{m\in V}\frac{\mathcal{P}^i_{sr}P^j_{ms}P^k_{rm}}{2E_{rm}-E_{rs}}2\delta(E_{rs}-2\hbar\omega), \qquad (4.11d)
$$

where the superscripts refer to the type of ω-transition and C or V denote whether the virtual transition m is over a conduction or a valence state, respectively. Notice that if $E_{ms} = 2E_{rs}$ the apparent divergence of $\Im m\overset{\leftrightarrow}{X}^{1\omega,C}$ is canceled by that of $\Im m\overset{\leftrightarrow}{X}^{2\omega,C}$ for $2E_{ms} = E_{rs}$ due to the Dirac deltas of each term. A similar cancellation occurs between $\Im m\overset{\leftrightarrow}{X}^{1\omega,V}$ and $\Im m\overset{\leftrightarrow}{X}^{2\omega,V}$. Therefore this spurious divergences are avoided in the individual terms given above.

We remark that Eqs. (4.11) must be symmetrized in the last two indices (jk) in order to comply with the intrinsic permutation symmetry of $\overset{\leftrightarrow}{X}$ and we employ the Kramers-Kronig transform to calculate the real part of $\overset{\leftrightarrow}{X}$. Then, the components of $\overset{\leftrightarrow}{\chi}$ for the double-domain (100) surface are obtained through

$$
\chi_{\perp\perp\perp} = X_{zzz}, \qquad (4.12a)
$$

$$
\chi_{\perp\parallel\parallel} = (X_{zxx} + X_{zyy})/2, \qquad (4.12b)
$$

$$
\chi_{\parallel\parallel\perp} = (X_{xxz} + X_{yyz})/2, \qquad (4.12c)
$$

where $X_{ijk} = X_{ikj}$ are calculated for each of the two single-domain lattices.[‡] With the

---

[‡] Notice that $\chi^{I}_{zxx} = \chi^{II}_{zyy}$, and $\chi^{I}_{xxz} = \chi^{II}_{yyz}$, for domain I and domain II.

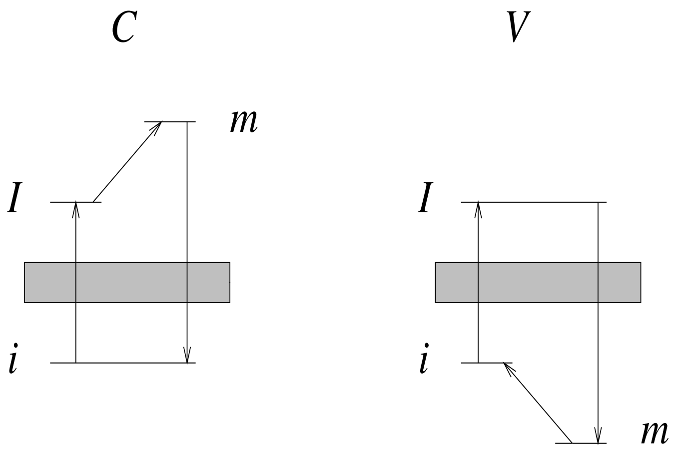

Figure 4.1: We sketch the two different transitions processes that contribute to SHG through Eq. (4.8). The shaded rectangle represents the energy gap. Here, i is the initial state always in the valence band, I is the intermediate state always in the conduction band, and m is the virtual state which could be in the conduction band (denoted by the C diagram and corresponding to Eqs. (4.11a) and (4.11b)) or in the valence band (denoted by the V diagram and corresponding to Eqs. (4.11c) and (4.11d)).

help of Eqs. (4.11) and Eqs. (4.12), it follows that

$$\overset{\leftrightarrow}{\chi} = \overset{\leftrightarrow}{\chi}^{1\omega,C} + \overset{\leftrightarrow}{\chi}^{2\omega,C} + \overset{\leftrightarrow}{\chi}^{1\omega,V} + \overset{\leftrightarrow}{\chi}^{2\omega,V}. \tag{4.13}$$

Figure 4.1 shows a sketch of the different transitions corresponding to each of the four terms of Eqs. (4.11). The transitions involved in the sums of these equations are classified according to their surface or bulk character. To this end, the weight $W^m_{\vec{k}}(N_i, N_f)$ is defined as the accumulated squared modulus of the wave function $\psi^m_{\vec{k}}$ between planes N_i and N_f. As before, $\vec{k}$ is the wave vector in the 2DBZ, and m denotes the corresponding states which could be V or C. Then,

$$W^m_{\vec{k}}(N_i, N_f) = \sum_{\ell=N_i}^{N_f} \sum_{\lambda} |\psi^m_{\vec{k}}(\ell, \lambda)|^2, \tag{4.14}$$

where $\ell = N_i$ denotes the starting plane and $\ell = N_f$ the final plane ($N_i \geq 1$, and $N_f \leq N$) and λ are the remaining quantum numbers of $\psi^m_{\vec{k}}$, like the ones required in the sp^3s^* basis, which also need to be summed. Now, several criteria can be used to classify m as a surface or as a bulk state. For instance, for a surface reconstruction localized to within the first N_s surface planes, if $W^m_{\vec{k}}(1, N_s) \geq W^m_{\vec{k}}(N_s + 1, N - N_s)$, then m is a surface state at $\vec{k}$, which means that the weight of the surface region is equal or larger than the weight of the bulk. Also, if $W_{\vec{k}}^m(1, N_s) \geq w$, for w some fixed positive value, then m is a surface state. For the case of an slab with a front surface different from the back surface, we can also consider $(W_{\vec{k}}^m(1, N_s) + W_{\vec{k}}^m(N - N_s, N))/2$ as the effective weight of the surface wave function, and use either of the two criteria just considered. If the state m is not a surface state, it must be a bulk state. In what follows we have found that the classification of surface and bulk states is basically the same using the first criteria or the second one with $w \sim 0.3$, which is a similar situation as the one used in the linear response described in Ref. 108.

From Fig. 4.1, the states that enter the summations in Eqs. (4.11), are either surface (s) or bulk (b), and thus each term in Eqs. (4.11) can further be classified according to the surface or bulk nature of their three different transitions. The following notation is defined:

$$\overset{\leftrightarrow}{\chi}^{1\omega,C}, \overset{\leftrightarrow}{\chi}^{2\omega,C}, \overset{\leftrightarrow}{\chi}^{1\omega,V}, \overset{\leftrightarrow}{\chi}^{2\omega,V} \leftarrow \overset{\leftrightarrow}{\chi}^{n\omega,v}(i, I, m), \tag{4.15}$$

where the argument denotes the surface (s) or bulk (b) character of the initial state i (always V), the intermediate state I (always C), and the virtual state m, which could be either $v = V$ or $v = C$. Also, $n = 1, 2$ refers to the type of ω transition. Considering all the possibilities in Eq. (4.15), 32 different cases are possible. To make this notation clear, we take any of the 32 possibilities as an example. For instance, $\chi^{2\omega,C}(s, b, s)$ involves a surface(s)-bulk(b) 2ω transition, whose virtual state is a surface (s) state in the conduction band (C). This term is calculated with Eq. (4.11b).

The analysis of the different contributions of $\overset{\leftrightarrow}{\chi}^{n\omega,v}(i, I, m)$ to the SHG yield is facilitated by further introducing auxiliary susceptibilities, which are defined as follows:

$$\overset{\leftrightarrow}{\chi}^{n\omega,v}(i, I) = \overset{\leftrightarrow}{\chi}^{n\omega,v}(i, I, s) + \overset{\leftrightarrow}{\chi}^{n\omega,v}(i, I, b), \tag{4.16a}$$

where it has been summed over the s and b character of the virtual states. Also,

$$\overset{\leftrightarrow}{\chi}^{n\omega}(i, I) = \overset{\leftrightarrow}{\chi}^{n\omega,V}(i, I) + \overset{\leftrightarrow}{\chi}^{n\omega,C}(i, I), \tag{4.16b}$$

where we have been summed over the V and C states of the virtual states regardless of their s or b character. Finally,

$$\overset{\leftrightarrow}{\chi}(i, I) = \overset{\leftrightarrow}{\chi}^{1\omega}(i, I) + \overset{\leftrightarrow}{\chi}^{2\omega}(i, I), \tag{4.16c}$$

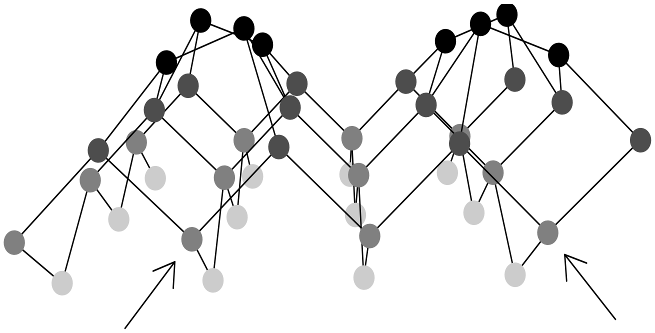

Figure 4.2: The c(4×2) reconstruction of the clean Si(100) surface is shown. The first layer of atoms corresponds to the alternating dimers (black circles), and the diminishing gray shaded circles to the 2nd, 3rd, etc layers. Notice the atoms just below the dimer rows in the 3rd layer (indicated by an arrow), which have an important role in the S_1 resonance.

where it has been summed over the 1ω and 2ω transitions. This last susceptibility is easily interpreted as the $i-I$ contribution to $\overset{\leftrightarrow}{\chi}$ of Eq. (4.13). We see that there are only four choices for the $i-I$ transitions, i.e. $s-s$, $s-b$, $b-s$ and $b-b$. Equivalent to Eq. (4.13), we have that

$$\overset{\leftrightarrow}{\chi} = \overset{\leftrightarrow}{\chi}(s,s) + \overset{\leftrightarrow}{\chi}(s,b) + \overset{\leftrightarrow}{\chi}(b,s) + \overset{\leftrightarrow}{\chi}(b,b). \tag{4.17}$$

As will be seen in the next section, with the help of Eq. (4.17) and Eqs. (4.16), we can analyze the contributions of the different type of transitions to the SHG radiated efficiency. We mention that $\overset{\leftrightarrow}{X}$ from Eq. (4.8), and thus, all the different χ's defined above, are dimensionless quantities. To obtain the non-linear susceptibility with the correct units, one must multiply them by $1/(n_0 e)$, which in turn could be written in $\mathrm{m}^2\mathrm{V}^{-1}$ or esu cm units.

4.3 Microscopic study of SHG

The equations shown in the previous section, allow us to study the nature of the different contributions to the non-linear susceptibility $\overset{\leftrightarrow}{\chi}$. As a very important example, we analyze the SHG efficiency for a clean Si(100) surface with a c(4×2) reconstruction, which is known to be the most stable configuration for low temperature [96]. This reconstruction is characterized by alternating buckled dimers as shown in Fig. 4.2 [109].

We follow the approach described in Ref. 45 for the calculation of $\overset{\leftrightarrow}{\chi}$ which uses the SETB method of Refs. 110 and 100.

The numerical accuracy of the method is basically controlled by the number of planes N and by the number of special k-points (N_k) for the summation over the 2DBZ that appears in Eqs. (4.8) and (4.11). The criterion for choosing N and N_k is a good numerical convergence of the SHG spectra with respect to them; in particular the results shown below are for $N = 16$ and for $N_k = 64$. Results for larger values of N and N_k give very similar results. In carrying out the Kramers-Kronig transform[§], a finite broadening of 25 meV was used; a larger (smaller) broadening will erase (sharpen) some of the small structures. With this broadening the comparison with experiment is quite good. Another test to corroborate the numerical consistency of the results could be made by verifying the following sum-rule of Ref. 111,

$$I = \int_0^\infty \mathrm{d}\omega \omega \Im m(X_{ijk}) = 0. \tag{4.18}$$

We obtain that for the different components of X_{ijk}, $0.07 < I < 0.50$ which is very reasonable for a function that has a large variation as a function of ω. We mention that we have shifted upward in energy the theoretical curves by 0.24 eV, in order to have a better correspondence in energy between the calculated and the measured E_1 structure. Differences of this order, often occurring in SETB calculations [112], are due to the underlying approximations involved in the method [45].

From Ref. 45, we also know that $\chi_{\|\|\perp}$ dominates the p-in P-out SHG spectrum. Although $\chi_{\perp\|\|}$ and $\chi_{\perp\perp\perp}$ have a magnitude similar to $\chi_{\|\|\perp}$, the prefactors of each component in Eq. (2.15) make $\chi_{\|\|\perp}$ the dominant contribution to the SHG radiation. Indeed, for the frequencies considered here (i.e. $\hbar\omega \sim 1 - 1.7\,\mathrm{eV}$), the wave vector perpendicular to the surface $k_\perp(2\omega)$ is much larger than $\sin\theta$ and $k_\perp(\omega)$, since it goes through a local maximum due to the fact that $\epsilon(2\omega)$ also goes through its first relative maximum around $2\hbar\omega \sim 3.3\,\mathrm{eV}$, which is the well known E_1 bulk transition of Si. We mention that this argument may break down for other energy regions (see below and Fig. 4.3). It is inter-

---

[§] The Kramers-Kronig relations follow directly from the causality principle and have played a fundamental role in the study of nonlinear response of media. Scandolo and Bassani [111] obtained the general asymptotic behavior of the second-order susceptibility. From this, three sets of Kramers-Kronig dispersion relations were obtained, and in turn seven sum rules were found. They can be of great help in analyzing available experiments, to connect the phase and amplitude of the susceptibility, and to establish if other contributions exist outside a given frequency range. They are also helpful in assessing the validity of computational calculations.

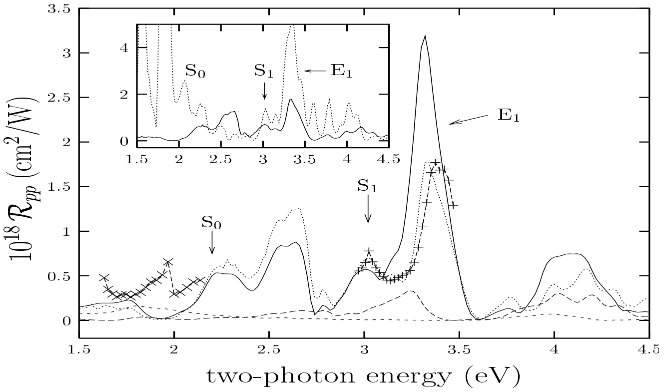

Figure 4.3: We show $\mathcal{R}_{Pp}$ for Si(100) for an incident angle of 55°. The dotted line is for the calculation using all components of $\overset{\leftrightarrow}{\chi}$ through Eq. (2.15a), whereas in the solid line only the dominant component $\chi_{\parallel\parallel\perp}$ is included. Notice the resemblance of both spectra, specially for the surface resonances S$_0$ and S$_1$, and the bulk resonance E$_1$. The long-dashed (short-dashed) line is for the case where only $\chi_{\perp\parallel\parallel}$ ($\chi_{\perp\perp\perp}$) is included. The $\chi_{\perp\perp\perp}$ case is multiplied by 20. The experimental data from Ref. 31 (pluses) and Ref. 104 (crosses) are shown with a dashed line (both sets of data are rescaled in the vertical axis). The inset shows the comparison between our SETB (solid line) and the *ab initio* [47] (dotted-line) results using all components of $\overset{\leftrightarrow}{\chi}$. The theoretical data have been shifted upward in energy by 0.24 eV (see text for details).

esting to notice that the calculation of Ref. 113, for the SHG spectra of Si(111)H (1×1) surface give that both $\chi_{\perp\parallel\parallel}$ and $\chi_{\parallel\parallel\perp}$, dominate the spectra regardless of the SETB or *ab initio* approach used in the calculation of the one-electron energies and momentum matrix elements required in Eq. (4.8).

The fact that $\chi_{\parallel\parallel\perp}$ dominates the SHG spectrum brings about a considerable simplification in the analysis. To wit, we only have to consider the different contributions to $\chi_{\parallel\parallel\perp}$, and relate these directly to $\mathcal{R}_{Pp}$. This situation is similar to the linear optical response of cubic materials, where the observed spectra could be directly related to only one scalar response function, which is the linear susceptibility [102,108,112]. Nonetheless, we mention that for SHG it is still necessary to take the absolute value of the complex r_{Pp} (Eq. (2.15)), so in general one has to proceed with care, since neither its real nor its imaginary part are directly proportional to $\mathcal{R}$. In Fig. 4.3, we show $\mathcal{R}_{Pp}$ calculated only through $\chi_{\parallel\parallel\perp}$, and the full calculation including all the terms in r_{Pp} of Eq. (2.15a). It is seen that both calculations are remarkably similar, specially below the E$_1$ SHG resonance. Also, in this figure we have included $\mathcal{R}_{Pp}$ for the case where only $\chi_{\perp\parallel\parallel}$ or $\chi_{\perp\perp\perp}$ are present. The former spectrum is comparable with the full calculation and the $\chi_{\parallel\parallel\perp}$ case for energies above 4 eV, but for energies around or below E$_1$ the spectra is at least an order of magnitude smaller. The spectrum for the $\chi_{\perp\perp\perp}$ component is negligible,

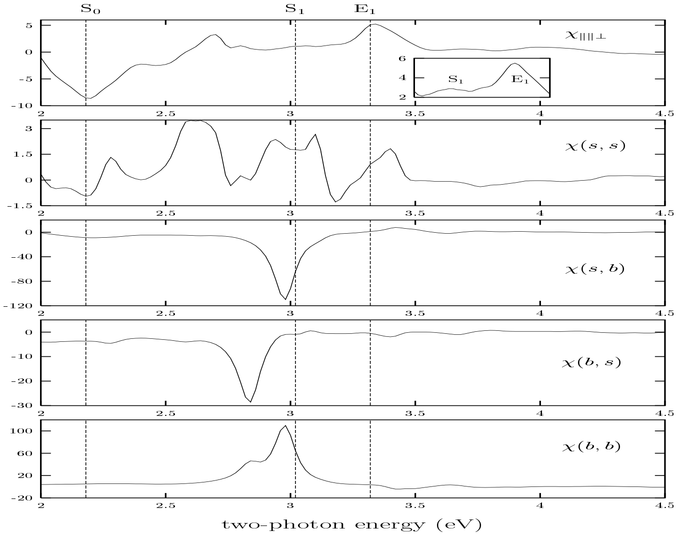

Figure 4.4: The imaginary part of $\chi_{\|\|\perp}$ and its respective $\chi(s,s)$, $\chi(s,b)$, $\chi(b,s)$, and $\chi(b,b)$ components from Eq. (4.17) vs. the two-photon energy are shown. The positions of the surface resonances S$_0$ and S$_1$, and the bulk resonance E$_1$ are denoted for reference. In the inset we show the absolute value of $\chi_{\|\|\perp}$ in order to enhance the S$_1$ peak. Notice the different scales in the vertical axis, where the units of χ are in 10^{-19} m^{2}V^{-1}.

thus it has been multiplied by 20 in order to show some structure in the figure. The experimental data from Dadap *et al.* [31] and from the recent experiment of Mantese *et al.* [104] are also shown for comparison. In the theoretical spectra, for the full calculation and for the $\chi_{\|\|\perp}$ component, we see the bulk E$_1$ resonance of Si at 3.32 eV and two surface peaks at 2.18 eV (onset) and 3.02 eV, that we called S$_0$ and S$_1$, respectively. We directly identify E$_1$ and S$_1$ with the experimental results of Ref. 31, and we can assign the resonance at 1.97 eV of Ref. 104 with S$_0$. It is worth mentioning that both sets of experimental data agree remarkably well with the theoretical spectra. From Fig. 4.3, it should be clear that the information contained in $\chi_{\|\|\perp}$ is practically the same as that of $\mathcal{R}_{Pp}$ for this energy range.

In the inset of Fig. 4.3 we compare our SETB SHG spectrum with that of the *ab initio* calculation of Ref. 47. We notice that E$_1$ and S$_1$ are very well given by both approaches, and S$_0$ appears at 2 eV for the *ab initio* spectrum instead of 2.18 eV of the SETB spectrum. The overall intensity is larger for the *ab initio* spectrum and the peaks above E$_1$ and between S$_0$ and S$_1$ are also shifted. As was mentioned above, both approaches differ below 2 eV. Thus, it should be clear that our SETB $sp^3s^\star$ model is reliable in the two-photon energy range from 2 eV up to 4.5 eV.

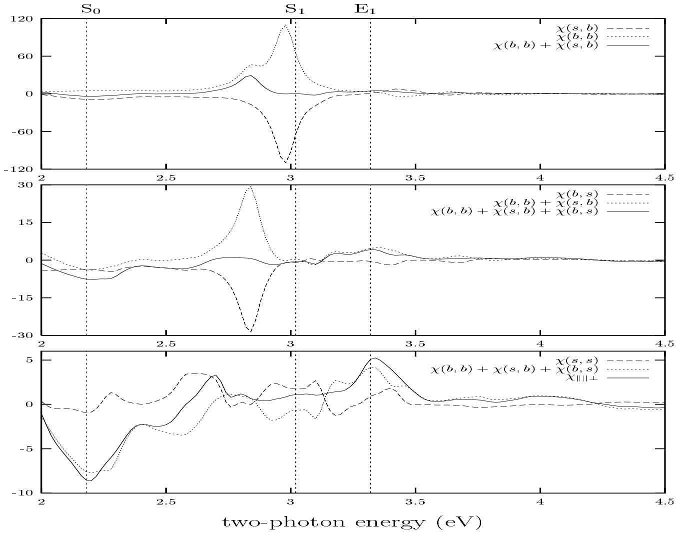

Figure 4.5: We show the same components of Fig. 4.4 and their partial sums. The top panel shows $\chi(s,b)$ (dashed line), $\chi(b,b)$ (dotted line) and their sum (solid line). The middle panel shows $\chi(s,b)+\chi(b,b)$ (dotted line), $\chi(b,s)$ (dashed line) and their sum (solid line). The bottom panel shows $\chi(s,b)+\chi(b,b)+\chi(b,s)$ (dotted line), $\chi(s,s)$ (dashed line) and their sum (solid line), which is equal to $\chi_{\|\|\perp}$ shown in the curve of the top panel of Fig. 4.4.

Since only one component of $\overset{\leftrightarrow}{\chi}$ dominates the spectrum, we drop the corresponding subscript $\|\|\perp$ from Eq. (4.16) and Eq. (4.17) to make the notation easier. Also, we show only the imaginary part of these components; similar information can be obtained by using the real part or the absolute value. The units of χ are given in $10^{-19}\,\mathrm{m}^2\ \mathrm{V}^{-1}$, and the reported values are within the experimental ones reported in Ref. 21 for similar surfaces.

Before we analyze some of the individual transitions seen in Fig. 4.3 the overall behavior of the susceptibility spectra will be described . Figure 4.4 shows $\chi_{\|\|\perp}$, along with its different contributions $\chi(s,s)$, $\chi(s,b)$, $\chi(b,s)$, and $\chi(b,b)$. Notice that neither component resembles the total susceptibility, although some particular features could be ascribed to a single component. As given by Eq. (4.17), the sum of the four different contributions should give the total result. To see how this is accomplished, Fig. 4.5 shows the next sequence of sums. In the top panel $\chi(s,b)$, $\chi(b,b)$ and their sum are shown. We clearly notice how the addition of these two terms cancels the large resonance just below 3 eV, giving among other peaks a large one around 2.8 eV. In the middle panel, $\chi(s,b)+\chi(b,b)$ is repeated and $\chi(b,s)$ is shown, along with the sum $\chi(s,b)+\chi(b,b)+\chi(b,s)$. Again, adding these terms makes the peak at 2.8 eV to be strongly quenched. Finally, in the bottom panel $\chi(s,b)+\chi(b,b)+\chi(b,s)$, $\chi(s,s)$, and $\chi_{\|\|\perp}$ are shown, where the fine

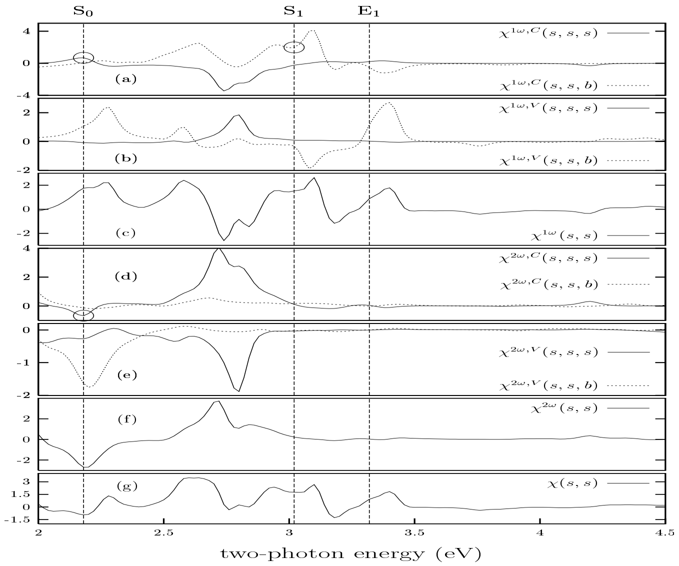

Figure 4.6: As in Fig. 4.4, the following components are shown: a) $\chi^{1\omega,C}(s,s,s)$ (solid line), $\chi^{1\omega,C}(s,s,b)$ (dotted line); b) $\chi^{1\omega,V}(s,s,s)$ (solid line), $\chi^{1\omega,V}(s,s,b)$ (dotted line); c) $\chi^{1\omega}(s,s)$ which is the sum of the last four; d) $\chi^{2\omega,C}(s,s,s)$ (solid line), $\chi^{2\omega,C}(s,s,b)$ (dotted line); e) $\chi^{2\omega,V}(s,s,s)$ (solid line), $\chi^{2\omega,V}(s,s,b)$ (dotted line); f) $\chi^{2\omega}(s,s)$ which is the sum of the last four; g) $\chi(s,s)$, which is the sum of c) and f). The main contributions to S$_0$ and S$_1$ are aim at with a circle.

additive properties of the susceptibility are even more apparent.

Figures 4.6-4.9 show the different terms of Eq. (4.16), which include the 32 different components of $\chi^{n\omega,v}(i,I,s)$, from where we can see how the different auxiliary susceptibilities combine to eventually give the total susceptibility χ of Eq. (4.17). The subtleties that give the final features in χ, which then gives the SHG resonant peaks, require a more careful and detailed analysis, which we proceed to give.

We are interested in analyzing the three resonances that have been measured and are shown in Fig. 4.3. The other resonances are also interesting, and can be analyzed along the lines that will follow. We discuss S$_0$, S$_1$ and E$_1$ in ascending energy order in the energy-space domain and $\vec{k}$-space domain.

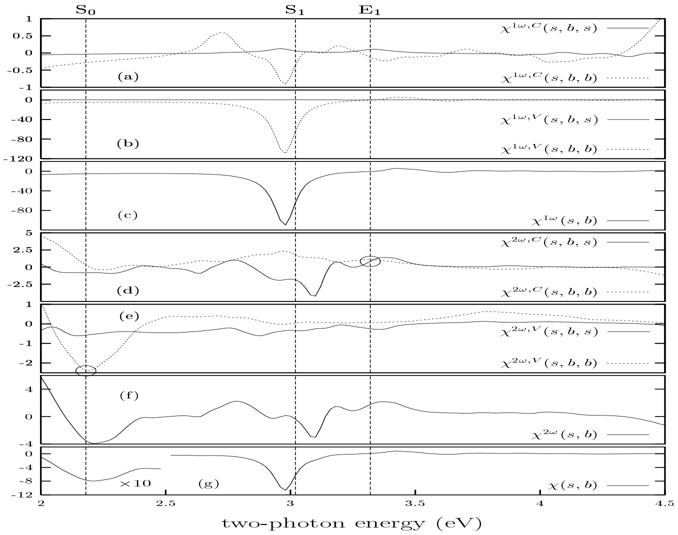

Figure 4.7: As in Fig. 4.4, the following components are shown: a) $\chi^{1\omega,C}(s,b,s)$ (solid line), $\chi^{1\omega,C}(s,b,b)$ (dotted line); b) $\chi^{1\omega,V}(s,b,s)$ (solid line), $\chi^{1\omega,V}(s,b,b)$ (dotted line); c) $\chi^{1\omega}(s,b)$ which is the sum of the last four; d) $\chi^{2\omega,C}(s,b,s)$ (solid line), $\chi^{2\omega,C}(s,b,b)$ (dotted line); e) $\chi^{2\omega,V}(s,b,s)$ (solid line), $\chi^{2\omega,V}(s,b,b)$ (dotted line); f) $\chi^{2\omega}(s,b)$ which is the sum of the last four; g) $\chi(b,s)$, which is the sum of c) and f), and it is multiplied by 10 below 2.5 eV in order to show S$_0$. The circles show the components that contribute to S$_0$ and E$_1$.

4.3.1 Energy-space domain

S$_0$ resonance

Figure 4.10 shows $\chi_{\parallel\parallel\perp}$, $\chi(s,s)$, $\chi(s,b)$, $\chi(b,s)$, and $\chi(b,b)$ from Fig. 4.5, but in a reduced two-photon energy range. It is seen how $\chi(s,b)$ and $\chi(b,b)$ show no features around S$_0$. However, $\chi(s,b)$ shows a broad dip around S$_0$ that when it is combined with the sharp minimum of $\chi(s,s)$, gives the well defined S$_0$ dip in the total susceptibility. Thus, it might be concluded that S$_0$ comes mainly from surface-surface and surface-bulk transitions. But now, with the help of Eq. (4.15) and Figs. 4.6-4.9, we can further investigate from which components of $\chi(s,s)$ and $\chi(s,b)$ this transition is coming from. From Fig. 4.6(a,d) and Fig. 4.7e is clear to see that only $\chi^{1\omega,C}(s,s,s)$, $\chi^{2\omega,C}(s,s,s)$ and $\chi^{2\omega,V}(s,b,b)$ contribute to S$_0$. The first two add in such a way that the maximum of the first partially cancels the minimum of the second, giving the dip at S$_0$ seen in $\chi(s,s)$ of Fig. 4.10. The $\chi^{2\omega,V}(s,b,b)$ component is also responsible for S$_0$, however we see that the influence of the other terms that contribute to $\chi^{2\omega}(s,b)$ make the minimum in $\chi(s,b)$ to be broader and slightly blueshifted from the value of S$_0$. It is mentioned that S$_0$ has a combination of both diagrams of Fig. 4.1, which means that it involves transitions to

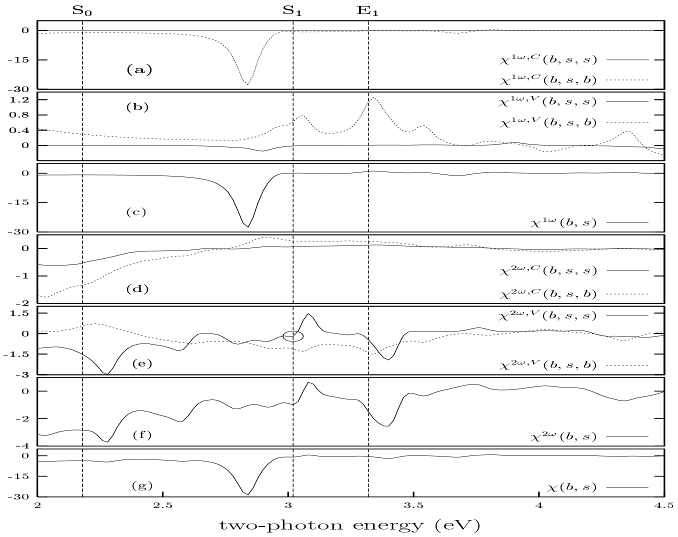

Figure 4.8: As in Fig. 4.4, the following components are shown: a) $\chi^{1\omega,C}(b,s,s)$ (solid line), $\chi^{1\omega,C}(b,s,b)$ (dotted line); b) $\chi^{1\omega,V}(b,s,s)$ (solid line), $\chi^{1\omega,V}(b,s,b)$ (dotted line); c) $\chi^{1\omega}(b,s)$ which is the sum of the last four; d) $\chi^{2\omega,C}(b,s,s)$ (solid line), $\chi^{2\omega,C}(b,s,b)$ (dotted line); e) $\chi^{2\omega,V}(b,s,s)$ (solid line), $\chi^{2\omega,V}(b,s,b)$ (dotted line); f) $\chi^{2\omega}(b,s)$ which is the sum of the last four; g) $\chi(b,s)$, which is the sum of c) and f). The circle shows the components that contribute to S$_1$

virtual conduction and to virtual valence band states.

S$_1$ resonance

From Fig. 4.5 we conclude that the main contributions to S$_1$ come from $\chi(s,s)$ and $\chi(b,s)$, and that neither $\chi(s,b)$ nor $\chi(b,b)$ contribute to S$_1$. However they do contribute along with $\chi(b,s)$ to the dips on both sides of S$_1$ that are seen in the bottom panel of Fig. 4.5. We also see how these two dips are almost canceled by the two corresponding peaks of $\chi(s,s)$, and that S$_1$ in the total susceptibility $\chi_{\|\|\perp}$ results from the dominant contribution of $\chi(s,s)$ over $\chi(b,s)$. As for S$_0$ we now look into $\chi^{n\omega,v}(i,I,m)$, for all combinations of $n=1,2$, $v=C,V$ and $i,I,m=s,b$, to find out the components responsible for S$_1$. It is found that $\chi^{1\omega,C}(s,s,b)$ and $\chi^{2\omega,V}(b,s,s)$ are responsible for S$_1$, as can be seen from Figs. 4.6a and 4.8e respectively. As for S$_0$, S$_1$ involves virtual transitions to the conduction and to the valence band states.

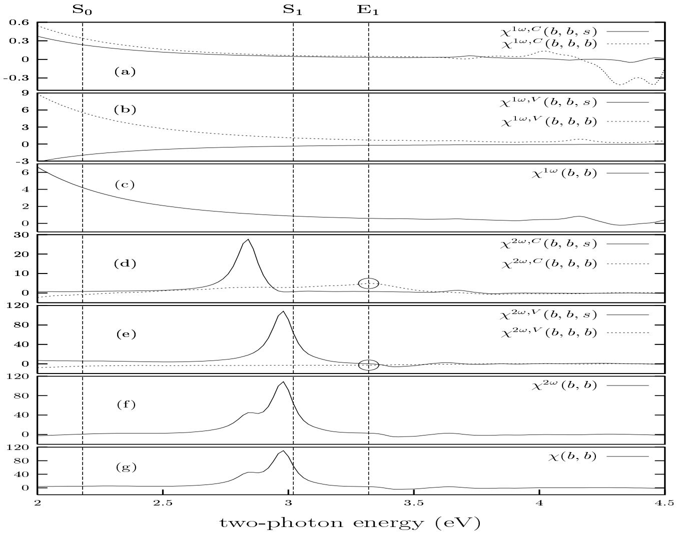

Figure 4.9: As in Fig. 4.4, the following components are shown: a) $\chi^{1\omega,C}(b,b,s)$ (solid line), $\chi^{1\omega,C}(b,b,b)$ (dotted line); b) $\chi^{1\omega,V}(b,b,s)$ (solid line), $\chi^{1\omega,V}(b,b,b)$ (dotted line); c) $\chi^{1\omega}(b,b)$ which is the sum of the last four; d) $\chi^{2\omega,C}(b,b,s)$ (solid line), $\chi^{2\omega,C}(b,b,b)$ (dotted line); e) $\chi^{2\omega,V}(b,b,s)$ (solid line), $\chi^{2\omega,V}(b,b,b)$ (dotted line); f) $\chi^{2\omega}(b,b)$ which is the sum of the last four; g) $\chi(b,b)$, which is the sum of c) and f). The circles show the components that contribute to E$_1$, for $\chi^{2\omega,V}(b,b,b)$ see Fig. 4.11.

E$_1$ resonance

Figure 4.11 shows a detail of $\chi^{2\omega,C}(s,b,s)$, $\chi^{2\omega,C}(s,b,b)$, $\chi^{2\omega,C}(b,b,b)$, and $\chi^{2\omega,V}(b,b,b)$, along with $\mathcal{R}_{Pp}$ (including only $\chi_{\|\|\perp}$) for reference. These are the components that dominate E$_1$, all other combinations of $\chi^{n\omega,v}(i,I,m)$ are only monotonic functions in the two-photon energy range shown. In contrast with S$_0$ and S$_1$, the real part of $\chi^{2\omega,C}(s,b,s)$ is the one that shows the structure which is partially responsible for E$_1$. For the other components the imaginary part is enough to correlate their partial contribution to E$_1$. Therefore, E$_1$ is given by the addition of these four contributions to $\chi_{\|\|\perp}$. We see how this bulk transition is influenced by the surface through $\chi^{2\omega,C}(s,b,s)$ and $\chi^{2\omega,C}(s,b,b)$ which involve transitions of surface states. Also, in Fig. 4.11 the extremes or inflection point of the four different contributions are shown with arrows, to remark a very interesting result, i.e. $\chi^{2\omega,C}(b,b,b)$ and $\chi^{2\omega,V}(b,b,b)$ have their extremes at higher energies than $\chi^{2\omega,C}(s,b,b)$, and this in turn has its extreme at an energy higher than $\chi^{2\omega,C}(s,b,s)$. Therefore E$_1$ is shifted from its bulk position by the delicate balance of purely bulk terms and surface-bulk terms of the non-linear susceptibility.

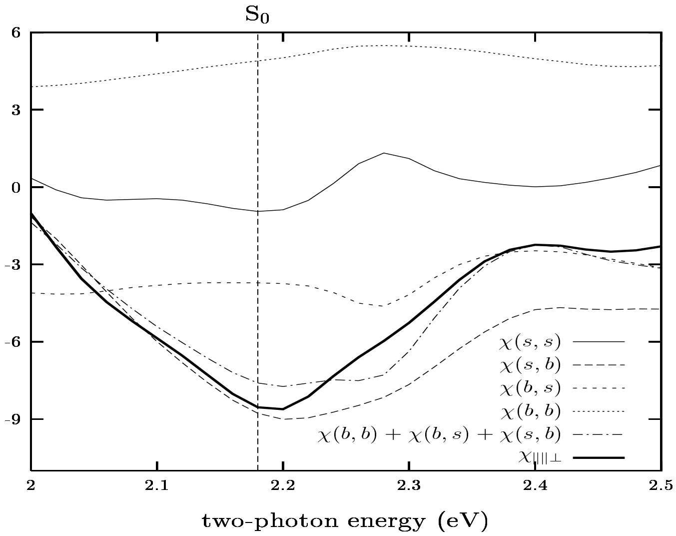

Figure 4.10: Detail of Fig. 4.4 for S_0, where we show $\chi(s,s)$ (thin solid line), $\chi(s,b)$ (long-dashed line), $\chi(b,s)$ (short-dashed line), $\chi(b,b)$ (dotted line), $\chi(s,b)+\chi(b,s)+\chi(b,b)$ (dash-dotted line), and the total sum $\chi_{\|\|\perp}$ (thick solid line). Notice that the S_0 dip in $\chi_{\|\|\perp}$ is given by the $\chi(s,s)$ and $\chi(s,b)$ term.

4.3.2 $\vec{k}$-space domain

Now that the origin of S_0, S_1 and E_1 in the energy-space domain (through the help of $\chi^{n\omega,v}(i,I,m)$) have been discussed, we can go back to Eqs. (4.11), and find out the $\vec{k}$-space domain information concerning these transitions. The way to do it is as follows. For a given $\vec{k}$, the energy in Dirac's deltas appearing in Eqs. (4.11) is fixed, to any of the values corresponding to S_0, S_1 or E_1. This automatically selects the transitions from the valence to the conduction state (second and third sums in Eqs. (4.11)). Then, it is possible to calculate the value of each summand as we add the most internal state m, which corresponds to the virtual valence or to the virtual conduction (m) states of Fig. 4.1. This way, we can find out the transitions to virtual states that contribute to a particular $\chi^{n\omega,v}(i,I,m)$ for any given resonance in the SHG spectrum, like S_0, S_1 or E_1. Even more, from Eqs. (4.11) we can even know if the resonance is coming from the energy denominators or the momentum matrix elements. This analysis is carried out for every $\vec{k}$ point in the 2DBZ, and thus the values of $\vec{k}$ which contribute more to Eqs. (4.11) can also be obtained. It would be convenient to do the $\vec{k}$-space analysis along the lines of maximum symmetry in the 2DBZ. However, the $\vec{k}$ points that dominate along these lines do not coincide with the actual $\vec{k}$ points used in the sum over the 2DBZ, and thus are not representative of $\chi^{n\omega,v}(i,I,m)$. However for completeness, we show in Fig. 4.12

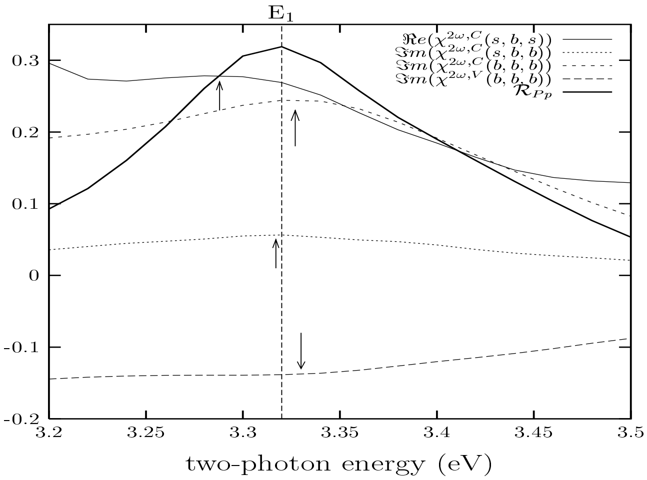

Figure 4.11: The following components for E$_1$ are shown: $\Re e(\chi^{2\omega,C}(s,b,s))$ (thin solid line), $\Im m(\chi^{2\omega,C}(s,b,b))$ (dotted line), $\Im m(\chi^{2\omega,C}(b,b,b))$ (short-dashed line), and $\Im m(\chi^{2\omega,V}(b,b,b))$ (long-dashed line). For reference $\mathcal{R}_{Pp}$ (thick solid line) is shown rescaled on the vertical axis. The up arrows denote the maxima and the down arrow the inflection point of the components of χ that contribute to E$_1$. Notice that the surface (bulk) related χ's have their E$_1$ redshifted (blueshifted) with respect to $\mathcal{R}_{Pp}$ E$_1$ (see text).

the energy bands along lines of maximum symmetry. We see surface states in the gap of the bulk states, along with surface states which are intermixed with bulk states (resonant states). In what follows, we show the results over the actual values of the $\vec{k}$ points used in the sum over the 2DBZ. These $\vec{k}$ points are represented in the inset of Fig. 4.12. We mention again that 64 $\vec{k}$-points are enough to get good convergence of the results. As in the previous subsection 4.3.1, we proceed to explain S$_0$, S$_1$ and E$_1$.

S$_0$ resonance

Figure 4.13 shows the energy bands along with the corresponding 1ω and 2ω transitions, as a function of the $\vec{k}$ points given in the inset of Fig. 4.12. Notice that the ordinates are given in natural numbers κ corresponding to the (k_x, k_y) pair in the 2DBZ. Notice that since $\hbar\omega$ of S$_0$ is too low there are only two 1ω transitions. Actually for lower resonances only the 2ω terms would contribute. Figure 4.13 also shows the summands of Eq. (4.11a) for the 1ω transitions, of Eq. (4.11b) and of Eq. (4.11d) for the 2ω transitions, which add up to $\chi^{1\omega,C}(s,s,s)$, $\chi^{2\omega,C}(s,s,s)$, and $\chi^{2\omega,V}(s,b,b)$ respectively, for the energy corresponding to S$_0$. These summands have been separated into the xxz and yyz Cartesian components of $\overset{\leftrightarrow}{X}$, needed in Eq. (4.12c) for $\overset{\leftrightarrow}{\chi}$. We recall that an ijk Cartesian

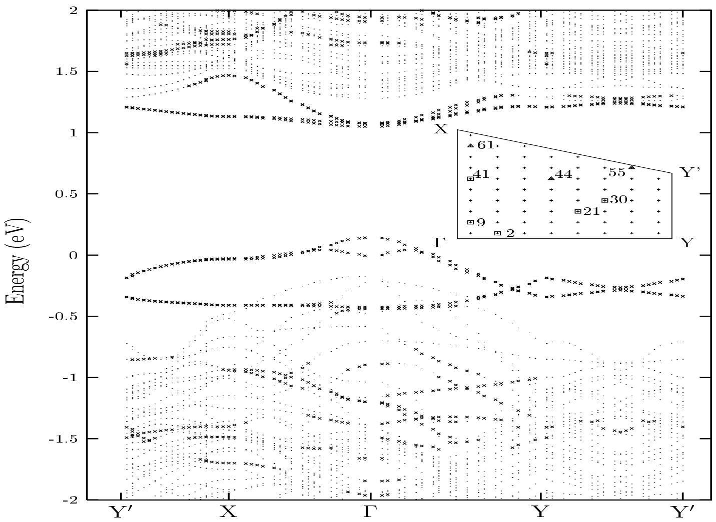

Figure 4.12: The band structure for the clean Si(100)c(4×2) surface obtained within the SETB model is shown. The dots (crosses) are bulk (surface) states. In the inset, the lines of maximum symmetry of the irreducible part of the first Brillouin zone are shown, where the special 64 κ points are shown for reference (pluses). They are enumerated progressively from left to right and from bottom to top, starting from the left lower corner. Points $\kappa = 2, 9, 21, 30, 41$ (squares) are for S$_0$ and $\kappa = 44, 55, 61$ (triangles) are for S$_1$ (see text).

component of $\overset{\leftrightarrow}{X}$ gives the non-linear (SH) polarization along i for a perturbing field along j and k. With the dimers of the c(4×2) surface oriented along x, X_{xxz} (X_{yyz}) gives the SH polarization parallel (perpendicular) to the dimers for a p-polarized fundamental field oriented also parallel (perpendicular) to the dimers.

From Fig. 4.13, it is seen that for the C terms, there are several 2ω transitions along κ which carry very little or no weight from their corresponding summands, and only two of these transitions are actually important. They coincide in κ value with the 1ω transitions, which show similar weights. We see that for $\kappa = 2$ the xxz term of the 2ω transition almost cancels the xxz of the 1ω transition, and that for $\kappa = 9$ these two contributions add. Also, at this κ, the yyz components of the 1ω and 2ω terms cancel each other. Furthermore, it can also be shown that the resonant contribution comes from the energy denominators of Eqs. (4.11a) and (4.11b), and not from the momentum matrix elements. From the 2DBZ shown in Fig. 4.12, it is seen that $\kappa = 2, 9$ are near the Γ point and along ΓY and ΓX directions, respectively, although only $\kappa = 9$ gives a finite contribution.

In contrast with $\chi^{1\omega,C}(s,s,s)$ and $\chi^{2\omega,C}(s,s,s)$, the summands of Eq. (4.11d) which

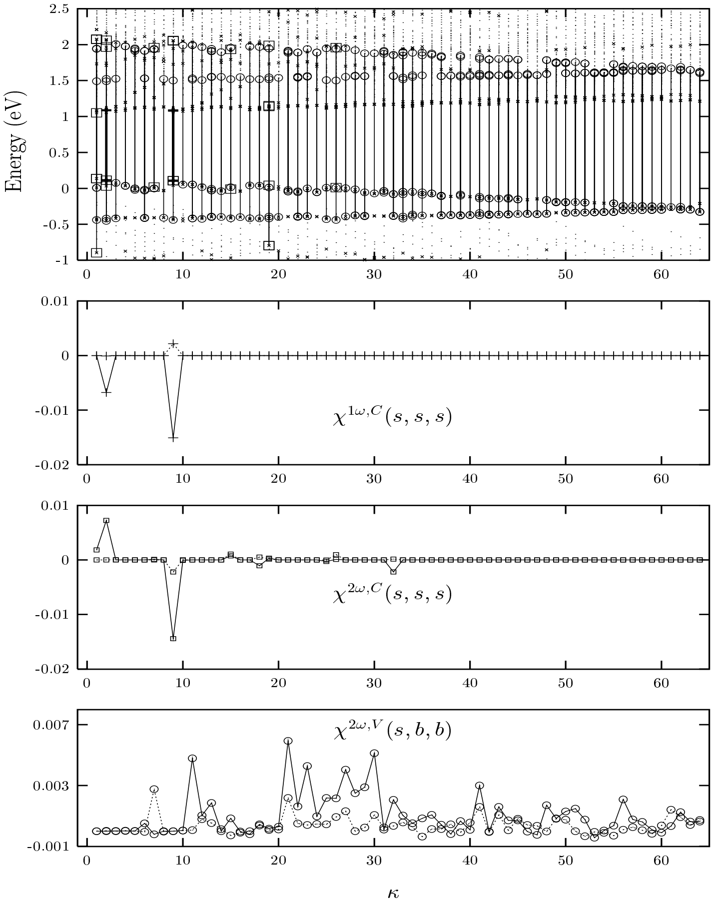

Figure 4.13: For S_0, we show the band structure along the 64 κ points shown in the inset of Fig. 4.12, along with the 1ω $s-s$ transitions (thick lines with pluses), 2ω $s-s$ transitions (thin lines with squares), and $s-b$ 2ω transitions (thin lines with open circles). The dots (crosses) are bulk (surface) states. The lower panels show the corresponding value of the xxz component (with a solid line as guide to the eye) and the yyz component (with a dotted line as guide to the eye), of the summands of Eq. (4.11a) for $\chi^{1\omega,C}(s,s,s)$, Eq. (4.11b) for $\chi^{2\omega,C}(s,s,s)$, and Eq. (4.11d) for $\chi^{2\omega,V}(s,b,b)$.

add up to $\chi^{2\omega,V}(s,b,b)$, show a different behavior as a function of κ. The value of the summands is distributed over the full 2DBZ with the largest contributions well inside the BZ, and the xxz and yyz add each other with the same sign. It is also seen that for a given κ there are several $s-b$ 2ω transitions across the gap which contribute to the susceptibility. Finally, the resonant contribution comes from the momentum matrix elements of Eq. (4.11d) and not from the energy denominator as in the previous case.

Once we have identified the eigenstates among which the transitions sketched in Fig. 4.1 take place for S_0, we can go further down into the calculation of χ, and find out the nature of their associated wave functions. The three states (i,I,v) at $\kappa=9$ for $\chi^{1\omega,C}(s,s,s)$ and $\chi^{2\omega,C}(s,s,s)$ have the following nature: (i) the wave function is strongly localized in the top and bottom atoms of the dimer with very little contribution from the atoms below the dimer; (ii) the i state (valence state) has dominant p_z-like orbitals and the I state (conduction state) has dominant p_y-like orbitals and both are strongly localized in the top atom of the dimer; (iv) on the other hand, the m state (virtual state) has an admixture of p_z-like and p_x-like orbitals for the top atom of the dimer, whereas it shows a dominant p_z-like orbital for the bottom atom of the dimer. We mention that the the transitions to the virtual state m are dominant for the states which are separated by $\hbar\omega$ from their I states. On the other hand, for the analysis of $\chi^{2\omega,V}(s,b,b)$ we sample over some representative values of κ (like $\kappa=21,30$ and 41, see Fig. 4.12), to obtain the following information: (i) the i state is strongly localized in the top Si of the dimer with an admixture of s and p_z orbitals, (ii) the I state, being a bulk state, has its wave function spread over all atoms, but it has a large amplitude at the bottom Si of the dimers with an admixture of p_y and p_z orbitals, (iii) for the m state, which is now a valence state, there are several states that contribute to the susceptibility, in contrast with the previous case, where there is only one m state for each $i-I$ electronic transition. Again, by sampling on these many states we find dominant p_x and p_z orbitals, and that their wave functions are spread over all atoms, in agreement with their bulk character, but there is no atom whose wave function dominates, as it is for the I state.

As a result of the above behavior, the electron undergoes a 1ω transition among surface states that are localized to within the dimer atoms (see Fig. 4.2). For the 2ω transitions there are two possibilities, the electron may stay within the surface states of the dimer atoms, or it may also undergo transitions from the surface states of dimer atoms to the subsurface atoms as the I and m states are bulk states. In Fig. 4.14, we show a sketch of the transitions involved in S_0.

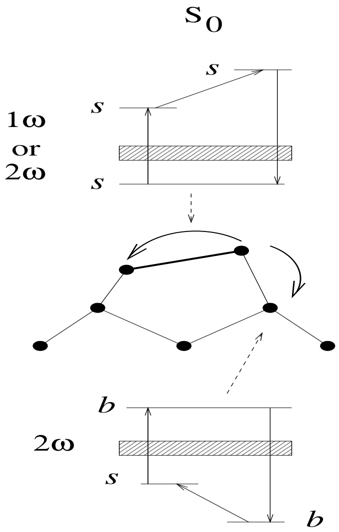

Figure 4.14: We show a sketch of the transitions involved in S_0. The Si atoms are shown by solid circles and the dimer bond by a thick solid line. The upper diagram corresponds to the dimer confined transitions, and the lower diagram to the transitions from the top Si of the dimer to a Si in the second atomic plane. The diagrams, as in Fig. 4.1, indicate the type of ω transition and the bulk or surface character of the states involved.

From the $\chi^{n\omega,v}(i,I,m)$ components of χ, we see how they involve different electronic processes which contribute to SHG. In these transitions the electron samples different symmetries of the wave function for the 1ω and the 2ω processes, and it is mostly confined to within the dimer and subsurface region.

S_1 resonance

As for S_0, figure 4.15 shows the transitions involved in S_1 in a similar fashion, where κ only ranges from 30 to 60, since the other points have transitions with no weight. We notice that only a few κ points contribute to $\chi^{1\omega,C}(s,s,b)$ for the 1ω transitions and to $\chi^{2\omega,V}(b,s,s)$ for the 2ω transitions. For the 1ω transitions the yyz component of $\overset{\leftrightarrow}{X}$ dominates over the xxz component and they partially cancel each other, whereas for the 2ω transitions, only the yyz component contributes. The two dominant κ points for the 2ω transitions are close to X and Y' along the $X\Gamma$ and $Y'X$ directions, respectively, however for the 1ω transitions, the dominant κ points are well inside the 2DBZ (see Fig. 4.12), as it is for the $\chi^{2\omega,V}(s,b,b)$ component of S_0. For S_1, the resonant contribution comes from the energy denominators of Eqs. (4.11a), (4.11d), and not from the momentum matrix elements.

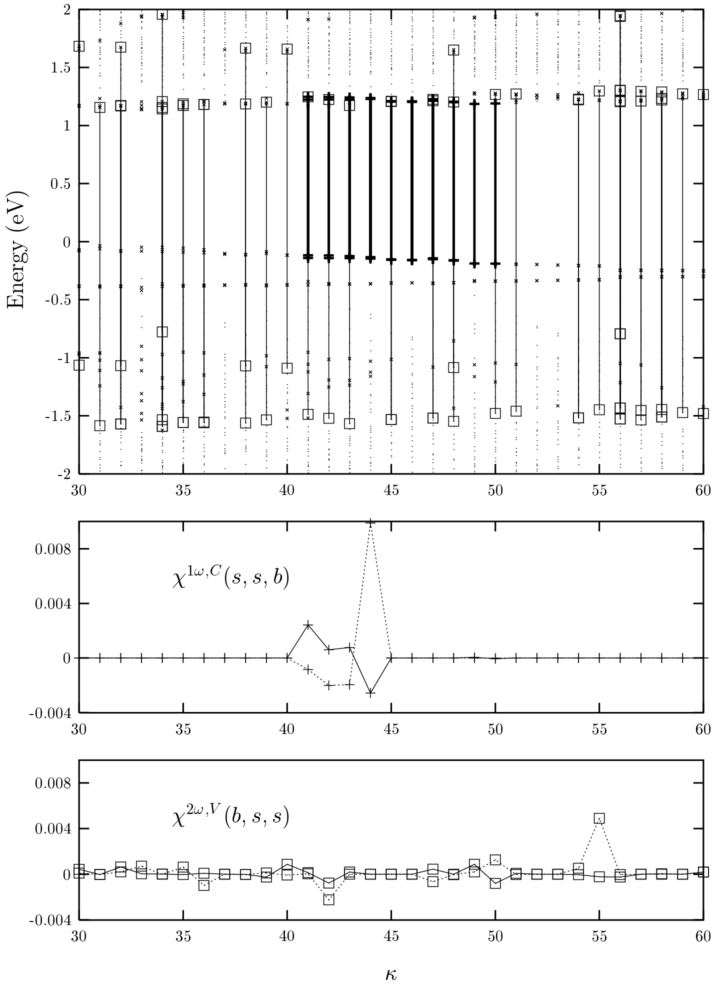

Figure 4.15: For S_1, we show the band structure from $\kappa = 30$ to 60 as these are the values of κ for which the transitions have finite contribution. We also show the 1ω $s-s$ transitions (thick lines with pluses), and 2ω $b-s$ transitions (thin lines with squares). The dots (crosses) are bulk (surface) states. The lower panels show the corresponding value of the xxz component (with a solid line as guide to the eye) and the yyz component (with a dotted line as guide to the eye), of the summands of Eq. (4.11a) for $\chi^{1\omega,C}(s,s,b)$, and Eq. (4.11d) for $\chi^{2\omega,V}(b,s,s)$.

We take some of the dominant κ values from the bottom panel of Fig. 4.15 to investigate the nature of the wave functions involved in S_1, as it was done for S_0. For $\kappa = 44$ which is related to a 1ω transition, it is found that the wave function for the valence states is concentrated in the top atom of the dimers, whereas for the conduction states is larger for the bottom atom of the dimers. The wave function of the former has an admixture of p_x and p_z orbitals, and that of the latter has dominant p_z orbitals. The bulk atoms have negligible wave functions for conduction and valence states. For $\kappa = 55$ and 61, which are related to 2ω transitions the behavior is as follows. The valence states wave functions have similar values for the 4 atoms of the unit cell at the second atomic plane (see Fig. 4.2) and all have dominant p_z orbitals. On the other hand, the conduction states wave functions have a dominant contribution for the lower atom of the dimers, with p_z orbitals, but also equally large wave functions exists for the atoms of the 3rd plane which are directly below the dimer rows (see Fig. 4.2). These two atoms display p_x and s^* dominant orbitals. Although the wave function associated to valence states are finite for the bulk atoms, the conduction states have negligible wave functions. In this way, the transitions concentrate to within the surface and subsurface atoms. Therefore, it is concluded that for S_1 the 1ω transitions that contribute to $\chi^{1\omega,C}(s,s,b)$ are mainly from the top to the bottom Si in the dimers, whereas the 2ω transitions that give $\chi^{2\omega,V}(b,s,s)$ are mainly from a Si in the second plane to either a bottom Si of the dimers or a Si in the 3rd plane just below the dimer rows. In Fig. 4.16, we show a sketch of the transitions involved in S_1. In a space-extended view of the wave function, these transitions will be among the electronic states of the corresponding bonds, i.e. dimer bonds, back-bonds and bulk Si-Si bonds. This sort of real-space visualization of the wave-function (or its charge density) has been used in Ref. 12 in order to understand the linear optical behavior of a Si(111)2×1 surface.

E_1 resonance

Figure 4.17 shows for E_1 the summands of Eq. (4.11b) for the 2ω transitions that add up to $\chi^{2\omega,C}(s,b,s)$, $\chi^{2\omega,C}(s,b,b)$, and $\chi^{2\omega,C}(b,b,b)$, along with the summands of Eq. (4.11d) which give $\chi^{2\omega,V}(b,b,b)$ vs. κ. The summands are separated into their xxz and yyz components, as in Fig. 4.13 for S_0 and Fig. 4.15 for S_1 however, for E_1 the energy bands and 2ω transitions are not shown since there are many of them and will not display clearly. From Fig. 4.17, we see that the summands of $\chi^{2\omega,C}(s,b,s)$ and $\chi^{2\omega,C}(s,b,b)$ which involve surface states, have only a few dominant terms, whose

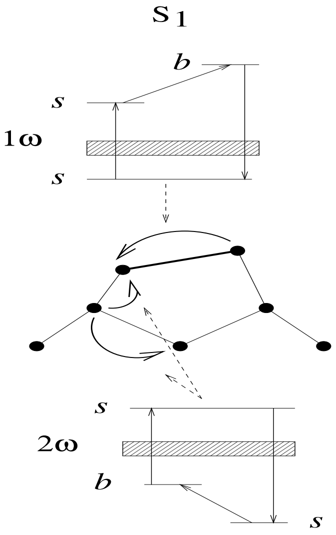

Figure 4.16: As in Fig. 4.14, we show a sketch of the transitions involved in S_1. The upper diagram corresponds to the dimer confined transitions, and the lower diagram to the transitions from the Si in the second atomic plane to either the bottom Si of the dimer or the Si in the third atomic plane just below the dimer (see Fig. 4.2).

xxz and yyz components tend to cancel each other exactly. However, the summands of $\chi^{2\omega,C}(b,b,b)$ and $\chi^{2\omega,V}(b,b,b)$ which only involve bulk states, have much more finite terms spread over the full 2DBZ, where the almost exact cancellation of the xxz and yyz contributions is not as well defined as for the terms that involve surface states. Indeed, as a function of κ, the xxz component is very small where the yyz component is large, and *vice versa*. This marked difference from surface or bulk states has to do with the fact that there are much more bulk states, and thus far more available transitions. For E_1, the resonant contributions to the summands of $\chi^{2\omega,C}(b,b,b)$ and $\chi^{2\omega,V}(b,b,b)$ come from the momentum matrix elements, in contrast with $\chi^{2\omega,C}(s,b,s)$ and $\chi^{2\omega,C}(s,b,b)$ for which they come from the energy denominators as it is for some terms of S_0 and all the contributions to S_1. This means that for S_1 the virtual transitions from the intermediate state I happen to many virtual states m (as it is for the $\chi^{2\omega,V}(s,b,b)$ term of S_0), whereas for S_0 these transitions only happen between states that are separated in energy by $\hbar\omega$. Recall that this apparent energy conservation is not physically required, only the real transition between valence (i) and conduction states (I) across the gap need to conserve energy, as indicated by the Dirac deltas in Eqs. (4.8) and (4.11). Notice that there are no contribution to E_1 coming from 1ω transitions. The contribution from $\chi^{1\omega,V}(b,s,b)$ near E_1 is cancelled by that of $\chi^{2\omega,V}(b,s,s)$ as can be seen from Fig. 4.8. Taking some values of κ for which the summands of Fig. 4.17 are largest, we conclude that the wave functions for the valence states are evenly distributed among all atoms in the unit cell

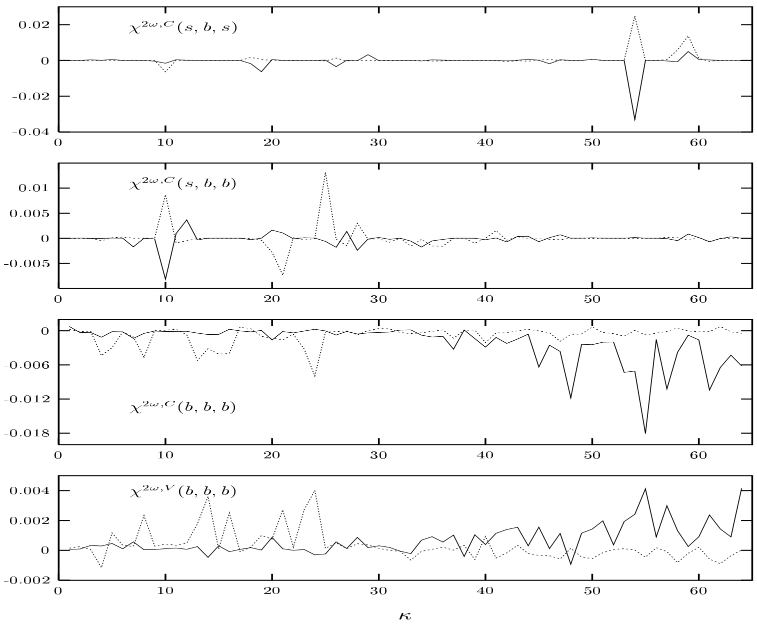

Figure 4.17: For E_1, we show the xxz (solid line) and yyz (dotted line) components of the summands of Eq. (4.11b) that add up to a) $\chi^{2\omega,C}(s,b,s)$, b) $\chi^{2\omega,C}(s,b,b)$, c) $\chi^{2\omega,C}(b,b,b)$, and of Eq. (4.11d) that gives d) $\chi^{2\omega,V}(b,b,b)$.

for surface and bulk layers, and that they have a mixture of p_x, p_y and p_z orbitals. On the other hand, the wave functions for the conduction states have strong maxima for the lower Si of the dimers with strong p_z orbitals. Therefore, it might be concluded that for E_1, transitions among the bulk and the lower atoms of the dimer contribute to the SHG signal for E_1. In Fig. 4.18 we show a sketch of the transitions involved in E_1. It is quite interesting to point out how E_1, which is a bulk resonance, is affected by the surface properties, and how the surface itself differs from the bulk, thus breaking the inversion symmetry and readily allowing SHG. The delicate balance among the different terms that enter $\overset{\leftrightarrow}{\chi}$, ultimately give the origin of the resonances seen in the SHG spectrum.

4.4 Conclusions

We have applied a microscopic formulation to analyze the different terms that contribute to the total non-linear susceptibility with which we calculate SHG. As an example the Si(100)c(4×2) surface was analyzed. We have shown within our formalism that taking into account only the $\chi_{\parallel\parallel\perp}$ component of the susceptibility tensor in the calculation of SHG yields a spectrum that well resembles the experimental results in the frequency

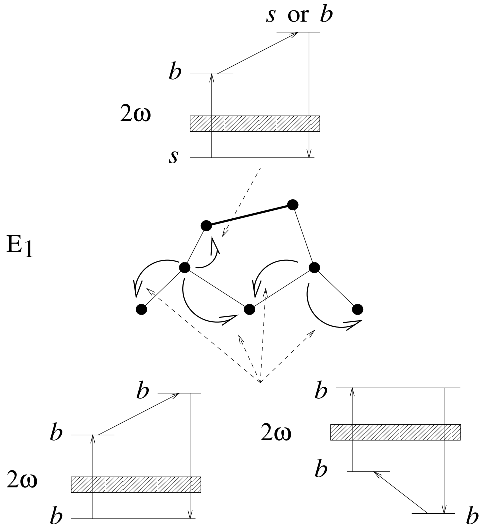

Figure 4.18: As in Fig. 4.14, we show a sketch of the transitions involved in E_1. The upper diagram corresponds to the transitions from the Si in the second atomic plane to the bottom Si of the dimer, and the lower diagram to the transitions from any Si in the second atomic plane to any Si in the third atomic plane.

range from 2 to 4 eV. Classifying the 1ω and 2ω contributions of $\chi_{\parallel\parallel\perp}$ into their surface or bulk character we discussed the energy-space and $\vec{k}$-space features of the S_0, S_1, and E_1 resonances. From this analysis and within our model we have concluded the following.

The S_0 resonance comes from 1ω and 2ω surface-surface transitions across the gap, whose transitions are to surface virtual states in the conduction band, and it also comes from 2ω surface-bulk transitions across the gap, whose transitions are to virtual bulk states in the valence band (see Fig. 4.14). The transitions occur from the top to bottom Si of the dimer, however the transitions to virtual bulk states in the valence band that are part of the surface-bulk contribution, could be to subsurface atoms.

The S_1 resonance has its origin in 1ω surface-surface transitions across the gap, whose transitions are to virtual bulk states in the conduction band, and in 2ω bulk-surface transitions across the gap, whose virtual transitions are to virtual surface states in the valence band. The 1ω transitions are from the top to the bottom Si of the dimer, and the 2ω transitions are from a Si in the second plane to either the bottom Si of the dimer or a Si in the third plane just below the dimer rows (see Fig. 4.16).

The bulk E_1 resonance has more contributions than the previous two surface peaks, but only from 2ω transitions (see Fig. 4.18). They are given by, surface-bulk transitions across the gap whose transitions are into surface and bulk conduction virtual states, and bulk-bulk transitions across the gap whose transitions are into bulk conduction or valence virtual states. Since E_1 is a bulk resonance, it is important to remark that it is strongly affected by the surface, i.e. the E_1 transitions are among the bulk atoms and the lower atoms of the dimer. This fact also shows how the surface breaks the bulk inversion symmetry readily allowing dipolar SHG.

From the above conclusions, we can understand within our approach some of the general features seen in SHG from this surface when it is covered by other species of atoms. For instance, as a function of H termination of the surface, the dimer first symmetrizes and then breaks, disrupting the dimer related states, and thus quenching the surface resonances. However the E_1 resonance, being less sensitive to the dimer as it involves transitions among subsurface atoms, does not disappear completely. This is the behavior seen in the experimental [31] and in the theoretical spectrum [45]. On the other hand, B adsorption on this surface shows a very interesting behavior for the E_1 resonance. Since B goes to second layer Si sites, its influence is not of quenching, but rather redshifting the position of E_1 and increasing its intensity, since it interacts with the subsurface atoms as well as the bottom Si of the dimer. In Chap. 5 theory and experiment are compared for such a system. A similar analysis using the model presented in this chapter could be applied for other surfaces. We remark that such analysis could be carried out using different approaches to calculate the one-electron energies and momentum matrix elements required for the evaluation of the non-linear susceptibility.

From the analysis carried out within the present model, it should be clear how the fine interplay of surface and bulk 1ω and 2ω transitions gives the observed SHG spectrum. Also, we emphasize that the bulk or surface nature of a electronic state does not imply that it belongs to a surface or bulk atom completely, rather that its wave function is distributed among surface, subsurface and bulk atoms. The influence of both surface and bulk clearly shows up in the different terms of the susceptibility that give the SHG spectra, which is a statement of the known fact that the surface states are bulk perturbed and *vice versa*. We mention that further investigation of the present model could be made along the following lines. For instance, one can try to explore the improvement of the SETB method itself along the lines of Ref. 114, or Ref. 115 where the optical matrix elements are computed directly, instead of being adjusted as in this thesis [100, 110]. Also, the alternative approach which uses the longitudinal gauge for the calculation of $\overleftrightarrow{\chi}$, and thus splits it into inter-band and intra-band contributions [116], should be compared with the present formalism which uses the transverse gauge with no intra-band processes. This comparison will allow us to asses the role of the intra-band contributions to SHG in semiconductors. Finally, as we mentioned before, proper screening of the electric field near the surface, local field and excitonic effects should be incorporated into the theory of SHG to have a full understanding of it. Our approach is a first successful step towards this aim.

Chapter 5

SHG of H-adsorbed and B-doped Si(100) surfaces

5.1 Introduction

The adsorption of foreign atoms on a surface modify its atomic structure and thus its physical properties. These adsorbates can act as a surfactant or can passivate the surface. Therefore they play an important role in surface growth by affecting the kinetics and dynamics of adsorbate interactions with semiconductors surfaces.

Recently surface specific optical techniques such as second harmonic generation (SHG) have been applied to study adsorbed-covered and doped surfaces [29,31–33,103]. Due to the technological importance of the Si surfaces, the adsorption and desorption of H on Si surfaces have been studied experimentally [29,31–33,117–119] and theoretically [120–123] for the good characterization of Si surfaces and for the control on the epitaxial growth of Si films by chemical vapor deposition (CVD). H passivation of silicon-based devices reduces the number of active dangling bonds that act as charge and impede device operation. For these reason the interaction of H on Si surfaces, in particular the (100) surface, has been widely studied.

It is now established that when the Si(100) surface is passivated with H the temperature at which the dosing occurs determines the degree of adsorption of H on the Si surface (H/Si). This adsorption may change the surface reconstruction (see. Fig. 5.1)

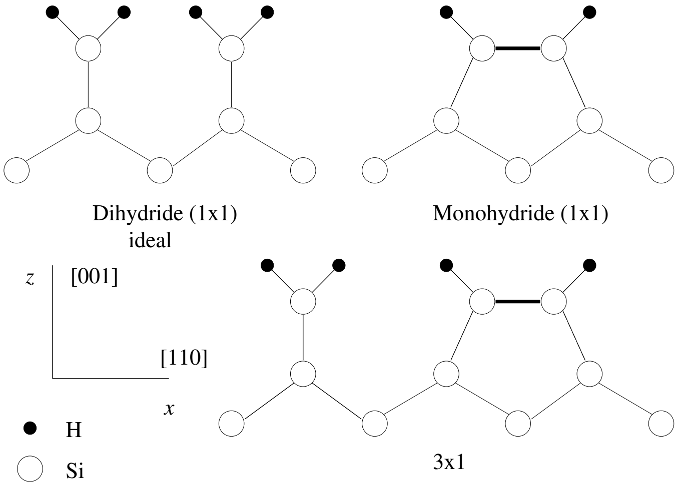

Figure 5.1: Schematic diagram of the possible structures of the H-adsorbed Si(100) surface.

at the surface as a 1×1, 2×1 or 3×1 phase [124]. At low temperatures and for coverages above 1 ML a 1 × 1 surface (ideal phase) forms on which each surface Si atom has two Si-H bonds. Above 600 K and for coverages less than 1 ML the 2×1 reconstruction which corresponds to the monohydride phase forms. The dihydride phase is formed by destroying surface dimers and changing the reconstructed 2 × 1 phase to the 1 × 1 phase. The 3×1 phase consists of alternating monohydride and dihydride units. It forms for coverage values ~ 1.3 ML and exist only on specially prepared surfaces [124].

Dadap *et al.* [31] and Höfer [32] reported measurements of SHG generated in reflection from Si(100) surfaces as a function of H coverage and temperature. They found a shift of the E_1 peak of Si as a function of H coverage: the E_1 peak redshifts by 0.1 eV in going from the clean surface to the monohydride phase, and then there is a blueshift of a smaller magnitude when proceeding towards the dihydride phase. Based on these findings Dadap *et al.* [31] proposed that surface electric fields associated with dimer formation and tilting are the dominant source of p-polarized SHG from the clean Si(100)2×1 surface, and that monohydride termination quench this contribution through chemical modification of the surface. DC surface fields approximately to 10^6 V/cm arise within the top few atomic layers of the clean 2×1 Si(100) surface due to the formation of surface dimers, even symmetric ones, induces electron transfer from the bulk into the uppermost atomic layers [31]. Jahn-Teller distortion (tilting) of the dimers cause additional charge transfer into the upper Si atom of the dimer, resulting in even stronger surface fields [83]. Thus surface dc-electric-field induced second second harmonic (SEFISH) polarization plays a major role in the SHG spectroscopy at Si interfaces [31, 33]. and differs from the bulk electric-field induced second harmonic (EFISH) polarization in which the dc-electric field penetrates a macroscopic distance determined by the bulk doping concentration [33, 125].

In this chapter, we include a suitable surface localized static electric field in the calculations of SHG at the Si(100) surface. By the inclusion of this field we will see that the E_1 peak shows the correct experimental behavior. This suggests the presence of built-in electric fields whose strength depends on the H coverage and are strongly localized in the subsurface region. A surface electric field $\vec{E}^{dc}(z) = E_z^{dc}(z)\hat{z}$, with z perpendicular to the surface, would be associated with the dimer bond formation of the clean surface as charge gets transferred to the top Si atom of each dimer [83]. The charge redistribution produces a large field strength in some portions of the immediate subsurface region. As the surface is covered with H, the charge moves back into the bulk, thus quenching the surface dc field, till it must disappear for the ideally terminated surface, i.e. the dihydride phase.

The microscopic formulation of Chap. 4 is now used to calculate the second harmonic (SH) spectra of Si(100) in the presence of surface localized dc-electric field. Adsorption of H and incorporation of B on the surface is analyzed. On one hand, we will see that the surface-allowed E_1 resonance for clean and H covered surfaces shift as a function of the dc field in agreement with experimental results. On the other hand, we will use optical second SHG spectroscopy to probe Si(001) following thermal decomposition of diborane at the surface. Incorporation of B at second-layer substitutional sites at H-free Si(001) intensifies and redshifts the E_1 SHG spectral peak, while subsequent H termination further intensifies and blueshifts E_1, in sharp contrast with the effect of bulk-B-doping or non-substitutional B. *Ab initio* pseudopotential (PP) and semi-empirical tight-binding (SETB) calculations independently reproduce these unique trends, and attribute them to the surface electric field associated with charge transfer to electrically active B acceptors, and rehybridization of atomic bonds. Part of this work is reported in Refs. [34, 126, 127].

We describe, in Sec. 5.2, two possible formulations that could be followed to calculate the SHG efficiency at Si(100) surfaces in the presence of a surface dc-electric field. The SHG experiments at the H-absorbed Si(100) surface are described in Sec. 5.3 and spectra of SHG as a function of H adsorption is reported in Sec. 5.4. The SHG as a function of H coverage on the B-doped Si(100) surface (B/Si) is analyzed through Secs. 5.5-5.7. Finally in Sec. 5.8, we give conclusions.

5.2 Effect of surface dc-electric field on SHG

From the theoretical side, two alternative formulations could be used, in principle, to calculate the effect of a surface localized dc-electric field, $\vec{E}^{dc}$ on SHG. We start from writing the non-linear second-order surface induced polarization* as [31]

$$p_i(2\omega, z) = \chi_{ijk}(\omega)E_j(\omega)E_k(\omega)\delta(z) + \chi_{ijkz}(\omega)E_j(\omega)E_k(\omega)E_z^{dc}(z) \tag{5.1}$$

where the first term on the right represents a polarization sheet commonly used to describe the dipolar SH field intrinsic of a surface, with χ_{ijk} its corresponding non-linear susceptibility. The second term is induced by the surface localized dc-electric field $E_z^{dc}(z)$ and is modulated by the fourth-rank tensor χ_{ijkz}. Both terms are driven by the external electric field $\vec{E}(\omega)$ at the fundamental frequency ω. In order to obtain the effective polarization of the surface we should integrate Eq. (5.1) as

$$\begin{aligned} p_i(2\omega) &= \int_{-\infty}^{\infty} p_i(2\omega, z)\mathrm{d}z \qquad (5.2) \\ &= \chi_{ijk}(\omega)E_j(\omega)E_k(\omega) + \chi_{ijkz}(\omega)E_j(\omega)E_k(\omega)E_0L_{eff}\eta, \end{aligned}$$

where we have assumed $E_z^{dc}(z) = E_0 f(z)$ with L_{eff} its effective depth, $\eta = \int_{-\infty}^{\infty} f(\zeta)d\zeta$. Therefore we can write Eq. (5.2) as

$$p_i(2\omega) = \chi_{ijk}^{eff}(\omega)E_j(\omega)E_k(\omega), \tag{5.3}$$

with an effective non-linear susceptibility given by

$$\chi_{ijk}^{eff} = \chi_{ijk} + \lambda\chi_{ijkz} \tag{5.4}$$

and $\lambda = E_0\eta L_{eff}$. According to the estimations of Ref. 31 λ is less than one.

Energy minimization calculations that predict a symmetric dimer structure indicate electron enrichment of approximately $e/6$ in the top two atomic layers, implying a surface charge density $\sigma = 10^{-5}\,\mathrm{C/cm^2}$ and field strength of the order of $E_0 \sim \sigma/\epsilon \sim 10^4\,\mathrm{kV/cm}$ (with $\epsilon \approx 11.9$) immediately beneath the surface [31]. Calculations that predict a tilted dimer indicate an even larger transfer of approximately $e/3$ into the upper Si atom of each buckled dimer, implying proportionately larger charge density and field strength

---

[*] An equivalent expression including static bulk fields describes the EFISH generation arising when a dc-electric field is applied externally to the sample [125].

in some portions of the immediate subsurface region, depending on the details of the charge redistribution. Similar E_0 values and vertical extent are implied by the decrease of 0.35 eV of the ionization energy of the Si(100)2×1 surface, which is observed when monohydride termination passivates and symmetrizes the surface dimer and quenches the surface field. This implies [31] $E_0 L_{eff} = 0.35V$.

As we see in Eq. (5.4), the effective susceptibility requires the calculation of the third-order susceptibility. This calculation is performed following perturbation theory just as we did in obtaining the second-oder susceptibility X_{ijk} in Sec. 4.2. Similarly to Eq. (4.5), we apply perturbation theory to obtain the third order induced current as

$$\begin{aligned} J_i = & < \psi^{(0)}|\hat{J}_i|\psi^{(3)} > + < \psi^{(3)}|\hat{J}_i|\psi^{(0)} > \\ + & < \psi^{(1)}|\hat{J}_i|\psi^{(2)} > + < \psi^{(2)}|\hat{J}_i|\psi^{(1)} >, \end{aligned} \tag{5.5}$$

where the wave function $|\psi^{(n)} >$ to n-th order is given by Eq. 4.5. After substitution of Eq. (5.5) into Eq. (4.3), we could obtain the corresponding expression for the third-order non-linear susceptibilities [128] which we do not give explicitly because they are cumbersome. Thus, we just mention that such an expression contains terms proportional to $\delta(E - \hbar\omega)$, $\delta(E - 2\hbar\omega)$ and $\delta(E - 3\hbar\omega)$ similarly to Eq. 4.8, which contains terms proportional to $\delta(E - \hbar\omega)$ and $\delta(E - 2\hbar\omega)$. In Fig. 5.2 we give an sketch, similar to that of Fig. 4.1, of the possible transitions 1ω, 2ω and 3ω involved in χ_{ijkz}. These transitions could take place to surface or bulk virtual states in the conduction or valence band.

Due to the cumbersome character of the calculation of χ_{ijkl}, we follow an alternative method to calculate the optical response of a surface in the presence of a surface localized field, which consists in adding to the original SETB unperturbed hamiltonian $\hat{\mathcal{H}}_0$, the electrostatic potential produced by $\vec{E}^{dc}(z)$. Within the electric dipole approximation, $\vec{E}^{dc}(z)$ is included into $\hat{\mathcal{H}}_0$ as a potential energy dependent of z as

$$\hat{\varphi}(z) = eV(z) \tag{5.6}$$

with

$$\frac{\mathrm{d}V(z)}{\mathrm{d}z} = -E_z^{dc}(z) \tag{5.7}$$

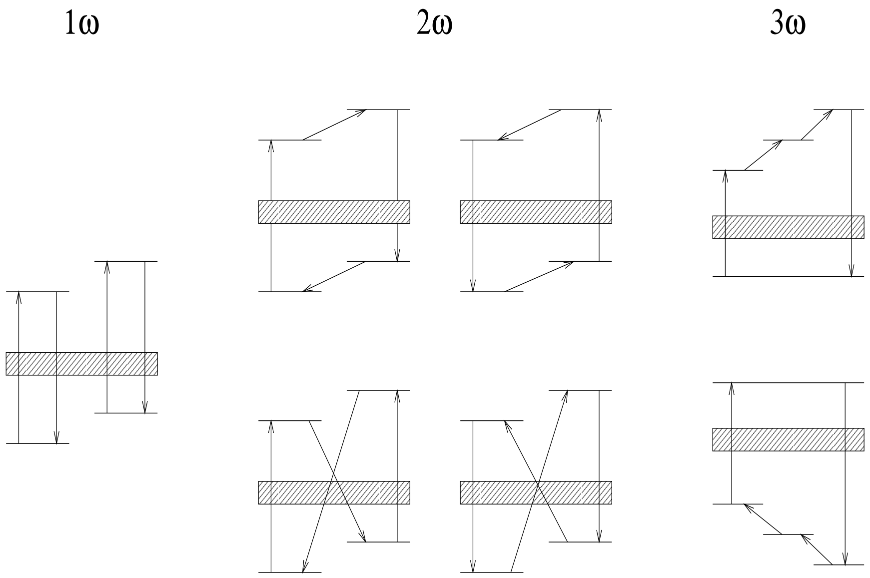

Figure 5.2: We show an sketch of the possible 1ω, 2ω and 3ω transitions involved in the third-order non-linear susceptibility χ_{ijkz}.

and calculate the ground state eigenvalues and eigenfunctions of this new hamiltonian

$$\hat{\mathcal{H}} = \hat{\mathcal{H}}_0 + \hat{\varphi}(z) \tag{5.8}$$

with which one calculates χ_{ijk}. Now, in this approach the key ingredient for the calculation are the matrix elements of $\hat{\varphi}(z)$.

We use a tight-binding (TB) approach to calculate the energy and momentum matrix elements required in Eq. 5.8. Then, for a general potential of the form $\varphi(z) = \varphi_o f(z)$, we have that the matrix elements between orbitals n and n' situated at atoms with positions $\mathbf{R}$ and $\mathbf{R}'$ are given by

$$< n\mathbf{R}|\varphi(z)|n'\mathbf{R}' >= \varphi_0 < \phi_{n\mathbf{R}}|f(z)|\phi_{n'\mathbf{R}'} > \tag{5.9}$$

where the TB wave functions are

$$\phi_{n\mathbf{R}} = \sum_{\mathbf{R}} \exp(i\vec{k} \cdot \mathbf{R}) u_n(\mathbf{R}), \tag{5.10}$$

with $\vec{k}$ the wave vector and $u_n(\mathbf{R})$ a periodic function. Substituting Eq. (5.10) into Eq.

(5.9) and taking $z \to z + R_z$, where R_z is the atomic z-coordinate, we obtain

$$< n\mathbf{R}|\varphi(z)|n'\mathbf{R}' >= \delta_{\mathbf{R}\mathbf{R}'}\varphi_o < u_n(\mathbf{R})|f(z+R_z)|u_{n'}(\mathbf{R}) >, \tag{5.11}$$

where we have neglected the inter-atomic matrix elements. Expanding the function $f(z+R_z)$ in a power series of z around $z = 0$ and limiting to the first-order term, we have

$$< u_n(\mathbf{R})|f(z+R_z)|u_{n'}(\mathbf{R}) >= f(R_z)\delta_{nn'} + < u_n(\mathbf{R})|z|u_{n'}(\mathbf{R}) > \left.\frac{\mathrm{d}f}{\mathrm{d}z}\right|_{z=0}. \tag{5.12}$$

For a constant dc-electric field $E_z^{dc} = E_0$ whose corresponding potential is given by

$$\varphi(z) = -(\varphi_o/a_B)z, \tag{5.13}$$

and $f(z) = -z$, we have

$$< n\mathbf{R}|\varphi(z)|n'\mathbf{R}' >= -(R_z\delta_{nn'} + z_{nn'})(\varphi_o/a_B)\delta_{\mathbf{R}\mathbf{R}'} \tag{5.14}$$

where

$$z_{nn'} =< u_n(\mathbf{R})|z|u_{n'}(\mathbf{R}') >, \tag{5.15}$$

and we have normalized with the Bohr radius a_B. Whereas, for a dc-electric field that decays exponentially,

$$\phi(z) = \phi_o e^{-z/L_{eff}}, \tag{5.16}$$

and $f(z) = \exp(-z/L_{eff})$, thus

$$< n\mathbf{R}|\varphi(z)|n'\mathbf{R}' >= (\delta_{nn'} - z_{nn'}/L_{eff})\delta_{\mathbf{R}\mathbf{R}'}\,\varphi_o e^{-R_z/L_{eff}}. \tag{5.17}$$

To calculate the intra-atomic matrix elements $z_{nn'}$ needed in above equations, we use a semi-empirical approach within our TB formalism. For the SETB approach we use a $sp^3s^\star$ basis, with which the different parameters involved are obtained by a fit to bulk Si optical properties. For $z_{nn'}$, the only elements different from zero are $< s|z|p_z >= 0.27$ Å, and $< s^\star|z|p_z >= 1.08$ Å [110]. The matrix elements of the momentum operator, calculated through $\hat{\vec{p}} = im[\hat{\mathcal{H}}, \hat{\vec{r}}]/\hbar$, are unaffected by $\varphi(z)$ since it commutes with $\hat{\vec{r}}$. The addition of Eqs. (5.14) or (5.17) to the SETB hamiltonian $\hat{\mathcal{H}}_0$, allows to calculate the ground state of the system in the presence of $E_z^{dc}(z)$, from which the more simple expression of χ_{ijk} could be readily calculated through Eq. 4.8.

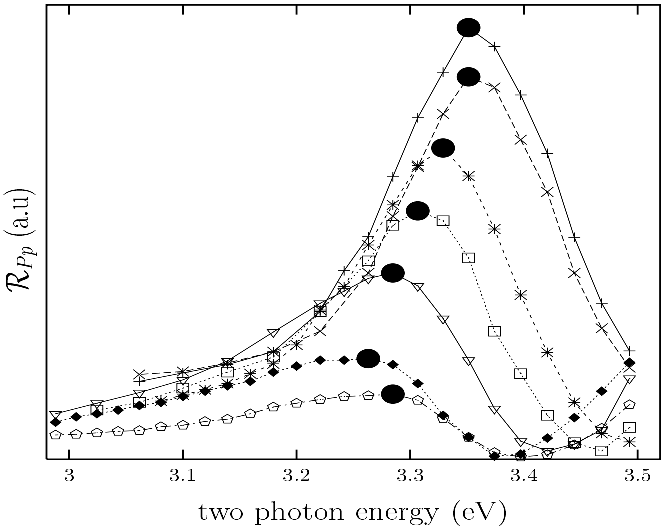

Figure 5.3: Isothermal p-in/P-out SHG. Experimental spectra from Ref. 31 of 8 isosteric Si(001) surfaces with H coverage of 0, 0.12, 0.3, 0.51, 0.75, 1 and 1.5 ML from top to bottom respectively at room temperature. We observed a quenching, redshift and line distortion of the E_1 resonance as coverage increases from 1.0 to 1.5 ML and blueshift as coverage increases from 1.0 to 1.5 ML. In order to follow the shift and quenching of the E_1 resonance we have indicated with a circle the maxima of the spectra.

5.3 SHG experiments at H-adsorbed Si(100) surface (H/Si)

Experimental studies of H adsorption at Si(100) surface have shown the importance of surface SEFISH polarization in the SHG spectroscopy at Si surfaces [29–31, 33, 125]. Daum *et. al.* [29, 30] proposed that the SH E_1 peak at clean Si(100)2×1 acquires its amplitude and redshifting primarily from near-surface vertical tensile strain induced by dimerized reconstruction and by this interpretation they explained the quenching of the resonance by H coverage. On the other hand Dadap *et al.* [31] explained the origin of the E_1 peak at Si(100)2×1 by the surface dc-electric field that arises from the charge transfer accompanied with dimer bond formation and tilting rather than from the near-surface strain field.

The SHG experiments to obtain SHG measurements from a Si(100) surface is described in this section. The experiments were done by Dadap *et al.* [31] at the University of Texas at Austin. With this experiments, Dadap *et al.* [31] reported isothermal and isosteric spectroscopic measurements and real time fixed wavelength measurements during heating, H desorption and epitaxial growth (time resolution $< 0.1\,\mathrm{s}$). The SH spectroscopy experiments were performed in an ultra-high vacuum (UHV) deposition chamber, equipped with a quadrupole mass spectrometer and a reflection high-energy electron diffraction (RHEED) apparatus. The deposition chamber is adjoined via a load-lock to a multitechnique surface analysis chamber (base pressure 8×10^{-11} Torr) with capabilities for Auger electron spectroscopy (AES), x-ray photoelectron spectroscopy (XPS), temperature-programmed desorption (TPD), and high-resolution electron-energy-loss spectroscopy (HREELS). The deposition chamber is pumped by a 450-1/s turbo-molecular pump to a base pressure $< 1 \times 10^{-9}$ Torr (the low-pressure limit of the Bayard-Alpert gauge), with no special provisions for pumping H, because of its low ($< 10^{-6}$) initial sticking coefficient on Si(100). This chamber is also equipped with a Roots blower, capacitance nanometer, and exhaust valve for operation at pressures up to 100 Torr. The deposition chamber is routinely exposed to large doses of silane and disilane during CVD growth, which helps maintain a low H_2O partial pressure (via gettering at the chamber walls) of approximately 5×10^{-11} Torr, estimated from residual gas analysis. The bare silicon surface can be maintained for about 15 min under these conditions without any accumulation of impurities detectable by (XPS) and TPD (< 0.01 ML). A typical SH spectrum was acquired in approximately 3 min.

The oriented p-type Si(001) substrate (miscut less than 1^o) was radiantly heated from the backside with a pyrolytic boron nitride (PBN) encased graphite heater for temperatures less than 1050 K. For higher temperatures, a coiled tungsten filament was inserted between the PBN heater and the backside of the crystal (using a linear motion device) to achieve electron beam heating to temperatures as high as 1400 K. Temperature was routinely monitored via a thermocouple, mounted to the sample holder, that was previously calibrated to the crystal temperature (to within ± 20 K). To achieve better accuracy in the temperature measurement (to within ± 5 K), the experiments used a K-type thermocouple, spot welded to the inside of a thin roll of tantalum foil, then inserted into a 0.5 mm hole through the crystal and fastened with a drop of zirconia-based adhesive (Aremco, Ultratemp 516). The native oxide was removed as SiO by 1 K/s heating to 1275 K, followed by 1 K/s cooling to ambient. This procedure has been shown to produce an atomically smooth 2×1 reconstructed surface as verified by a characteristically sharp, streaky RHEED pattern, with no impurities detectable by (XPS) and AES. Our SH measurements were performed on an undoped, epitaxial silicon layer that was grown by UHV-CVD using disilane (Airco, electronic grade mixture consisting of 4%-Si_2H_6/balance He) at 900 K to bury any trace contaminants present at this surface, and conceal the initial interface far beyond the extinction length of the SH radiation (typically a $0.3\,\mu$m layer was grown). As surface contaminants accumulated over the course of several days, the epitaxial growth procedure was routinely repeated to recover a pristine surface, with no degradation in the crystallinity nor surface roughness, as monitored by the RHEED pattern.

H coverage was controlled by exposing the bare crystal to atomic H produced by cracking molecular H on a 2000 K tungsten filament, placed in line-of-site with the crystal face at a distance of 3-4 cm. The H was purified by slowly filling an evacuated, liquid-nitrogen-cooled U tube to a pressure of 50 psi (gauge), before backfilling the chamber to the desired pressure, resulting in an H_2O partial pressure rise in the chamber to no more than 2×10^{-10} Torr at H pressures as high as 5×10^{-4} Torr. A resistively heated crystal and a line-of-site QMS were installed in the deposition chamber to quantify H coverages by TPD, while the SH spectroscopy experiments were performed concurrently on the same crystal. By normalizing the m/e 2 TPD peak areas to the area under the saturated monohydride peak, H coverages in ML were obtained with a relative accuracy of approximately 5%. Cracking of background impurities (CO, H_2O) was minimized by keeping the filament hot for no more than 30 s for each dose and varying the pressure to control the exposure. A 15 000 L (5×10^{-4} Torr, 30 s) molecular H exposure produced a saturation coverage of 1.5 ML at 375 K. H exposure was performed at no less than 375 K to minimize the formation of etch products that might lead to surface roughening. Following each exposure and SH spectroscopy experiment, the TPD heating program annealed the crystal at 1050 K to recover the smooth, double-domain (2×1) reconstructed surface.

Unamplified Ti:sapphire laser pulses of duration 120 fs, wavelength range 705-935 nm spectral bandwidth 5-10nm [full width at half maximum (FWHM)], average power 150 mW, and repetition rate 76 MHz were focused through a fused-silica viewpoint onto the (001)-oriented silicon crystal *in vacuo* at a 55^o angle of incidence. The reflected SH signal was monitored through a second optical port using a gated photon-counting system. A fraction of the fundamental laser beam was split off outside the chamber to generate a SH reference signal from a crystalline quartz plate, which normalized against drifts in average laser power or pulse duration data acquisition. Transient surface heating by individual laser pulses was negligible (< 0.5 K at $0.5\,\mathrm{mJ/cm^2}$ per pulse). However, cumulative surface heating by the 76-MHz pulse train caused a steady-state temperature difference as high as 40 to 50 K between the sample spot on the crystal and the thermocouple, mounted several mm away, when the laser operated at 200 mW average power.

This extra heating noticeable perturbed H desorption kinetics, which provided *in situ* calibration of the temperature offset. Attenuation of the incident beam to $< 50\,\mathrm{mW}$ with neutral density filters minimized laser-induced heating while maintaining adequate SH signals levels for most measurements.

For surface spectroscopy, the laser wavelength was tuned between 705 and 820 nm in pulse bandwidth (5-10 nm) increments in less than 3 min, yielding a two-photon spectral energy resolution $2\hbar\Delta\omega \approx 0.002 - 0.003\,\mathrm{eV}$. With a change in laser optics, the longer wavelength range from 800 to 935 nm was scanned in a similar manner. Spectral scans were repeated with increasing, then decreasing wavelengths to verify that contaminant adsorption did not influence the SH spectroscopy measurements during data acquisition. Periodic RHEED and (XPS) measurements indicated no appreciable contamination even after performing experiments for several days.

Experimental data of Dadap *et al.* [31] are shown in Fig. 5.3, where we see a series of room-temperature SHG efficiency $\mathcal{R}_{Pp}$ spectra of Si(100) as a function of H-coverage ranging from 0 to 1.5 ML. As H-coverage θ_H increases, three main features are observed: a) from 0 to 1 ML the E_1 resonance is sharply quenched, while from 1 to 1.5 ML there is hardly any further decrease in its amplitude; b) as the resonance quenches, its line shape distorts asymmetrically as a pronounced dip develops on its high energy side and c) from 0 to 1 ML, the peak redshifts monotonically away from the peak energy at 0 ML while from 1 to 1.5 ML, the peak blueshifts slightly back towards its 0 ML peak energy (3.36 eV). Reflection high energy electron diffraction (RHEED) patterns show that the dimerized 2×1 reconstruction persists for H-coverage up to 1 ML and converts to 1×1 for higher coverage.

5.4 SHG calculations at H-adsorbed Si(100) surface (H/Si)

We now incorporate the dc-electric field in our theory following the second formulation described in Sec. 5.2. Within the electric dipole approximation, $\vec{E}^{dc}(z)$ is included phenomenologically into the TB Hamiltonian through a potential energy along z. Relevant matrix elements were determined through matrix elements of z_{ij} (using unperturbed wave functions), and evaluated by empirical fits to experimental linear optical functions [45].

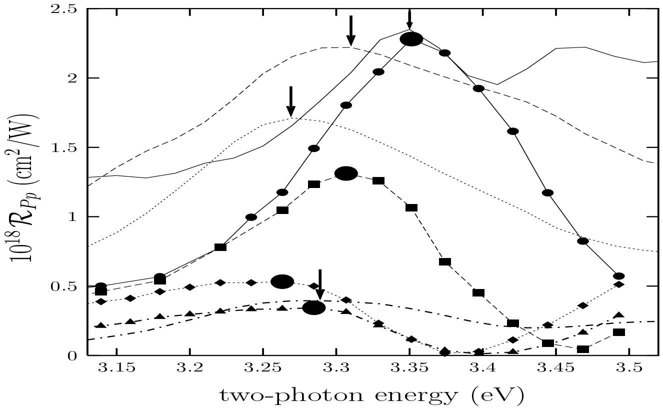

Figure 5.4: We show $\mathcal{R}_{Pp}$ for the clean Si(100) surface with c(4×2) reconstruction (solid line), a Si(100) surface with one H (dashed), with 2 H monohydride phase (dotted), and with 4 H ideally terminated dihydride phase (dotted dashed) per Si-Si dimer. The angle of incidence $\theta = 55°$ is the same as in the experiment of Ref. 31. For all curves $E_0 = 5 \times 10^6$ V/cm and $L_{eff} = a_o$ except for the ideal surface, for which $E_0 = 0$ (see text for details). The experimental spectra of Fig. 5.3 are also shown: the solid line with circles is for the clean surface, the dashed line with squares is for a surface with one H, the dotted line with diamonds is for the monohydride surface and the dot-dashed line with triangles is for the dihydride surface. We indicate with a wide filled circle the maxima of the experimental spectra.

We assume a constant dc-electric field, $E^{dc}_z(z) = E_0$, that point towards vacuum and extends to a distance L_{eff}. The following results for SHG at Si(100) were obtained.

Figure 5.4 shows $\mathcal{R}_{Pp}$ vs. the energy of the SH-photon for a clean Si(100) with c(4×2) surface reconstruction, and for a Si(100) surface with one H, 2 H (monohydride phase), and 4 H (ideally terminated dihydride phase) per Si-Si dimer, at an angle of incidence $\theta = 55°$. In the third and fourth cases all dangling-bonds are H saturated, while in the first (second) case two (one) unsaturated dangling bond per surface dimer survives. We have chosen $E_0 = 5 \times 10^6$ V/cm and $L_{eff} = a_o$, which is equivalent to 4 (100) planes, with a_o the lattice constant of Si, i.e the dc field extends four atomic planes. Because of the formation of the dimer there is a charge transfer to the upper atom of the dimer [83], thus $\vec{E}^{dc}$ points into the vacuum as the top atom gets more negatively charged.

The E_1 peak is clearly seen, and its intensity gets reduced by increasing the number of H. For this value of E_0 and L_{eff}, we see that the peak redshifts 0.05 eV as we move from the clean surface to the surface with one H per Si-Si dimer. Then, there is another redshift of 0.03 eV as we move to the monohydride phase, and then an smaller blueshift as we increase the number of H to finish in the ideally terminated dihydride phase, for which $E_0 = 0$. This behavior of the E_1 peak is in agreement with the experimental

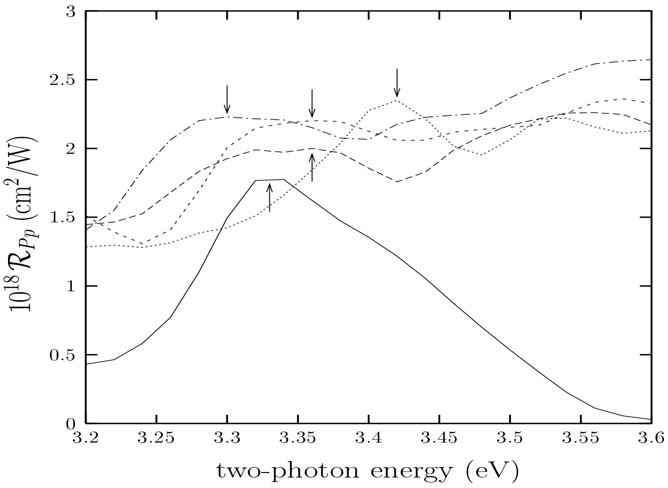

Figure 5.5: We show $\mathcal{R}_{Pp}$ vs. two-photon energy for a clean Si(100) with c(4×2) surface reconstruction. Here, $L_{eff} = a_o$, and $E_0 = 0$ (solid line), 2×10^6 V/cm (long dashed), 3×10^6 V/cm (short dashed) and 5×10^6 V/cm (dotted), for the case where $\vec{E}^{dc}$ points towards the vacuum. Also, the dot-dashed line corresponds to the case where $\vec{E}^{dc}$ points towards the bulk for $E_0 = 2 \times 10^6$ V/cm. The E$_1$ resonance of the spectra is indicated by an arrow.

behavior of Fig. 5.3 also shown in Fig.5.4.

In order to justify the values used for E_0 and L_{eff}, we have calculated the spectrum of SHG for a clean Si(100)c(4×2) surface by varying E_0 with L_{eff} fixed and vice versa. By varying the dc-electric field, we explore the magnitude of the surface dc-electric field related to H-coverage and by varying L_{eff} we investigate the extension depth of the surface dc-electric field. Figure 5.5 shows the spectrum for $\mathcal{R}_{Pp}$ vs. the energy of the SH-photon for a clean Si(100)c(4×2) surface with $L_{eff} = a_o$ and different values of E_0, along with the case for $E_0 = 0$, i.e. without the dc-electric field. It is observed that as the value of E_0 is increased, for the case of $\vec{E}^{dc}$ pointing towards the vacuum, the E$_1$ peak blueshifts by 0.1 eV from $E_0 = 0$ to $E_0 = 5 \times 10^6$ V/cm. From the same plot, we also see that if the direction of $\vec{E}^{dc}$ is reversed, i.e. pointing towards bulk, the E$_1$ peak redshifts. It is worth mentioning that it is the first case the one that corresponds to the correct physical situation. Besides the correct blueshift of E$_1$, it is also seen that the signal is enhanced as a function of $\vec{E}^{dc}$.

On the other hand, Fig. 5.6 shows the spectrum for $\mathcal{R}_{Pp}$ for a fixed value of $E_0 = 5 \times 10^6$ V/cm and for $L_{eff} = a_o/4$, $a_o/2$ and a_o. It is seen that for $L_{eff} = a_o/4$, the E$_1$ peak is only enhanced with respect to the $E_0 = 0$ case, and that for $L_{eff} = a_o/2$ and a_o is also enhanced and shifted to higher energies. This behavior shows that it is sufficient for

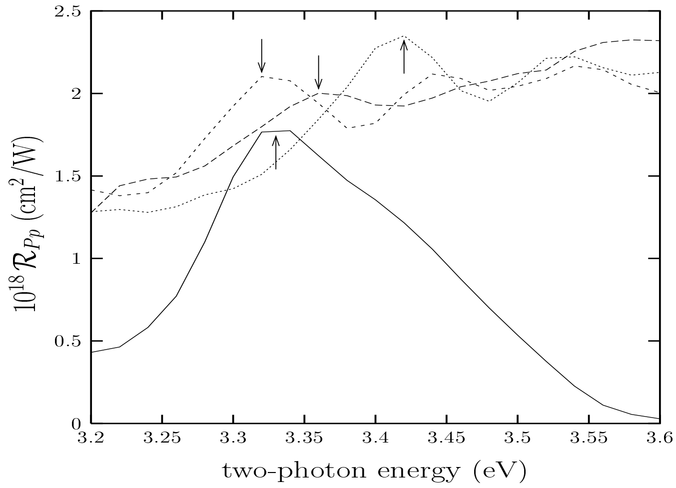

Figure 5.6: Same as Fig. 5.5, but for $E_0 = 5\times10^6$ V/cm, and $L_{eff} = a_o/4$ (short dashed line), $a_o/2$ (long dashed line) and a_o (dotted line), where $\mathcal{R}_{Pp}$ with $E_0 = 0$ is shown for reference (solid line).

the $\vec{E}^{dc}$ to penetrate only a few atomic layers in order to give the experimental behavior, and that the E_1 resonance is strongly dependent on the surface details.

From above, it is clear that the presence of the surface dc-electric field $\vec{E}^{dc}$ modifies the SHG signal of the surface allowed E_1 resonance in a physically consistent way and that its inclusion in the clean and H-covered Si(100) surfaces correctly describes the measured experimental spectra. This approximate way of including $\vec{E}^{dc}$, strongly suggests that there is a built in dc-electric field in the subsurface region of Si. As mentioned above, this field may be related to the charge transfer that takes place as the surface reconstructs to lower its energy, and the top Si atom in the dimer gets more negatively charged. An approach that would take this charge transfer effect into account self-consistently should in principle reproduce the SHG behavior of the E_1 peak for the clean and H-covered surfaces without the explicit contribution of $\vec{E}^{dc}$.

In contrast with the observed blueshift of E_1 as a function of H coverage at Si(100) surfaces, a redshift could be observed for other surfaces. This would be seen by reversing the direction of the dc-electric field, i.e pointing towards the bulk (see. Fig.5.5). For instance, in the B-doped Si(100) surface, the electronically active B, occupies second layer Si sites reversing the direction of the vacuum oriented clean surface. The study of this surface will be the subject of next section.

5.5 SHG at B-doped Si surfaces (B/Si)

Dopants play an important role in semiconductor technology and growth of surfaces and interfaces. They not only modify the electronic properties of semiconductors but also they influence the growth rate and morphology of the manufactured surface. This has motivated the need for understanding the physical mechanisms by which dopants modify the electronic properties of surfaces. For instance, B is the most widely used bulk dopant in Si-based semiconductor technology. Stable two-dimensional layers of highly B-doped Si with unique structural and electronic properties can be fabricated by depositing B at Si surfaces. Extensive experimental [129–133] and theoretical [134,135] structural studies of such layers have shown that B, unlike larger Group III atoms, enters substitutional sites below the top Si layer, resulting in a strong charge transfer from the surface Si to the underlying B acceptors. This charge transfer appears to strongly influence the unique properties of reconstructed B-doped Si(001) [131,134] and B-doped Si(111) [129], notably their unusual structures, their reduced chemical reactivity compared to clean surfaces [136–139], and their stability to deposition of Si overlayers, which enables fabrication of ordered-doped structures [132, 140].

Scanning tunneling microscopy (STM) studies made by Wang and Hamers [131] have revealed that decomposition of diborane and/or decaborane on the Si(100) surfaces produces several ordered 4×4 reconstructions. Additionally, Headrick et al. [141] reported the 2×1 surface reconstruction (see. Fig. 5.7). They found that the 2×1 reconstruction can be preserved within high quality crystalline Si by low-temperature epitaxial overgrowth at $\approx 300°$C.

Recently surface specific optical techniques such as SHG have been applied to study adsorbed-covered and doped surfaces [29, 31–33, 103]. SHG is sensitive at the monolayer (ML) level to the surface discontinuity of centrosymmetric materials such as Si [16]. Features on the SHG spectrum show unique signatures of 2nd layer B incorporation which contrast markedly with those of other Si-adsorbate surfaces [31, 32, 45].

In this thesis, we demonstrate by a microscopic theory, a remarkable contribution of vertical surface fields originating from charge transfer to electrically active B in governing SHG spectroscopy. SHG thus complements structure-sensitive probes by directly probing charge transfer which underlies B/Si surface chemistry.

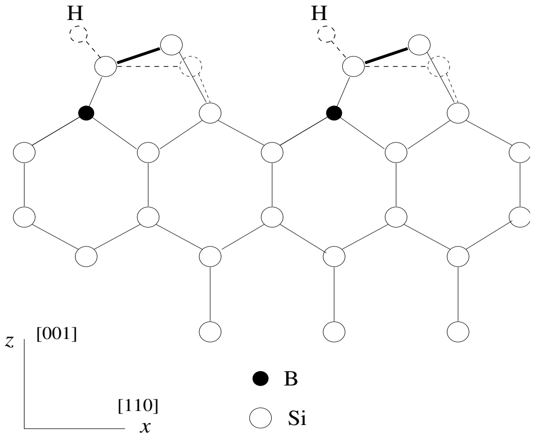

Figure 5.7: Schematic diagram of the B-doped Si(100)2×1 reconstructed surface. The dashed lines shows the symmetrization of the dimer with H adsorption.

5.6 B/Si and H-B/Si SHG experiments

In this section, we describe the SHG experiments performed by D. Lim, M. Downer and J. Ekerdt at the U. of Texas at Austin on a B/Si and H-covered B/Si (H-B/Si) surfaces. We mention that these experiments confirm our prediction of Sec. 5.4, by which the E_1 peak blueshifts as we reverse the direction of the $\vec{E}^{dc}$ field from pointing towards the surface to pointing towards the bulk [34]. The experiments were performed in an UHV chamber equipped for film growth by CVD and multi-technique surface analysis [31]. Native oxide is removed by heating the Si(001) sample to 1000°C. A 0.4 μm thick Si epilayer is then grown by CVD from disilane gas with the sample at 600°C. After reflection, high energy electron diffraction (RHEED) will show a clear 2×1 reconstructed surface, P-polarized SHG spectra is acquired by tuning unamplified, p-polarized, 120 fs Ti:sapphire laser pulses, which are focused onto the sample at 55° incidence angle, from 710 to 800 nm. Fluence is kept low enough ($< 0.3\,\mathrm{mJ/cm^2}$) that heating and carrier generation did not influence reflected SHG, which is normalized to a reference SHG signal [31]. B is then deposited by exposing the surface, at either room temperature (RT) or 600°C, to diborane (B_2H_6) gas. SHG spectra is acquired again. RT exposure leads to termination of Si dimer dangling bonds by BH_2 and H [142]. At 600°C, B tends to occupy second layer substitutional sites and to become electrically active, as shown by scanning tunneling spectroscopy [131, 143]. Additional SHG spectra is acquired after exposing the latter surface (after cooling to 150°C) to atomic H, generated by cracking back-filled H_2 with a hot tungsten filament. Measurements are repeated with increasing dosages of B_2H_6. B coverage θ_B for 600°C deposition is calibrated with $\sim 10\%$ accuracy

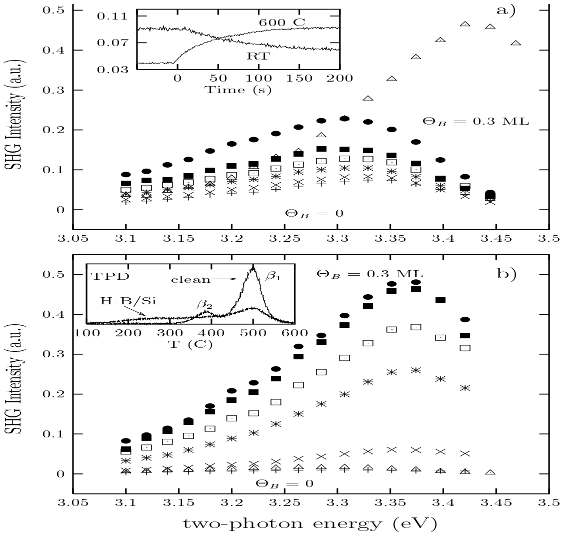

Figure 5.8: SH spectra of a) surface B-doped Si(001) and b) H-terminated B/Si(001) surface. B_2H_6 exposure are 0 L (plus signs), 2.4 L (crosses), 7.2 L (stars), 12 L (open squares), 24 L (filled squares), and 48 L (filled circles). Maximum $\theta_B \sim 0.3$ ML. Triangles in a) and b) show SH spectra for bare and H-terminated bulk-B doped samples, respectively. Inset of a): real time SHG following B_2H_6 exposure at 600°C and RT, with B_2H_6 partial pressure 2×10^{-7} Torr. Inset of b): H_2 TPD of H-Si(001) and H-B/Si(001).

by terminating this surface with atomic H at 150°C, then comparing H_2 TPD with TPD of a standard H-B/Si surface for which θ_B had been independently calibrated by Auger spectroscopy in a connected surface analysis chamber. For comparison, several 0.3 μm thick epilayers with uniform *bulk* B doping of several 10^{18} cm^{-3} are also grown from B_2H_6 disilane gas mixtures.

The SHG spectra acquired by the above procedure is shown in Fig. 5.8 for the clean and H-terminated bulk-doped films. Fig. 5.8a shows SHG spectra of clean Si(001) before (plus signs) and after (other data sets, except triangles) surface B adsorption at 600°C for θ_B up to ~ 0.3 ML. The clean Si spectrum shows the surface E_1 peak, redshifted (3.34 eV) from its bulk energy (3.4 eV) [30]. H-termination quenches this feature (Fig. 5.8b, plus signs) as reported previously [30,31]. As θ_B increases to 0.3 ML, the SHG signal from the H-free surface intensifies, and the E_1 peak redshifts continuously to $\sim$3.3 eV (Fig. 5.8a). The SHG signal rises with time constant $\sim$ 50 s following opening of the B_2H_6 inlet valve (see 600°C curve in inset of Fig. 5.8a), a delay which we attribute to the time for 2nd layer substitutional B to reach saturation coverage. For very low $\theta_B < 0.02$ ML, H termination still quenches the SHG signal as for clean Si(001) (Fig. 5.8a and b: crosses). Surprisingly for higher θ_B, H termination *intensifies* and *blueshifts* the spectral peak closer to the bulk

E_1 energy (Fig. 5.8b, upper 4 data sets), exactly opposite to the effect of H termination on clean Si(001) (see Fig. 5.3). H_2 TPD spectra for $\theta_B = 0$ and 0.3 ML (inset of Fig. 5.8b) revealed, in addition to the dihydride β_2 (380°C) and monohydride β_1 (500°C) features, a broad low temperature (150° C to 400°C) desorption feature, which does not exist for undoped Si(001), and which has been identified with Si-H bonds weakened by charge transfer to underlying B back-bonds [117,144]. With increasing θ_B the latter peak intensifies at the expense of β_2 and β_1. After selectively desorbing H associated with this low temperature feature by annealing the sample at 300°C, most of the enhanced SH signal shown in Fig. 5.8b was quenched. Thus H associated with this feature appears to be responsible for the surprising enhancement of SHG.

Figure 5.8a and 5.8b also show the SHG spectrum from the bare and H-terminated surface (triangles), respectively, of a *bulk*-B-doped film. The signal of the bare surface is 5 times stronger than that from the clean undoped Si and, in contrast with surface B-doped Si(001), the E_1 peak is *blueshifted* to its bulk energy. This signifies the bulk origin of the signal via EFISH generation in the depletion region [33]. H termination quenches and spectrally redshifts the SHG signal - again opposite to the behavior of surface B-doped Si(001) - because H passivates surface states responsible for Fermi level pinning [33], thus flattening the bands.

Surface B_2H_6 adsorption at RT, in contrast with both 600°C adsorption and bulk B doping, quenches surface SHG. This can be seen in the real time RT response at $2\hbar\omega = 3.3\,\mathrm{eV}$ shown in the inset of Fig. 5.8a. The $\sim 100\,\mathrm{s}$ rise time[†]reflects primarily the surface accumulation time of B_2H_6, which subsequently dissociates into BH_2 and H at Si dimer sites. Clearly the SHG response to second-layer substitutional B differs markedly from that of either bulk B or non-substitutional surface B_2H_6 dissociation products.

5.7 B/Si and H-B/Si SHG calculations

The calculation of optical spectra of semiconductor surfaces requires the development of accurate theories. First principles or *ab initio* methods are quiet accurate but they are limited in the number of atoms they can handle, in contrast with the SETB method which can handle many atoms, and thus has the advantage of being computationally faster.

[†] The rise time in this context is the time necessary to detect the SHG signal from the surface at saturation coverage.

However, both can be used simultaneously to learn about SHG. In this section, we use them to understand the experimental SHG response of clean and H-covered B/Si(100) surface as seen in Sec. 5.6.

First, we use the *ab initio* PP method of Ref. 46 to calculate the SHG spectra. Pseudopotentials for Si and H are generated by the Bachelet-Hamman-Schlütter (BHS) scheme [145] using the generalized gradient approximation (GGA). For B, a soft-core pseudopotential generated by the Troullier-Martins scheme is used [146]. Due to the quantum-size shift the GGA E_1 feature in the Si-slab occurs near 3.4 eV. Therefore no quasiparticle corrections are needed for PP generated band structure. The surface structure is modeled as a slab of eight atomic (100) layers. Total energy minimization, using an energy cutoff of $E_{cut} = 17\,\mathrm{Ry}$, yielded equilibrium atomic positions, according to the molecular dynamics method. For optical calculations up to $E_{cut} = 31\,\mathrm{Ry}$ are used. Although clean Si is well represented by a 2×1 unit cell [46], the B-doped surface reconstructs in multidomain c(4×4) [134] units. Computing the non-linear optical properties of such a big unit cell is at present prohibitively lengthy for *ab initio* methods. Thus the structural calculation is limited to a 2×1 unit cell also for B-doped surfaces, substituting one B for one second layer Si and two H per surface Si-Si dimer (monohydride) for H-B/Si (see. Fig. 5.7). *Ab initio* calculations for other Si-adsorbate systems showed that main SHG features were reproduced with this model as long as eigenfunctions were well converged [46]. In addition, using less computationally intensive SETB methods discussed below, larger unit cells calculations yield similar qualitative behavior [126].

Figure 5.9 shows calculated SHG intensity for clean, B-doped and H-B-doped Si(100)2×1 surface. For clean Si(100)2×1, the E_1 feature near 3.4 eV is evident. For B/Si a stronger, red-shifted peak at 3.3 eV appears, in agreement with experimental results, together with a second strong peak at 2.8 eV, beyond the experimental range. On H-B/Si, the former peak blue-shifts to 4.05 eV, the latter to 3.1 eV, and both strengthen. The qualitative behavior of the higher energy peak clearly mirrors the observed trends shown in Fig. 5.8. Quantitatively, the blueshift at H-B/Si is much stronger than observed. We believe the primary reason for this discrepancy is our use of a 2×1 cell with one B, which overestimates maximum θ_B by about a factor of 2. In fact, the surface monolayers from which SHG originates become alloyed at our modeled B and H concentrations, so that calculated peaks in Fig. 5.9 (in particular on H-B/Si) lose identity as Si E_1 and E_2. This situation can be remedied only with calculations based on larger unit cells. We also find that the blueshift at H-B/Si is sensitive to H concentration and bonding site. For

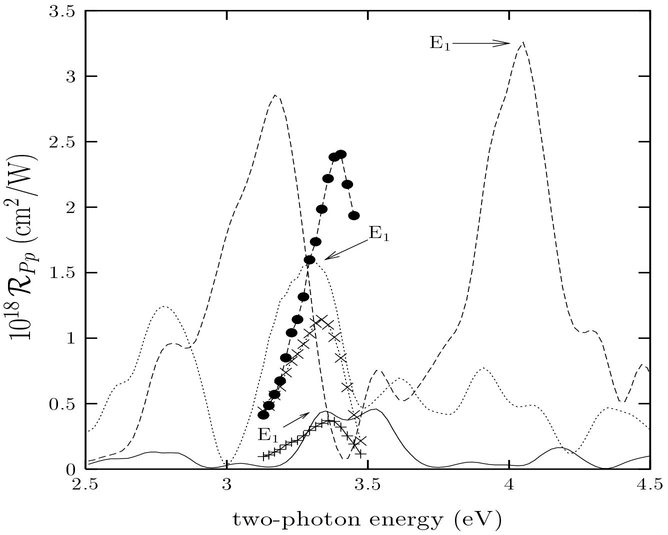

Figure 5.9: *Ab initio* calculations of reflected SHG intensity $\mathcal{R}_{Pp}$ for clean (solid line), B-doped (dotted line), and H-B-doped (dashed line) Si(001)2×1 surface. Arrows identify the E_1-like feature in each curve. The experimental spectra is also shown for comparison: the solid line with pluses is for the clean surface, the dotted line with crosses is for the B-doped surface and the dashed line with circles is for the H-B-doped surface.

example, using only 1 H per dimer, above either a Si or B back-bond, we calculate that the same peaks are less blue-shifted and broader. A mixture of such sites may be present experimentally.

The results presented in Fig. 5.9 describe the modifications of the SHG response in terms of chemical hybridization of surface bonds. These calculations make no explicit reference to the surface dc-electric field $E_z^{dc}(z)$ approaching 10^7 V/cm, which accompanies electron transfer from surface Si dimers to second layer B acceptors [131, 143]. Fields of this strength contribute to SHG in ways which are not completely included in the present PP calculations, since they significantly redistribute transition momentum (cf. Franz-Keldysh effect in linear optics) and induce higher-order SH polarization. A complete accounting of these effects requires calculation of SEFISH terms including both the *second*- and the *third*-order optical susceptibilities, χ_{ijk} and χ_{ijkz} respectively (first method described in Sec. 5.2). Nevertheless the results shown in Fig. 5.9 capture the main qualitative SHG trends observed for B/Si and H-B/Si.

In order to evaluate SEFISH contributions more explicitly, we performed an independent SETB calculation (second formalism described in Sec. 5.2) to calculate SHG spectra of a clean and H covered B/Si(100) surface. For the clean surface, B/Si, the

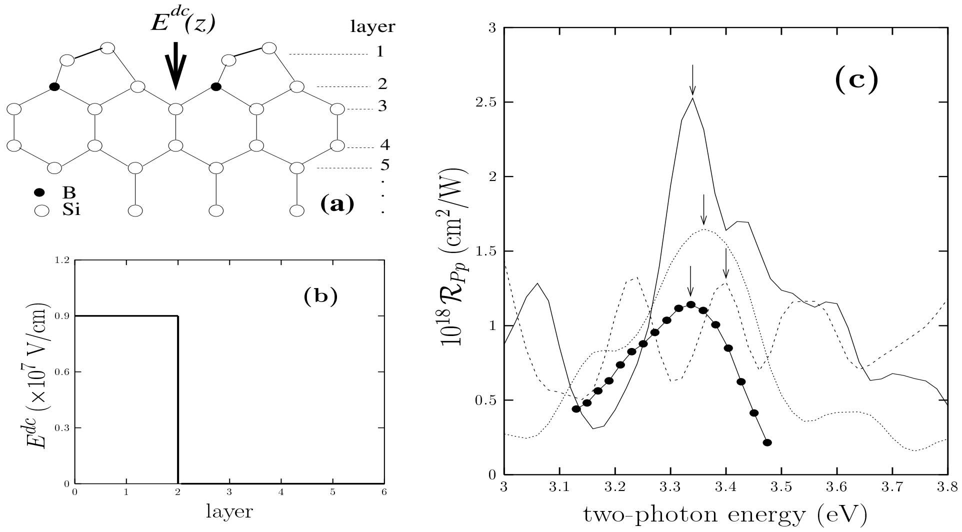

Figure 5.10: Panel (a) shows the equilibrium structures of the B/Si surface viewed along [110]. Open (solid) circles are Si (B) atoms. Panel (b) shows the profile of the surface field $E_z^{dc}(z)$ pointing towards bulk. In panel (c) we show the SETB calculations of $\mathcal{R}_{Pp}$ for clean ($E_z^{dc}(z) = 0$) Si(100)2×1 (dotted line), $E_z^{dc}(z)$ pointing towards the bulk (solid line), and towards the vacuum (dashed line). The second case corresponds to the B-doped surface. The solid circles are the experimental results of Fig. 5.8. The arrows show E_1.

electron transfer from surface Si dimers to second layer B acceptors [131] brings a surface dc-electric field $E_z^{dc}(z)$, that approaches 10^7 V/cm, and points into the bulk of the system (see Figs. 5.10a and 5.10b). On the other hand, according to *ab initio* structure calculations (see above), H termination of B-back-bonded Si dimers symmetrizes the surface dimer and quenches charge transfer to the second layer B, which should in turn quench the SEFISH polarization. Nevertheless, B can continue to act as a strong acceptor of electrons from the underlying bulk. Accompanied by redistribution of the space charge, this could create a dc-electric field opposite in direction, and deeper in spatial extent than the step dc-electric field that arises on the B/Si surface, as depicted in Figs. 5.11a and 5.11b. Its strength and spatial extent depends on band bending as determined by the relative energies of the acceptor states, which pin the surface Fermi level and the bulk Fermi level. Since TB parameters for the Si-B bond are not well-established, we treated B as a Si atom for the SETB calculations, while preserving atomic coordinates from the *ab initio* structure calculation.

As shown in Fig. 5.10c the SETB SHG spectrum for clean Si(100)2×1 clearly shows the E_1 peak. The calculated E_1 for B/Si, also shown in Fig. 5.10c, is for a $E_z^{dc}(z)$ directed inward with a step-function profile and magnitude of 0.9×10^7 V/cm terminating at the

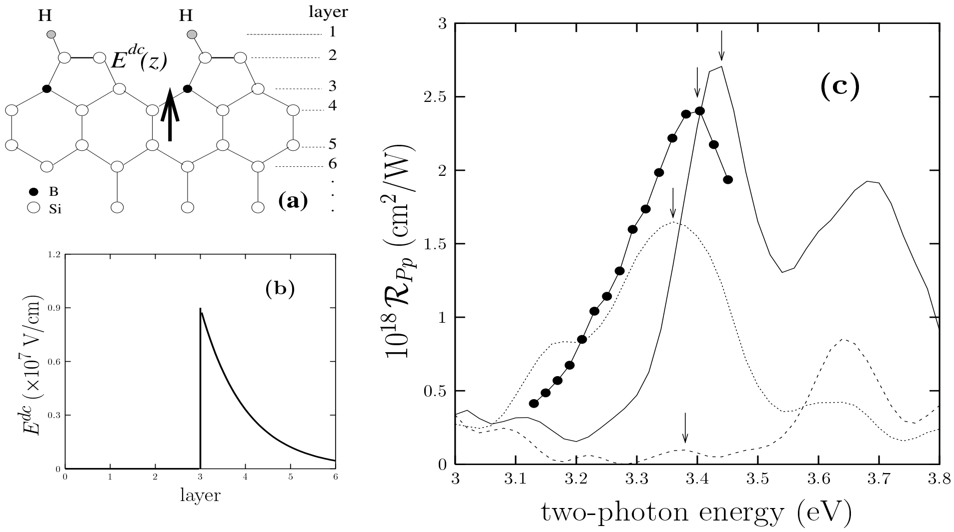

Figure 5.11: Panel (a) shows the equilibrium structures of H-B/Si viewed along [110]. Open (solid) circles are Si (B) atoms. Panel (b) shows the profile of the surface field $E_z^{dc}(z)$ pointing towards vacuum. In panel (c) we show the SETB calculations of $\mathcal{R}_{Pp}$ for clean ($E_z^{dc}(z) = 0$) Si(100)2×1 (dotted line), $E_z^{dc}(z)$ pointing towards the vacuum (solid line), and towards the bulk (dashed line). The second case corresponds to the H-B-doped surface. The solid circles are the experimental results of Fig. 5.8. The arrows show E_1.

second layer B (see Fig. 5.10b). We see that in this case E_1 is intensified and redshifted compared to the undoped surface, in qualitative agreement with the measured spectra shown in the same figure. Similar $E_z^{dc}(z)$ profiles yielded the same qualitative behavior; reversing the field direction changes the direction of the spectral shift and substantially alters the intensity and lineshape of the E_1 peak (see Sec. 5.4), as can be seen also in Fig. 5.10c.

As discussed above, for the case of H-B/Si(100), and to illustrate the sensitivity of the SHG to the field profile changes, we can anticipate field strength comparable to $E_z^{dc}(z)$ just beneath the second layer B. Indeed, our SETB SHG spectrum for this case shown in Fig. 5.11c, where we used a $E_z^{dc}(z)$ which starts abruptly at 0.9×10^7 V/cm from the third layer, and decays exponentially with z (see Figs. 5.11b), shows the E_1 peak blueshifted from the bulk E_1 energy and strengthened, in qualitative agreement with the experimental spectra shown in the same figure. The E_1 energy reflects the more bulk-like origin of the signal and a field-induced blueshift from the surface-directed $E_z^{dc}(z)$. As in the previous case, reversing the field direction changes the direction of the spectral shift and substantially alters the intensity and lineshape of the E_1 peak, as can be seen also in Fig. 5.11c.

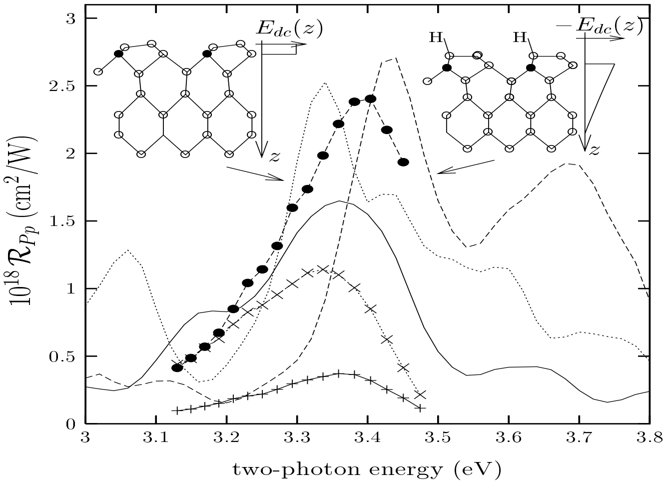

Figure 5.12: SETB calculations of $\mathcal{R}_{Pp}$ for clean (solid line), B-doped (dotted line), and H-B-doped (dashed line) Si(100)2 $\times$ 1. The corresponding experimental data is also shown: the solid line with pluses is for the clean surface, the dotted line with crosses is for the B-doped surface and the dashed line with circles is for the H-B-doped surface. The theoretical curves have been shifted upward by 0.48 eV for better comparison with experimental results. Insets: equilibrium structures viewed in the [110] direction. Open (solid) circles are Si (B) atoms. The surface field $E_z^{dc}(z)$ points towards bulk and vacuum, respectively, for B/Si (left) and H-B/Si (right).

We show in Fig. 5.12 the SHG spectra of Figs. 5.10c and 5.11c with the correct direction of $E_z^{dc}(z)$ along with the experimental data. The SETB SHG spectrum for clean Si(100)2 $\times$ 1 clearly shows the E_1 peak (solid curve). The calculated E_1 for B/Si (dotted curve), with $E_z^{dc}(z)$ directed inward with a step function terminating at the second layer (see Fig. 5.10b), is intensified and redshifted compared to the undoped surface. For the H-B/Si surface (dashed line) with a exponential decaying function for $E_z^{dc}(z)$ initiating at the third substitutional B layer (see Fig. 5.11b) and pointing towards vacuum, the E_1 resonance is more intensified and blueshifted compared to the undoped surface. This behavior is in qualitative agreement with the measured spectra of Fig. 5.8.

5.8 Conclusions

We have presented in this chapter a microscopic calculation of the effect of a surface dc-electric field on SHG for a clean and H-covered Si(100)c(4$\times$2) surface as well as for the B-doped Si(100)2$\times$1 and H-B-doped Si(100)2$\times$1 surface. The behavior of the surface allowed bulk E_1 peak is shown to have the correct experimental behavior as a function of the surface dc-electric field, strongly suggesting the presence of built in fields in the subsurface region. SHG spectroscopy yields direct signatures of charge transfer accompanying second layer B incorporation at Si(100) which have been microscopically modeled. SETB (second formalism) confirms the key role of near-surface electric fields, which could not be neglected as compared to the effect of the rehybridization of atomic bonds (first formalism). Our results shed light into the direction for further improvement of the theory by calculating the $\vec{E}^{dc}(z)$ from the actual charge density.

Chapter 6

Conclusions

In this thesis, we have studied the linear and mainly the non-linear optical response of Si surfaces through the techniques of reflectance anisotropy (RAS) and second harmonic generation (SHG). We have studied the clean and H-adsorbed Si(100) surface as well as the B-doped surface. We have used two approaches to obtain the optical spectra, the polarizable bond model and a microscopic formulation using the semi-empirical tight-binding (SETB) method and *ab initio* calculations. Our results obtained by these models show a good agreement with the experimental data available at present.

The model of polarizable bonds has been applied to study the surface RAS and SHG optical spectra of clean Si(100)2×1. It has been found that both RAS and SHG are very sensitive to the buckling and that in particular a surface with dimer buckling of 0.6 Å qualitatively reproduces most of the experimental features reported in the literature. By changing some of the parameters of the model, we concluded that the resonant structures in RAS and SHG are produced by the atomic reconstruction of the surface through the local field induced in the sub-surface region. Even though the model does not include the electronic surface states, the 1.5 eV surface peak is seen in RAS. However, the surface resonance at 3 eV in SHG is not observed. The spectra for a c(4×2) surface reconstruction have been also calculated and we found that this surface gives a good SHG E_1 resonance however, it does not give good agreement with RAS. The surface sensitivity shown by this model is such that, as a further extension of this work, one can refine the dimer geometry by varying structural parameters and by choosing a few frequencies, like E_1 and E_2, at which to fit the spectral features of RAS and SHG. However, this is beyond the scope of the present thesis. Finally within the polarizable bond model, we see that the 2×1

reconstruction of Si(100) yields a better agreement with experiment than the c(4×2) structure in contrast with the conclusion of the microscopic calculations of Ref. [45]. To make a direct comparison with the above theoretical results, we suggest that the same sample should be studied in RAS and SHG spectroscopic experiments.

On the other hand, we have also applied a microscopic formulation to analyze the different terms that contribute to the total non-linear susceptibility with which we calculate SHG. As an example, the Si(100)c(4×2) surface was analyzed. It has been shown that taking into account only the $\chi_{\parallel\parallel\perp}$ component of the susceptibility tensor in the calculation of SHG yields a spectrum that well resembles the experimental spectrum in the frequency range from 2 eV to 4 eV. Classifying the 1ω and 2ω contributions of $\chi_{\parallel\parallel\perp}$ into its surface or bulk character, we discussed the energy-space and $\vec{k}$-space features of the S_0, S_1, and E_1 resonances. From this analysis, we concluded the following.

The S_0 resonance comes from 1ω and 2ω surface-surface transitions across the gap, whose transitions are to surface virtual states in the conduction band, and it also comes from 2ω surface-bulk transitions across the gap, whose transitions are to virtual bulk states in the valence band. The transitions occur from the top to bottom Si of the dimer, however the transitions to virtual bulk states in the valence band that are part of the surface-bulk contribution, could be to subsurface atoms (see Fig. 4.14).

The S_1 resonance has its origin in 1ω surface-surface transitions across the gap, whose transitions are to virtual bulk states in the conduction band, and in 2ω bulk-surface transitions across the gap, whose virtual transitions are to virtual surface states in the valence band. The 1ω transitions are from the top to the bottom Si of the dimer, and the 2ω transitions are from a Si in the second plane to either the bottom Si of the dimer or a Si in the third plane just below the dimer rows (see Fig. 4.16).

The bulk E_1 resonance has more contributions than the previous two surface peaks, but only from 2ω transitions (see Fig. 4.18). They are given by, surface-bulk transitions across the gap whose transitions are into surface and bulk conduction virtual states, and bulk-bulk transitions across the gap whose transitions are into bulk conduction or valence virtual states. Since E_1 is a bulk resonance, it is important to remark that it is strongly affected by the surface, i.e. the E_1 transitions are among the bulk atoms and the lower atoms of the dimer. This fact also shows how the surface breaks the bulk inversion symmetry readily allowing dipolar SHG (see Fig. 4.18).

From our analysis it should be clear how the fine interplay of surface and bulk 1ω and 2ω transitions gives the observed SHG spectrum. Also, we emphasize that the bulk or surface nature of a electronic states does not imply that it belongs to a surface or bulk atom completely, rather that its wave function is distributed among surface, subsurface and bulk atoms. The influence of both surface and bulk clearly shows up in the different terms of the susceptibility that give the SHG spectra, which is a statement of the known fact that the surface states are bulk perturbed and vice versa.

We emphasize that the analysis to systematically investigate the different contributions of the non-linear susceptibility to the observed peaks in SHG might be applied for other surfaces. We remark that such analysis could be carried out using different approaches to calculate the one-electron energies and momentum matrix elements required for the evaluation of the non-linear susceptibility.

We have also applied the microscopic calculation of Chap. 4 to study the effect of a surface dc-electric field on SHG for Si(100) clean and H covered surfaces. On one hand, the adsorption of H on the clean surface was studied. The behavior of the surface allowed bulk E_1 peak is shown to have the correct experimental behavior as a function of the surface dc-electric field, strongly suggesting the presence of built in fields in the subsurface region. Also, the spectral differences as a function of $\vec{E}^{dc}$ make SHG a useful optical probe for it. We find a behavior of E_1 which would be very interesting to study experimentally in more detail.

On the other hand, adsorption of H and incorporation of B on Si surface was also studied. SHG spectroscopy yields direct signatures of charge transfer accompanying second layer B incorporation at Si(001) which have been microscopically modeled. SETB confirms the key role of near-surface electric fields, which could not be neglected as compared to the effect of the rehybridization of atomic bonds. Our results shed light into the direction for further improvement of the theory by calculating the $\vec{E}^{dc}(z)$ from the actual charge density, then incorporating its effect through a surface EFISH χ_{ijkl} (see Chap. 5).

From the above conclusions, we can understand within the approach of Chap. 4 some of the general features seen in SHG from this surface when it is covered by other species of atoms. For instance, as a function of H termination of the surface, the dimer first symmetrizes and then breaks, disrupting the dimer related states, and thus quenching the surface resonances (see Chap. 5). However the E_1 resonance, being less sensitive to the dimer as it involves transitions among subsurface atoms, does not disappear completely. This is the behavior seen in the experiments [31] and in the theoretical spectra [45]. On the other hand, B adsorption on this surface shows a very interesting behavior for the E_1 resonance (see. Chap. 5). Since B goes to second layer Si sites, its influence is not of quenching, but rather of redshifting the position of E_1 and of increasing its intensity, since it interacts with the subsurface atoms as well as the bottom Si of the dimer.

Experiments over a wider spectral range, and calculations based on more accurate structural units, will also improve quantitative interpretation of the spectroscopy. We mention that local-field and excitonic effects along with the surface screening will prove to be crucial for a quantitative comparison between theory and experiment.

Finally, we conclude that the optical techniques RAS and SHG are very versatile *surface sensitive* probes to analyze surfaces and interfaces, which offer unique advantages over other surface probes: they are coherent probes, they do not require ultra-high vacuum (UHV) environments, they are non-invasive, non-destructive and have wide spectral coverage as well.

Experimental and theoretical studies of surfaces by using optical techniques have been developed rapidly. This research has contributed significantly in the last years to understand the optical physical processes that take place at surfaces. This is very important for the development of new electronic devices. Currently, we are not yet able to apply this kind of techniques to control the quality of manufacture of surfaces for a device in a manufacture plant. However the rapid evolving research in this direction makes the optical techniques to be a promising tool [147].

The transistor revolutionized the electronics and has made possible to built novel devices. We expect, in the forthcoming years, that the optical techniques of RAS and SHG will allow surface science research to develop much more impressive and novel electronic devices.

Appendix A

Optical spectroscopy: potential applications

The following discussion has been taken from Ref. 147 and is intended to emphasize the potential that the optical spectroscopy has for controlling semiconductor epitaxial growth.

The drive towards higher performance and increasing complexity in semiconductor devices, together with the trend towards chemical beam deposition (CVD) methods such as organometallic CVD and chemical beam epitaxy, are providing strong incentives to develop a better understanding of growth processes and better methods of monitoring[*] growth. Real-time information about a growing crystal is useful for various reasons, including a posteriori diagnosis of failed devices. Much effort is presently being directed toward developing predictive approaches and to base process decisions on information about the growing sample itself, leading ultimately to sample-driven closed-loop feedback control[†] of epitaxy.

Optical probes are of interest for sample-driven applications because they are nondestructive, noninvasive, and can be used in any transparent ambient. Recent effort has gone into developing optical techniques sensitive to surface processes. Those that are relatively new include reflectance anisotropy spectroscopy (RAS), reflectance difference

---

[*] By monitoring we refer to the real-time determination of information about the process (ambient), sample surface, and/or the sample itself.

[†] By control we refer to the use of information about the process (ambient), sample surface, and/or the sample itself to make real-time decisions about modifications of growth or deposition parameters.

spectroscopy (RDS), laser light scattering (LLS) second harmonic generation generation (SHG). These techniques rely on symmetry to suppress the bulk response in favor of the surface component.

The parameters needed to characterize growth may be classified as follows: a) bulk parameters: layer thickness, compositions, and uniformities; b) surface-determined parameters: efficiency of dopant incorporation, possibility of atomic ordering of nominally random alloys. interface widths, etc. and c) tertiary parameters which are those related to the process itself, for example pressure, and flow rate of the carrier gas, the partial pressures of active species, temperature of the sample etc.

Our ability to use these parameters for control is predicated on our capability of obtaining information about them. Process-directed measurements include temperature determinations by thermocouples and ambient-composition determinations by laser induced fluorescence, infrared absorption spectroscopy, coherent anti-Stokes Raman scattering, ultraviolet absorption spectroscopy, and mass spectrometry. Surface information can be obtain by RAS, RDS, surface photoabsorption, LLS, SHG, and in ultra-high vacuum environments (UHV), reflection high energy electron diffraction (RHEED). Bulk probes include spectroreflectometry, spectroscopic ellipsometric, photoreflectance, and various imaging techniques.

Considerable progress has been made in the control of semiconductor epitaxy. However a number of challenges remain. A major challenge, particularly with respect to quaternary material such as $\mathrm{In}_x\mathrm{Ga}_{1-x}\mathrm{As}_{1-y}\mathrm{P}_y$, is to enhance signal-to-noise ratios to where anion as well as cation compositions can be determined, especially in actual reactors where samples are rotated for uniformity and mechanical vibration may occur as well.

Surface-optical spectra must also be interpreted to achieve a quantitative understanding of growth chemistry. The quartz-optics spectral range, about 1.5 to 6.0 eV, is severely limited. Without a suitable atlas of visible-near ultraviolet spectra of surface species it has been necessary to rely on the theoretical calculations. The task of calculating surface-optical spectra is difficult even in the linear approximation, and recent experiments suggest that non-local and many-body effects must be considered as well.

The biggest challenge will be to win acceptance of the theoretical approaches used to describe surface processes in production. The major objective of growth is the production of devices, and success is measured in new capabilities and improved yields. It is unlikely that the advances made so far, particularly any but the simplest, will be accepted until improved yields are demonstrated or devices that cannot currently be fabricated are produced. Although considerable progress has been made, much remain to be done before these techniques become viable production tools.

Appendix B

List of abbreviations

2DBZ	Two Dimensional Brillouin Zone
AES	Auger Electron Spectroscopy
B/Si	B-doped Si
CVD	Chemical Vapor Deposition
dc	Direct Current
DFG	Difference Frequency Generation
DFT	Density Functional Theory
DFT-LDA	Density Functional Theory within the Local Density Approximation
DRS	Differential Reflectance Spectroscopy
EFISH	Electric-field-induced Second Harmonic
HREELS	High-resolution Electron-energy-loss Spectroscopy
H-B/Si	H-adsorbed and B-doped Si
LDA	Local Density Approximation
LEED	Low Energy Electron Diffraction
LLS	Laser Light Scattering
ML	Monolayer
PP	Pseudopotential
RAS	Reflectance Anisotropy Spectroscopy
RDS	Reflectance Difference Spectroscopy
RT	Room Temperature
RHEED	Reflection High Energy Electron Diffraction
SETB	Semi-empirical Tight-binding

SDR	Surface Differential Reflectivity
SH	Second Harmonic
SHG	Second Harmonic Generation
SFG	Sum Frequency Generation
STM	Scanning Tunneling Microscopy
TB	Tight-Binding
TPD	Temperature Programmed Desorption
TDLDA	Time Dependent Local Density Approximation
UHV	Ultra-high Vacuum
XPS	X-ray Photoemission or Photoelectron Spectroscopy

Appendix C

List of symbols

a	Distance between crystal planes
a_o	Lattice constant
$\vec{A}$	Vector potential
A	Area
a_B	Bohr Radius
$\overset{\leftrightarrow}{\alpha}$	Linear polarizability tensor
$\alpha_{\parallel}$	Parallel component of the linear polarizability
$\alpha_{\perp}$	Perpendicular component of the linear polarizability
c	Speed of light
d	Layer thickness
$\vec{D}$	Displacement electric field
$\delta(z)$	Dirac's delta
$\Delta\epsilon$	Perturbation to the dielectric function
ΔR	Difference in reflectance of light
ΔR_x	Reflectance of light polarized along x
ΔR_y	Reflectance of light polarized along y
e	Electron charge
$\hat{e}$	Unitary vector
$\vec{E}$	Electromagnetic field vector
$\vec{\mathcal{E}}$	Local field
$\vec{E}(A,\omega)$	External electric field
$\vec{E}(B,\omega)$	Electric field inside the medium
$\vec{E}^{ext}$	External field

$\vec{E}^{dc}$	Surface dc-electric field
E_z^{dc}	z component of the surface dc-electric field
E_{at}	Atomic electric field
E_n	Energy
E_{nr}	Difference of energy between the states E_n and E_r
E_0	Magnitude of the surface dc-electric field
ϵ	Dielectric function
ϵ_s	Surface dielectric function
ϵ_b	Bulk dielectric function
$\hat{\mathcal{H}}_0$	Unperturbed Hamiltonian
I	Intensity of light
$\hat{\vec{J}}$	Induced current operator
$\vec{k}$	Wave vector
L_{eff}	Effective depth
λ	Wave length
m	Electron mass
$\overset{\leftrightarrow}{M}$	Dipolar interaction tensor of second rank
n_0	Electron density
$\overset{\leftrightarrow}{N}$	Dipolar interaction tensor of third rank
ω	Frequency
ω_c	Damping frequency
ω_p	Plasma frequency
$\omega_{\parallel}$	Frequency corresponding to the parallel response
$\omega_{\perp}$	Frequency corresponding to the perpendicular response
$\vec{p}(\omega)$	First order induced dipole moment
$\vec{p}(2\omega)$	Second-order induced dipole moment
$\hat{\vec{p}}$	Momentum operator
$\vec{P}$	Polarization
P^{tot}	Total polarization
$\vec{\mathcal{P}}$	Modified momentum operator
$\vec{\mathsf{P}}$	Dipole moment per unit volume
$\vec{P}_b$	Bulk polarization
$\vec{P}(B,\omega)$	Bulk polarization
$\vec{P}_{eff}$	Effective polarization
P_{sn}^{i}	Matrix element of the i-component of the momentum operator between states s and n

$\psi^{(n)}$	Wave function of order n
$\psi^{(0)}$	Ground state wave function
ϕ	Tight-binding wave function
$\hat{\varphi}$	Potential energy
$\overleftrightarrow{Q}$	Second-order induced quadrupole moment
$\overleftrightarrow{\mathcal{Q}}$	Electric quadrupolar polarization
$\vec{r}$	Position
$\mathcal{R}$	Second harmonic generation efficiency
R_0	Fresnel reflection coefficient
$\vec{S}$	Non-linear source
σ	Surface charge density
t	Time
T_i	Transmission Fresnel factor for light with i polarization
θ	Angle of incidence
V	Perturbing potential
W	Weight
X	Second-order nonlinear susceptibility for a single domain surface
$\overleftrightarrow{\chi}$	Second-order nonlinear susceptibility tensor
$\overleftrightarrow{\chi}^{(d)}$	Dipolar microscopic second-order susceptibility tensor
$\overleftrightarrow{\chi}^{eff}$	Effective non-linear susceptibility
$\overleftrightarrow{\chi}^{(m)}$	Magnetic microscopic second-order susceptibility tensor
$\overleftrightarrow{\chi}^{(Q)}$	Quadrupolar microscopic second-order susceptibility tensor
$z_{nn'}$	Intra-atomic matrix elements for the atomic z-coordinate

Appendix D

Publication list

Part of the research of this thesis is published in the following articles:

1. N. Arzate, J.E. Mejía, Bernardo S. Mendoza and Rodolfo del Sole, *D.C.-electric-field modified second-harmonic-generation at the Si(100)*, Appl. Phys. B, **68**, 629-632 (1999). DOI: 10.1007/s003400050676
2. D. Lim, M. C. Downer, J. G. Ekerdt, N. Arzate, Bernardo S. Mendoza, V. I. Gavrilenko and R. Q. Wu, *Optical second harmonic spectroscopy of boron-reconstructed Si(001)*, Phys. Rev. Lett. **84**, 3406 (2000). DOI: 10.1103/PhysRevLett.84.3406
3. N. Arzate and Bernardo S. Mendoza, *Polarizable bond model for optical spectra of Si(100) reconstructed surfaces*, Phys. Rev. B **63**, 113303-1 113303-4 (2001). DOI: 10.1103/PhysRevB.63.113303
4. N. Arzate and Bernardo S. Mendoza, *Microscopic study of surface second harmonic generation from a clean Si(100)c4×2 surface*, Phys. Rev. B **63**, 125303 (2001). DOI: 10.1103/PhysRevB.63.125303
5. N. Arzate and Bernardo S. Mendoza, *Surface dc-electric field modified second-harmonic-generation at the B and H-covered Si(100)2×1 surface*, J. Optical Technology, **69**, 380-384 (2002). DOI: 10.1364/JOT.69.000380
6. N. Arzate and B. S. Mendoza, *Polarizable bond model for reflectance anisotropy and second harmonic generation for Si(100) surfaces*, Proceedings of the 19th Course

of the International School of Solid State Physics, Epioptics 2000, The Science and Culture, Series Materials Science, Editor: Antonio Cricenti, 18-23 (2001).

Bibliography

[1] M. Riordan and L. Hoddeson, *Birth of an era*, Scientific American **8**(1), 10 (1997).

[2] F. H. Rockett, *The transistor*, Scientific American **8**(1), 19 (1997).

[3] H. I. Smith and H. G. Craighead, *Nanofabrication*, Physics Today p. 24 (February 1990).

[4] M. H. Brodsky, *Progress in gallium arsenide semiconductors*, Scientific American p. 56 (February 1990).

[5] G. Burns, *Solid State Physics* (Academic Press, Inc., 1985).

[6] W. L. Mochán and R. G. Barrera, *Intrinsic surface-induced optical anisotropies of cubic crystals: Local-field effect*, Phys. Rev. Lett. **55**(11), 1192 (1985).

[7] C. M. J. Wijers, P. L. de Boeij, C. W. van Hasselt, and T. Rasing, *Effect of linear polarizability and local fields on surface SHG*, Solid State Commun. **93**(1), 17 (1995).

[8] B. S. Mendoza and W. L. Mochán, *Polarizable-bond model for second-harmonic generation*, Phys. Rev. B **55**(4), 2489 (1997).

[9] B. S. Mendoza, R. Del Sole, and A. I. Shkrebtii, *Theory of optical reflectance anisotropy of the natural Si(110) surface*, Phys. Rev. B **57**(20), R12709 (1998).

[10] C. D. Hogan and C. H. Patterson, *Reflectance anisotropy of silicon surfaces: Discrete dipole calculation*, Phys. Rev. B **57**(23), 14843 (1998).

[11] M. Palummo, G. Onida, R. Del Sole, and B. S. Mendoza, *Ab initio optical properties of Si(100)*, Phys. Rev. B **60**(4), 2522 (1999).

[12] M. Rohlfing and S. G. Louie, *Excitons and optical spectrum of the Si(111)-(2×1)*, Phys. Rev. Lett. **83**(4), 856 (1999).

[13] J. D. E. McIntyre and D. E. Aspnes, *Differential reflection spectroscopy of very thin surface films*, Surf. Sci. **24**, 417 (1971).

[14] P. A. Franken, A. E. Hill, C. W. Peters, and G. Weinreich, *Generation of optical harmonics*, Phys. Rev. Lett. **7**(4), 118 (1961).

[15] R. W. Terhune, P. D. Marker, and C. M. Savage, *Optical harmonic generation in calcite*, Phys. Rev. Lett. **8**(10), 404 (1962).

[16] Y. R. Shen, *Surface properties probed by second-harmonic and sum-frequency generation*, Nature **337**, 519 (1989).

[17] Y. R. Shen, *Wave mixing spectroscopy for surface studies*, Solid State Commun. **102**, 221 (1997).

[18] P. Guyot-Sionnest, W. Chen, and Y. R. Shen, *General considerations on optical second-harmonic generation from surfaces and interfaces*, Phys. Rev. B **33**(12), 8254 (1986).

[19] T. F. Heinz, C. K. Chen, D. Ricard, and Y. R. Shen, *Spectroscopy of molecular monolayers by resonant second-harmonic generation*, Phys. Rev. Lett. **48**(7), 478 (1982).

[20] P. Guyot-Sionnest and Y. R. Shen, *Bulk contribution in surface second-harmonic generation*, Phys. Rev. B **38**(12), 7985 (1988).

[21] K. van Hasselt, *Nonlinear and linear optical studies of Si-SiO$_2$ interfaces*, Ph.D. thesis, Katholieke Universiteit Nijmegen (1997), contains a nice and comprehensive list of references for this field.

[22] Y. R. Shen, *Surface contribution versus bulk contribution in surface nonlinear optical spectroscopy*, Appl. Phys. B **68**, 295 (1999).

[23] J. R. Power, J. D. O'Mahony, S. Chandola, and J. F. McGilp, *Resonant optical second harmonic generation at the steps vicinal Si(001)*, Phys. Rev. Lett. **75**(6), 1138 (1995).

[24] B. S. Mendoza and W. L. Mochán, *Local-field effect in the second-harmonic-generation spectra of Si surfaces*, Phys. Rev. B **53**(16), R10473 (1996).

[25] N. Bloembergen, R. K. Chang, S. S. Jha, and C. H. Lee, *Optical second harmonic generation in reflection from media with inversion symmetry*, Phys. Rev. **174**(3), 813 (1968).

[26] A. Janner, *Second-harmonic generation, a selective probe for excitons*, Ph.D. thesis, Wiskunde en Natuurwetenschappen aan de Rijksuniversiteit Groningen (1998).

[27] H. A. Wierenga, *Magnetization induced optical second-harmonic generation on magnetic multilayers*, Ph.D. thesis, Katholieke Universiteit Nijmegen (1995).

[28] G. Lüpke, D. J. Bottomley, and H. M. van Driel, *SiO_2/Si interfacial structure on vicinal Si(100) studied with second-harmonic generation*, Phys. Rev. B **47**(16), 33 (1993).

[29] W. Daum, H.-J. Krause, U. Reichel, and H. Ibach, *Nonlinear optical spectroscopy at silicon interfaces*, Physica Scripta **T49**, 513 (1993).

[30] W. Daum, H.-J. Krause, U. Reichel, and H. Ibach, *Identification of strained silicon layers at Si-SiO_2 interfaces and clean Si surfaces by nonlinear optical spectroscopy*, Phys. Rev. Lett. **71**(8), 1234 (1993).

[31] J. I. Dadap, Z. Xu, X. F. Hu, M. C. Downer, N. M. Russell, J. G. Ekerdt, and O. A. Aksipetrov, *Second-harmonic spectroscopy of a Si(100) surface during calibrated variations in temperature and hydrogen coverage*, Phys. Rev. B **56**(20), 13367 (1997).

[32] U. Höfer, *Nonlinear optical investigations of the dynamics of hydrogen interaction with silicon surfaces*, Appl. Phys. A **A 63**, 533 (1996).

[33] Z. Xu, X. F. Hu, D. Lim, J. G. Ekerdt, and M. C. Downer, *Second harmonic spectroscopy of Si(001) surfaces: Sensitivity to surface hydrogen and doping, and applications to kinetic measurements*, J. Vac. Sci. Technol. B **15**(4), 1059 (1997).

[34] D. Lim, M. C. Downer, J. G. Ekerdt, N. Arzate, B. S. Mendoza, V. I. Gavrilenko, and R. Wu, *Optical second harmonic spectroscopy of boron-reconstructed Si(001)*, Phys. Rev. Lett. **84**(15), 3406 (2000).

[35] N. Bloembergen and P. S. Pershan, *Light waves at the boundary of nonlinear media*, Phys. Rev. **128**, 606 (1962).

[36] O. A. Aksipetrov, I. M. Baranova, and Y. A. Il'inskiĭ, *Surface contribution to the generation of reflected second-harmonic light for centrosymmetric semiconductors*, Sov. Phys. JETP **64**(1), 167 (1986).

[37] J. E. Sipe, D. J. Moss, and H. M. van Driel, *Phenomenological theory of optical second- and third-harmonic generation from cubic centrosymmetric crystals*, Phys. Rev. B **35**(3), 1129 (1987).

[38] V. Mizrahi and J. E. Sipe, *Phenomenological treatment of surface second-harmonic generation*, J. Opt. Soc. Am. B **5**(3), 660 (1988).

[39] W. L. Schaich and B. S. Mendoza, *Simple model of second-harmonic generation*, Phys. Rev. B **45**(24), 14279 (1992).

[40] W. L. Mochán and B. Mendoza, *Second harmonic generation at crystal surfaces*, J. Phys. Condens. Matter **5**, A183 (1993).

[41] M. Cini, R. Del Sole, and L. Reining, *Theory of second-harmonic generation at semiconductor surfaces*, Surf. Sci. **287-288**, 693 (1993).

[42] L. Reining, R. Del Sole, M. Cini, and J. G. Ping, *Microscopic calculation of second-harmonic generation at semiconductor surfaces: As/Si(111) as a test case*, Phys. Rev. B **50**(12), 8411 (1994).

[43] V. I. Gavrilenko and F. Rebentrost, *Nonlinear optical susceptibility of the (111) and (001) surfaces of silicon*, Appl. Phys. A **60**, 143 (1995).

[44] V. I. Gavrilenko and F. Rebentrost, *Nonlinear optical susceptibility of the surfaces of silicon and diamond*, Surf. Sci. **331-333**, 1355 (1995).

[45] B. S. Mendoza, A. Gaggiotti, and R. Del Sole, *Microscopic theory of second harmonic generation at Si(100) surfaces*, Phys. Rev. Lett. **81**(17), 3781 (1998).

[46] V. I. Gavrilenko, *Optical second harmonic spectra of silicon-adatom surfaces: theory and experiment*, Thin Solid. Films **1-5**, 364 (2000).

[47] B. S. Mendoza, M. Palummo, G. Onida and R. Del Sole, *Ab initio calculation of second-harmonic-generation at the Si(100) surface*, submitted to Phys. Rev. Lett. (2000).

[48] J. Rudnick and E. A. Stern, *Second harmonic radiation from metal surfaces*, Phys. Rev. B **4**(12), 4274 (1971).

[49] J. E. Sipe, V. C. Y. So, M. Fukui, and G. I. Stegeman, *Analysis of second harmonic generation at metal surfaces*, Phys. Rev. B **21**(10), 4389 (1980).

[50] O. Keller, *Theoretical study of the nonlinear response function describing optical second-harmonic generation in nonlocal metal optics*, Phys. Rev. B **31**(8), 5028 (1985).

[51] M. Corvi and W. L. Schaich, *Hydrodynamic-model calculation of second-harmonic generation at a metal surface*, Phys. Rev. B **33**(6), 3688 (1986).

[52] W. L. Schaich and A. Liebsch, *Nonretarded hydrodynamic-model calculation of second harmonic generation at a metal surface*, Phys. Rev. B **37**(11), 6187 (1988).

[53] J. A. Maytorena, W. L. Mochán, and B. S. Mendoza, *Hydrodynamic model for second-harmonic generation at conductor surfaces with continuous profiles*, Phys. Rev. B **51**(4), 2556 (1995).

[54] J. A. Maytorena, W. L. Mochán, and B. S. Mendoza, *Hydrodynamic model for second-harmonic generation at metal surfaces*, SPIE **2730**, 376 (1996).

[55] J. A. Maytorena, B. S. Mendoza, and W. L. Mochán, *Theory of surface sum frequency generation spectroscopy*, Phys. Rev. B **57**(4), 2569 (1998).

[56] J. A. Maytorena, W. L. Mochán, and B. S. Mendoza, *Hydrodynamic model for sum and difference frequency generation at metal surfaces*, Phys. Rev. B **57**(4), 2580 (1998).

[57] B. S. Mendoza, W. L. Mochán, and J. A. Maytorena, *Visible-infrared sum and difference frequency generation at adsorbate-covered au*, Phys. Rev. B **60**(20), 14334 (1999).

[58] M. Weber and A. Liebsch, *Density-functional approach to second-harmonic generation at metal surfaces*, Phys. Rev. B **35**(14), 7411 (1987).

[59] A. Liebsch, *Second-harmonic generation at simple metal surfaces*, Phys. Rev. Lett. **61**(10), 1233 (1988).

[60] A. Liebsch and W. L. Schaich, *Second-harmonic generation at simple metal surfaces*, Phys. Rev. B **40**(8), 5401 (1989).

[61] A. Liebsch, *Electronic excitations at metal surfaces* (Plenum, 1996), 1st ed.

[62] A. Liebsch, *Theory of sum frequency generation from metal surfaces*, Appl. Phys. B **68**, 301 (1999).

[63] B. S. Mendoza, *A theoretical model for second-harmonic generation in silicon*, J. Phys. Condens. Matter **5**, A181 (1993).

[64] Z. H. Levine, *One-electron formalism for second-harmonic generation in crystalline semiconductors*, Phys. Rev. B **42**(6), 3567 (1990).

[65] J. E. Sipe and E. Ghahramani, *Nonlinear optical response of semiconductors in the independent-particle approximation*, Phys. Rev. B **48**(16), 11705 (1993).

[66] M. Cini, *Simple model of electric dipole second-harmonic generation from interfaces*, Phys. Rev. B **43**(6), 4792 (1991).

[67] T. Yasuda, L. Mantese, U. Rossow, and D. E. Aspnes, *Surface-induce optical anisotropies of single-domain* (2×1) *reconstructed (001) Si and Ge surfaces*, Phys. Rev. Lett. **74**(17), 3431 (1995).

[68] R. Shioda and J. van der Weide, *Reflectance difference spectroscopy of highly oriented (2×1) reconstructed Si(100) surfaces*, Phys. Rev. B **57**(12), R6823 (1998).

[69] J. F. McGilp, M. Cavanagh, J. R. Power, and J. D. OMahony, *Spectroscopic optical second-harmonic generation from semiconductor interfaces*, Appl. Phys. A **A 59**, 401 (1994).

[70] C. Meyer, G. Lüpke, U. Emmerichs, F. Wolter, H. Kurz, C. H. Bjorkman, and G. Lucovsky, *Electronic transitions at Si(111)/*SiO_2 *and Si(111)/*Si_3N_4 *interfaces studied by optical second-harmonic spectroscopy*, Phys. Rev. Lett. **74**(15), 3001 (1995).

[71] K. Pedersen and P. Morgen, Surf. Sci. **377-379**, 393 (1997).

[72] P. Godefroy, W. de Jong, C. W. van Hasselt, M. A. C. Devillers, and T. Rasing, *Electric field induced second harmonic generation spectroscopy on a metal-oxide-silicon structure*, Appl. Phys. Lett. **68**(14), 1981 (1996).

[73] G. Lüpke, *Characterization of semiconductor interfaces by second-harmonic generation*, Surface Science Reports **35**, 75 (1999).

[74] Y. R. Shen, *The principles of nonlinear optics* (John Wiley & Sons, 1984).

[75] J. D. Jackson, *Classical electrodynamics* (John Wiley & Sons, 1975), 2nd ed.

[76] R. Del Sole, in P. Halevi, ed., *Photonics Probes of Surfaces* (Elsevier Science, 1995), p. 131.

[77] R. Del Sole and E. Fiorino, *Macroscopic dielectric tensor at crystal surfaces*, Phys. Rev. B **29**(8), 4631 (1984).

[78] W. L. Mochán and R. G. Barrera, *Local-field effect on the surface conductivity of adsorbed overlayers*, Phys. Rev. Lett. **56**(20), 2221 (1986).

[79] N. Arzate and Bernardo S. Mendoza, *Polarizable bond model for optical spectra of Si(100) reconstructed surfaces*, Phys. Rev. B in press (2001).

[80] F. W. de Wette and G. E. Schacher, *Internal field in general dipole lattices*, Phys. Rev. **137**(1A), A78 (1965).

[81] A. Ramstad, G. Brocks, and P. J. Kelly, *Theoretical study of the Si(100) surface reconstruction*, Phys. Rev. B **51**(20), 14504 (1995).

[82] J. A. Appelbaum and D. R. Hamman, *Theory of reconstruction induced subsurface strain application to Si(100)*, Surf. Sci. **74**, 21 (1978).

[83] D. J. Chadi, *Atomic and electronic structures of reconstructed Si(100) surfaces*, Phys. Rev. Lett. **43**(1), 43 (1979).

[84] A. I. Shkrebtii and R. Del Sole, *Microscopic calculation of the optical properties of Si(100)*2×1*: Symmetric versus asymmetric dimers*, Phys. Rev. Lett. **70**(17), 2645 (1993).

[85] D. E. Aspnes and A. A. Studna, *Dielectric functions and optical parameters of Si, Ge, GaP, GaAs, GaSb, InP, InAs, and InSb from 1.5 to 6.0 eV*, Phys. Rev. B **27**(2), 985 (1983).

[86] C. E. Moore, *Atomic Energy Levels* (NBS, Washington, 1970).

[87] W. Hanke and L. J. Sham, *Many-particle effects in the optical spectrum of a semiconductor*, Phys. Rev. B **21**(10), 4656 (1980).

[88] E. Fiorino and R. Del Sole, *Some remarks on the theory of the dielectric response of crystals and on the lorentz-lorenz formula*, Phys. Status Solidi B **119**, 315 (1983).

[89] R. M. Tromp, R. G. Smeenk, F. W. Saris, and D. J. Chadi, *Ion beam crystallography of silicon surfaces II. Si(100)-(*2×1*)*, Surf. Sci. **133**, 137 (1983).

[90] S. G. Jaloviar, Jia-Ling, F. Liu, V. Zielasek, L. McCaughan, and M. C. Lagally, *Step-induced optical anisotropy of vicinal Si(001)*, Phys. Rev. Lett. **82**(4), 791 (1999).

[91] B. S. Mendoza, A. Gaggiotti, and R. Del Sole, *Microscopic theory of second harmonic generation at the Si(100)2×1 surface*, Phys. Stat. Sol. (a) **170**(2), 343 (1998).

[92] A. Guerrero and B. S. Mendoza, *Model for great enhancement of second-harmonic generation in quantum dots*, J. Opt. Soc. Am. B **12**(4), 559 (1995).

[93] J. Cruz-Mandujano and B. S. Mendoza, *Disorder effects on second-harmonic generation from one-dimensional arrays of polarizable units*, Phys. Rev. B **62**(12), 8438 (2000).

[94] N. Arzate and Bernardo S. Mendoza, *Microscopic study of surface second harmonic generation from a clean Si(100)c*4×2 *surface*, Phys. Rev. B. in press (2001).

[95] M.-Z. Huang and W. Y. Ching, *Calculation of optical excitations in cubic semiconductors. ii. Second-harmonic generation*, Phys. Rev. B **47**(15), 9464 (1993).

[96] A. I. Shkrebtii, R. D. Felice, C. M. Bertoni, and R. Del Sole, *Ab initio study of structure and dynamics of the Si(100) surface*, Phys. Rev. B **51**(16), 11201 (1995).

[97] J. C. Slater and G. F. Koster, *Simplified LCAO method for the periodic potential problem*, Phys. Rev. **94**(6), 1498 (1954).

[98] Neil W. Ashcroft and N. David Mermin, *Solid State Physics* (Saunders College, 1976).

[99] T. J. Lenosky, J. D. Kress, I. Kwon, A. F. Voter, B. Edwards, D. F. Richards, S. Jang, and J. B. Adams, *Highly optimized tight-binding model of silicon*, Phys. Rev. B **55**(3), 1528 (1997).

[100] P. Vogl, H. P. Hjalmarson, and J. D. Dow, *A semi-empirical tight-binding theory of the electronic structure of semiconductors*, J. Phys. Chem. Solids **44**(5), 365 (1983).

[101] J.-M. Jancu, R. Scholz, F. Beltram, and F. Bassani, *Empirical spds tight-binding calculation for cubic semiconductors: General method and material parameters*, Phys. Rev. B **57**(11), 6493 (1998).

[102] J. R. Power, P. Weightman, S. Bose, A. I. Shkrebtii, and R. Del Sole, *Sensitivity of reflectance anisotropy spectroscopy to the orientation of Ge dimers on vicinal Si(001)*, Phys. Rev. Lett. **80**(14), 3133 (1998).

[103] C. Noguez, C. Beitia, W. Preyss, A. I. Shkrebtii, M. Roy, Y. Borensztein, and R. Del Sole, *Theoretical and experimental optical spectroscopy study of hydrogen adsorption at Si(111)-(7×7)*, Phys. Rev. Lett. **76**(26), 4923 (1996).

[104] L. Mantese, private communication.

[105] L. D. Landau and M. Lifshitz, *Quantum Mechanics* (Pergamon Press., 1977), 3rd ed.

[106] A. Bagchi and R. G. Barrera and A. K. Rajagopal, *Perturbative approach to the calculation of the electric field near a metal surface*, Phys. Rev. B **20**(12), 4824 (1979).

[107] R. R. Schlicher and W. Becker and J. Bergou and M. O. Scully, *in Quantum Electrodynamics and Quantum Optics*, edited by A. O. Barut (Plenum, New York, 1984) See. Eqs. (2.17)-(2.20).

[108] F. Manghi, R. Del Sole, A. Selloni, and E. Mollinari, *Anisotropy of surface optical properties from first-principles calculations*, Phys. Rev. B **41**(14), 9935 (1990).

[109] J. E. Northrup, *Electronic structure of Si(100)c(4×2) calculated within the GW approximation*, Phys. Rev. B **47**(15), 10032 (1993).

[110] A. Selloni, P. Marsella, and R. Del Sole, *Microscopy calculation of the surface contribution to the optical reflectivity: Application to Si*, Phys. Rev. B **33**(12), 8885 (1986).

[111] S. Scandolo and F. Bassani, *Kramers-Kronig relations and sum rules for the second-harmonic susceptibility*, Phys. Rev. B **51**(11), 6925 (1995).

[112] C. Noguez, A. I. Shkrebtii, and R. Del Sole, Surf. Sci. **318**, 342 (1994).

[113] J. E. Mejía *et al*, unpublished.

[114] Laref *et al.*, Phys. Status Solidi B **208**, 413 (1998).

[115] T. Dumitrică, J. S. Graves, and R. E. Allen, *Second-order susceptibility from a tight-binding hamiltonian*, Phys. Rev. B **58**(23), 15340 (1998).

[116] C. Aversa and J. E. Sipe, *Nonlinear optical susceptibilities of semiconductors: Results with a length-gauge analysis*, Phys. Rev. B **52**(20), 14636 (1995).

[117] U. Höfer, L. Li, and T. F. Heinz, *Desorption of hydrogen from Si(100)2×1 at low coverages: The influence of π-bonded dimers on the kinetics*, Phys. Rev. B **45**(16), 9485 (1992).

[118] X. F. Hu, Z. Xu, D. Lim, M. C. Downer, P. S. Parkinson, B. Gong, G. Hess, and J. G. Ekerdt, In situ *optical second-harmonic-generation monitoring of disiline adsorption and hydrogen desorption durig epitaxial growth on Si(001)*, Appl. Phys. Lett. **71**(10), 1376 (1997).

[119] E. J. Buehler and J. J. Boland, *Identification and characterization of a novel silicon hydride species on the Si(100) surface*, Surf. Sci. **425**, L363 (1999).

[120] Z. Jing and J. L. Whitten, *Ab initio studies of H chemisorption on Si(100)*, Phys. Rev. B **46**(15), 9544 (1992).

[121] C. Noguez, J. Song, S. E. Ulloa, D. A. Drabold, and S. H. Yang, *Size dependence of the optical properties of silicon clusters*, Superlattices and Microstructures **20**(1), 1 (1996).

[122] S. Hong and M. Y. Chou, *Effect of hydrogen on the surface-energy anisotropy of diamond and silicon*, Phys. Rev. B **57**(11), 6262 (1998).

[123] U. Hansen and P. Vogl, *Hydrogen passivation of silicon surfaces: A classical molecular-dynamics study*, Phys. Rev. B **57**(20), 13295 (1998).

[124] J. J. Boland, *Structure of the H-saturated Si(100) surface*, Phys. Rev. Lett. **65**(26), 3325 (1990).

[125] J. I. Dadap, X. F. Hu, M. H. Anderson, M. C. Downer, J. K. Lowell, and O. A. Aktsipetrov, *Optical second-harmonic electroreflectance spectroscopy of a Si(001) metal-oxide-semiconductor structure*, Phys. Rev. B **53**(12), R7607 (1996).

[126] N. Arzate, J. E. Mejía, B. S. Mendoza, and R. Del Sole, *DC-electric-field-modified second-harmonic generation at the Si(100) surface*, Appl. Phys. B **68**(3), 629 (1999).

[127] N. Arzate and Bernardo S. Mendoza, *Surface dc-electric field modified second-harmonic-generation at the B and H-covered Si(100)2×1 surface*, Optical Journal (Opticheski Zhurnal) in press (2001).

[128] Bernardo S. Mendoza, private communication.

[129] R. L. Headrick, I. K. Robinson, E. Vlieg, and L. C. Feldman, *Structure determination of the Si(111):B*$(\sqrt{3} \times \sqrt{3})R30^o$ *surface: Subsurface substitutional doping*, Phys. Rev. Lett. **63**(12), 1253 (1989).

[130] H. Huang and S. Y. Tong and J. Quinn and F. Jona, *Atomic structure of Si(111)* $(\sqrt{3}\times\sqrt{3})R30^o$*-B by dynamical low-energy electron diffraction*, Phys. Rev. B **41**(5), 3276 (1990).

[131] Y. Wang, R. J. Hamers, and E. Kaxiras, *Atomic structure and bonding of boron-induced reconstructions on Si(001)*, Phys. Rev. Lett. **74**(3), 403 (1995).

[132] A. V. Zotov, M. A. Kulakov, B. Bullemer, and I. Eisele, *Scanning tunneling microscopy study of Si growth on a Si(111)*$\sqrt{3}\times\sqrt{3}-B$ *surface*, Phys. Rev. B **53**(19), 12902 (1996).

[133] P. Baumgärtel, J. J. Paggel, M. Hasselblatt, K. Horn, V. Fernández, O. Schaff, J. H. Weaver, A. M. Bradshaw, D. P. Woodruff, E. Rotenberg, *et al.*, *Structure determination of the* $(\sqrt{3} \times \sqrt{3})R30^o$ *boron phase on the Si(111) surface using photoelectron diffraction*, Phys. Rev. B **59**(20), 13014 (1999).

[134] J. Fritsch, J. B. Page, K. E. Schmidt, and G. B. Adams, *First-principles local-orbital study of the boron-induced reconstruction of Si(001)*, Phys. Rev. B **57**(16), 9745 (1998).

[135] S. Wang, M. W. Radny, and P. V. Smith, Surf. Sci. **39**, 235 (1997).

[136] P. J. Chen, M. L. Colaiannni, and Y. T. Y. Jr., *Inhibition of atomic hydrogen etching of Si(111) by boron doping*, J. Appl. Phys. **70**(6), 2954 (1991).

[137] H. Kim, G. Glass, T. Spila, N. Taylor, S. Y. Park, J. R. Abelson, and J. E. Greene, *Si(001):B gas-source molecular-beam epitaxy: Boron surface segregation and its effect on film growth kinetics*, J. Appl. Phys. **82**(5), 2288 (1997).

[138] Y. Ma, C. T. Chen, G. Meigs, F. Sette, G. Illing, and H. Shigakawa, *Potassium-induced charge redistribution on Si(111) surfaces studied by core-level photoemission spectroscopy*, Phys. Rev. B **45**(11), 5961 (1992).

[139] B. Gong, D. E. Brown, J. H. Kang, S. K. Jo, Y. M. Sun, and J. G. Ekerdt, *Boron-induced stabilization of the Si(100)-(2×1) surface reconstruction*, Phys. Rev. B **59**(23), 15225 (1999).

[140] B. E. Weir *et al.*, Appl. Surf. Sci. **84**, 413 (1995).

[141] R. L. Headrick, B. E. Weir, A. F. J. Levi, D. J. Eaglesham, and L. C. Feldman, *Si(100)-(2×1)boron reconstruction: Self-limiting monolayer doping*, Appl. Phys. Lett. **57**(26), 2779 (1990).

[142] Y. Wang, J. Shan, and R. J. Hamers, *Combined scanning tunneling microscopy and infrared spectroscopy study of the interaction of diborane with Si(001)*, J. Vac. Sci. Technol. B **14**(2), 1038 (1996).

[143] Y. Wang and R. J. Hamers, *Boron-induced morphology changes in silicon chemical vapor deposition: A scanning tunneling microscopy study*, Appl. Phys. Lett. **66**(16), 2057 (1995).

[144] H. Kim, G. Glass, S. Y. Park, T. Spila, T. Taylor, J. R. Abelson, and J. E. Greene, *Effects of B doping on hydrogen desorption from Si(100) during gas-source molecular-beam epitaxy from* Si_2H_6 *and* B_2H_6, Appl. Phys. Lett. **69**(25), 3869 (1996).

[145] G. B. Bachelet, D. R. Hamann, and M. Schlüter, Phys. Rev. B **26**, 4199 (1982).

[146] N. Troullier and J. L. Martins, *Efficient pseudopotentials for plane-wave calculations*, Phys. Rev. B **43**(3), 1993 (1991).

[147] D. E. Aspnes and N. Dietz, *Optical approaches for controlling epitaxial growth*, Appl. Surf. Sci. **130-132**, 367 (1998).